Università degli Studi dell'Insubria
Dipartimento di Scienze e Alta Tecnologia
Corso di Dottorato in Astronomia e Astrofisica

Gamma-Ray Pulsars: a Multi-Band View

PhD Candidate:
Maura Pilia

Supervisors:
Prof. Aldo Treves
Dr. Alberto Pellizzoni

XXIV Ciclo di Dottorato

Preface and Summary

This Thesis is based mainly on the results of the timing analysis applied to the gamma-ray pulsars observed principally by the AGILE *satellite and also extended, in some cases, to observations with the* Fermi-*LAT satellite and the* MAGIC *Cherenkov telescope. Aim of this extended study of pulsars at the high energies was to characterize their properties based, now, on a more statistically relevant sample, and be able to disentangle useful informations that can be key to explain the emission mechanisms in pulsars.*

THE SCIENTIFIC CONTEXT *Pulsars are highly-magnetized, rapidly-rotating neutron stars. As explained in Chapter 1, they have been observed in the radio band over the past forty years, due to their highly anisotropic emission, which, when combined with the misalignment between the rotation and the magnetic axis, produces the pulsed emission we observed, also called the "lighthouse effect". Pulsars have been observed as gamma-ray emitters as well, but it is only in the past three years that their number hit the double digits and they started to yield their potential as keys to explain the neutron stars mechanisms.*

In Chapter 1, the basics of pulsar theory are given. While the phenomenological aspects have been widely studied thanks to extensive radio observations through the years, their electrodynamics represents an articulated field that is difficult to probe. The "classical" models of magnetosphere predict the presence of regions of particles' under-density (a "gap"), inside an overall force-free magnetized area that surrounds the pulsar, where the particles can be accelerated and can produce the observed radiation, after a number of cascade processes. More "modern" models of magnetosphere, with their roots in old predictions, discuss the hypothesis of a totally force-free magnetosphere. The discussed theories search for a confirmation in our gamma-ray observations, as the gamma-rays are the ones carrying away a good fraction of the rotational energy loss.

THE NEW PERSPECTIVES OPENED BY THE MULTI-BAND OBSERVATIONS *In April 2007 the Italian Space Agency launched the* AGILE *satellite for gamma-ray astronomy. About one year later,* AGILE *was joined in the observation of gamma-rays by the 16 times bigger* Fermi-*LAT satellite launched by NASA.* AGILE *and* Fermi-*LAT, with their wide field of view and large collective area, are particularly suited for the study of pulsars at high energies. Most recently, the window of very-high energy observations has opened up to pulsar studies and, in particular, by the* MAGIC *telescope, with the lowest up to now threshold for ground-based telescopes, at 25 GeV. Its observations are briefly described, together with* AGILE *and* Fermi-*LAT's, in* C*hapter 2.*

The techniques for studying pulsars in the gamma-rays are also explained in C*hapter 2, with the fundamental premise about the radio observations which were part of my analysis work, as they constitute the primary basis for the gamma-ray observations. The advances with respect to the observations of the previous generation gamma-ray instruments are highlighted. In particular,* AGILE *was able to take into account, for the first time in gamma-ray observations, the timing noise that affects young pulsars. In this way, the observations can be carried out for longer time spans without being affected by sensible light curve smearing. Thus, we could take advantage of the long time span, up to now the longest for gamma-ray observations, to increase the resolution of our light curves and see structures at the sub-millisecond level.*

GAMMA-RAY PULSARS AGILE *and* Fermi-*LAT pulsar observations first concentrated on the known gamma-ray pulsars. As shown in* C*hapter 3, the apparently "familiar" pulsars actually hid thriving new prospects for pulsar studies, as well as the new pulsars subsequently detected, described in* C*hapter 4.*

In these two Chapters, the properties of the gamma-ray emission ars analyzed for a number of pulsars, mainly using AGILE *data, but also with* Fermi-*LAT and* MAGIC *observations. The light curves are investigated with increased resolution from previous observations and the spectral properties are addressed. The availability of a statistically significant sample of gamma-ray pulsars led us to draw some lines on the models. The classical polar cap model seems to be failing the test of gamma-ray observations for most of the present sample, and a simple explanation of which can be found in conservation laws arguments discussed in*

Chapter 4. *At the same time it starts getting clear that a model that contemplates a single gap zone does not seem to be feasible to explain the observed pulse profiles. And, possibly, the entire gap theory should be combined with the more physical force-free models.*

Episodes of variability in pulsars have been observed and studied in this context. The Vela glitch of August 2007 was observed by AGILE *in search for gamma-ray emission. The Crab pulsar could have a contribution to the emission from a newly observed third pulsar peak, that is less significant and much weaker than the canonical two, and could be due to giant pulses.* AGILE *observed the first gamma-ray millisecond pulsar but its emission only appeared in a restricted time interval, leading to the interesting possibility that pulsar emission might have some intrinsic variability.*

HIGH MAGNETIC FIELD PULSARS *After the advent of* Fermi-*LAT,* AGILE *found its collocation in the gamma-ray astronomy in the characterization of the low-energy gamma-rays (from 30 to 100 MeV), where the collective areas of the two instruments is equivalent, but* AGILE *deals with much lower background. For this reason, we concentrated on those pulsars that show a low-energy cutoff, which were theorized to emit gamma-ray radiation through the exotic QED process of photon splitting.*

A detailed analysis of the two most significant cases is given in Chapter 5. *We have found that the concurrence of a high magnetic field and an aligned geometry, could overcome the objections from* Chapter 4 *against inner magnetosphere emission and be, indeed, dominated by polar cap emission. Interestingly, this phenomenology, that is observed in pulsars that are similar to magnetars, may be observed in objects that are transitioning from pulsar to magnetar.*

THE ENVIRONMENT OF PULSARS *Young pulsars are known to power a relativistic wind of particles that surrounds the pulsar and is best known as its Pulsar Wind Nebula (PWN). Important phenomena take place in the PWN and they are powered by the pulsar inside it. As discussed in Chapter 6, very high energy emission was already observed from PWN, but high energy emission was missing, in a spectral region where important constraints on the emission processes could be given.*

AGILE *was the first satellite to detect GeV emission from a PWN apart from Crab, Vela X, and it was also the first to claim the unexpected flux variation in the*

Crab Nebula which underwent two intense flares in 2010 and 2011. In Chapter 6 *we give a description of the events and a possible trail for an interpretation, although no clear picture can yet emerge from the observed events.*

CONCLUSIONS AND FUTURE PROSPECTS *The multi-band approach that has been used for the observations described in this Thesis has proven valid for the exploitation of new science and the most useful approach for the comprehensive analysis of pulsar phenomena across the electromagnetic spectrum. As a completion to this work, the more comprehensive* AGILE *Pulsar Catalog is in preparation. It will comprise all the pulsars observed by* AGILE *and particularly focus on the low-energy tail of them, which present interesting properties that bridge pulsars and magnetars.*

Contents

Chapter 1

An Introduction to Pulsars

Pulsars and their environments are the topic of this Thesis. Here a brief introduction on pulsars, their origin, their evolution and the attempts at modeling their emission, is given.

1.1 Pulsars

Pulsars, discovered in 1967 by Anthony Hewish and his student Jocelyn Bell [101], are neutron stars which spin very rapidly around their axes ($0.0012 < P_{rot} < 12$ sec) and have a high surface magnetic field ($10^8 < B_s < 10^{15}$ G). The misalignment between the rotation axis and the magnetic one is at the origin of the observed pulsation.

A neutron star is the residual nucleus of the explosion of a massive star of at least $8-10$ $M_\odot$. Neutron stars have typical radii of the order of 10 km and masses around 1.4 $M_\odot$. Their internal structure is still mostly unknown. With densities which reach 10^{14} g cm^{-3}, after the collapse, it is believed that the exterior is constituted by heavy elements' nuclei, among which iron, while the interior is predominantly made of neutrons which become superfluid in the interior. Depending on star mass and rotational frequency, the matter in the core regions of neutron stars may be compressed to densities that are up to an order of magnitude greater than the density of ordinary atomic nuclei. This extreme compression provides a high-pressure environment in which numerous subatomic particle processes are likely to compete with each other. The neutron star equation of state depends on the composition of the matter inside the star and it governs global properties such as radius for a given mass. So far open, with a wide range of cases, the issues of the interior of neutron stars and of their equation of state have pulsars as their best probes.

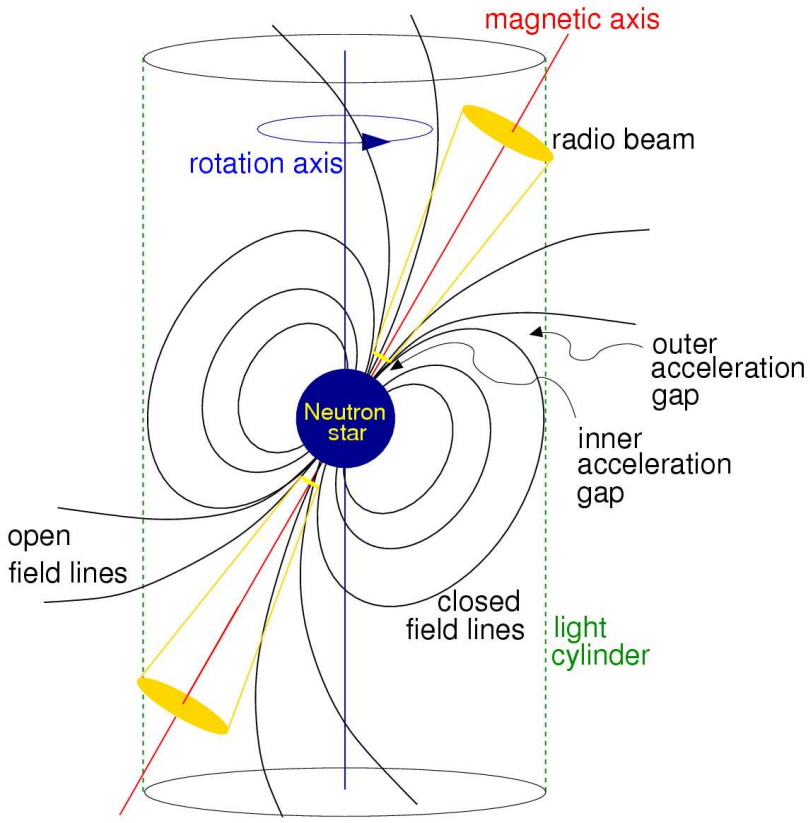

Figure 1.1 Representation of a pulsar and its closest environment, see text for details.

1.1.1 Why Study Pulsars?

Pulsars are very interesting study objects on different levels. They are the most extreme laboratories for the study of the physics of the matter at its highest densities and in a regime of very high magnetic fields, that are not reproducible on Earth.

The property that makes pulsars unique and mostly interesting is the stability of their rotation, especially when they are old and have been ”revived” by the transfer of angular momentum by a low mass companion star in the process of dying (see Section 1.1.4). In such cases, known as millisecond pulsars, the pulsars reach periods of the order of one millisecond and their rotation is so stable that, in time, they represent the stablest clocks even compared to the best atomic standards. These pulsars have been used to perform the most precise tests of the theory relativity by Albert Einstein, and are believed to be possible sources of gravitational waves as well as ”detectors” that can be timed to find them, due to the extreme stability of their rotation. The discovery of the gravitational waves would not only prove Einstein right once again, but they would open new and completely unexplored territories for the astrophysical studies.

I am member of the European Collaboration for the use of pulsars as a timing array (EPTA) which dedicates its efforts and conjunct radio telescope time to the detection of gravitational waves in the residuals of the pulsars observations (see Section 2.2.2). This topic is very interesting but is lies outside the work presented in this Thesis.

1.1.2 Birth of a Pulsar

When the core of a massive star collapses, the star radius is shrunk from 10^6 km to around 10 km. This shrinking results in the increase of the rotational velocity of the pulsar, for the conservation of the angular momentum: $I_i\Omega_i = I_f\Omega_f$, where $I = mr^2$ is the angular momentum and Ω the angular velocity, while i and f represent the initial and final stage of the formation of the neutron star. At the same time internal processes, whose nature is still unclear, make the surface magnetic field become extremely high. Thus a newly born pulsar typically has rotational periods $P = \Omega^{-1} \sim 10$ ms and magnetic fields $B \sim 10^{11-12}$ G. Pulsars' electrodynamics in these conditions is quite complicated. A more detailed explanation will be presented in Section 1.2; here the approximate theory of radiation from a magnetic dipole is presented.

The high surface magnetic field of the pulsar creates a high electric field which

in turn, given the high conductivity of the matter on the surface, brings to a charge separation, as for Gauss' law:

$$\sigma = \frac{1}{4\pi}(\vec{\nabla}\cdot\vec{E}) = -\frac{1}{2\pi c}\vec{\Omega}\cdot\vec{B}, \tag{1.1}$$

where σ is the internal charge surface density, $\vec{\Omega}$ is the angular rotation velocity of the neutron star, $\vec{E}$ and $\vec{B}$ are the electric and magnetic fields on the surface of the star. In an aligned rotator model (which is not the general case, but a valid approximation) the magnetic and rotation axes are aligned so that, for equation 1.1, the positive charges will flow towards the magnetic equator and the negative charges towards the poles. The high field strengthen the segregations and it is capable to extract the charges from the poles and have them co-rotate around the star, hooked to the magnetic field lines because of the extremely high conductivity of the stellar matter and the plasma. Co-rotating with the charged particles, the field lines are only closed until the co-rotation velocity is smaller than the speed of light in vacuum (c). This establishes a characteristic radius, the *light cylinder radius*, which can be derived as $R_{LC} = c/\Omega$. Inside the light cylinder the field lines are closed and they create a region of charged plasma around the neutron star, known as its *magnetosphere*. Outside the light cylinder the field lines open and the particles emit radiation in a collimated beam towards infinity.

The electrons, which are initially very energetic, move along and spiral around the field lines and emit curvature and synchrotron radiation. Cascade processes, which have not yet been fully understood (see Section 1.3.1) are responsible for the energy loss in the radiation which leads to the coherent radio emission that is observed, through subsequent steps of pair production and annihilation.

1.1.3 The $P\dot{P}$ - Diagram and the Pulsars' Evolution

Before the discovery of pulsars, [64] and then [166] proposed an emission mechanism related to the energy loss from magnetic dipole emission, following

$$\frac{dE}{dt} = \frac{d}{dt}(\frac{1}{2}I\Omega^2) = -\frac{2\Omega^4\mathscr{M}^2\sin\alpha^2}{3c^3} \tag{1.2}$$

where $\mathscr{M} = \frac{1}{2}R^3B$ is the magnetic dipole moment and B is the magnetic field at the pole, for a uniformly magnetized sphere. If we explicit $\mathscr{M}$ and $\Omega = 2\pi/P$, we get

$$P\dot{P} = \frac{8\pi^2}{3c^3}\frac{B^2R^6\sin^2\alpha}{I}. \tag{1.3}$$

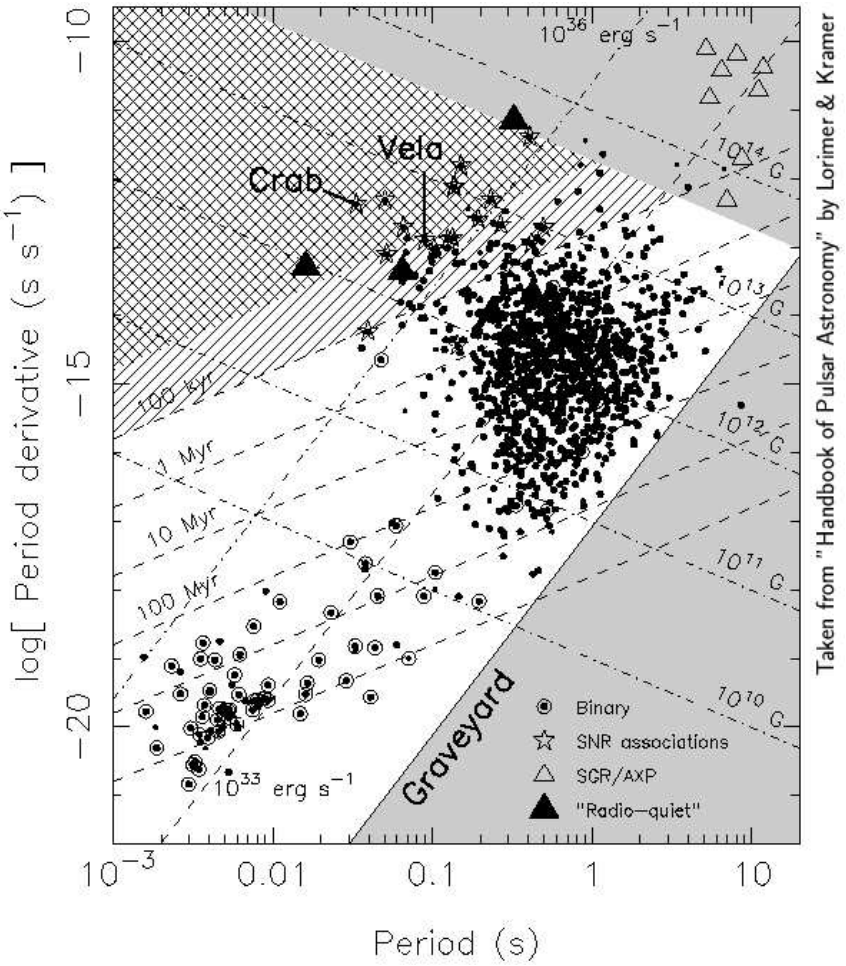

Figure 1.2 Evolutive diagram for pulsars, as a function of their rotational period and period derivative. See text for details.

Thus the pulsar loses energy through magnetic dipole emission and, in time, it spins down. For the young pulsars, the period derivative is of the order $\dot{P} \sim 10^{-13}$ ss^{-1}. No decay of the magnetic field strength is observed during a pulsar lifetime (around 10^8 yr, [93]).

The pulsar slow-down can be expressed in terms of the angular velocity as $\dot{\Omega} = \Omega^n$, where n is the *braking index* and can be expressed as

$$n = \frac{\Omega\ddot{\Omega}}{\dot{\Omega}^2}; \tag{1.4}$$

n should equal 3 for a perfect dipole. The fact that the observed values range from 1.4 to 2.9 (with a very recent measurement down to $n = 0.9$ [72]), reflects the fact that the pulsar is not placed in vacuo, that it is influenced by currents and winds, and that the multipole components can play a relevant role. If we assume the dipole approximation to still be valid to some extent, and consider the initial spin period of a pulsar to be very small with respect to the actual period, an estimate of the spin-down age can be obtained as

$$\tau = \frac{1}{(n-1)}\frac{\Omega}{\dot{\Omega}} = \frac{1}{(n-1)}\frac{P}{\dot{P}} \tag{1.5}$$

which is valid for $n \neq 1$ and in particular, in the magnetic dipole approximation, it becomes

$$\tau = \frac{1}{2}\frac{P}{\dot{P}}. \tag{1.6}$$

τ is the so-called spin-down age, usually an upper limit to the real age of the pulsar. From the spin-down law, a relationship can be drawn that links the magnetic field at the surface of the pulsar to its period and period derivative:

$$B_{NS} = \left(\frac{3c^3}{8\pi^2} P\dot{P} I_{NS}\right)^{1/2} \frac{1}{R_{NS}^3 \sin\alpha} \tag{1.7}$$

which becomes

$$B \approx 3.2 \cdot 10^{19} \sqrt{P\dot{P}}\ \mathrm{G} \tag{1.8}$$

assuming typical parameter values for the neutron stars: $I = 10^{45}$ g cm^2, $R = 10$ km and $\sin\alpha = 1$.

One can, therefore, represent the evolution of a pulsar through a $P - B$ diagram (or the equivalent $P - \dot{P}$). Figure 1.2 shows the diagram, where the iso-age lines for pulsars are underlined. The young pulsars are located in the top left corner of the diagram. Most of the observed pulsars are slower, but with magnetic fields similar to those of the younger pulsars. We can highlight a region where no pulsars are

observed: this is the so-called *death valley*: there comes a time (around $10^7 - 10^8$ yr, depending on the rotation period) when pulsars reach too low luminosities, below the detection limits for present instruments: the emission mechanism is no longer able to keep the pulsed radio emission active. It is assumed that a critical period exists which determines the end of the pair production for the coherent radiation. The fact that such a death line exists is due to the fact that the emission is coherent and that it is originated by cascade processes [45].

1.1.4 Characteristics of Young and Old Pulsars

The young pulsars occupy the top left hand side of the $P - \dot{P}$ diagram because, when they are born (see Section 1.1.2) they are characterized by very high rotation frequency and surface magnetic field. In time both decrease because of the energy losses (see Section 1.1.3). The sample of young pulsars is limited due to their short lives ($\sim 10^4 - 10^5$ yr). Young pulsars are characterized by the presence of *star quakes*: aftershock settlements which indicate that the neutron star is progressively relaxing in its inside. *Glitches* are observationally associated to these phenomena: sudden variations of the pulsars' rotation period which are superimposed to the secular spin-down. They are believed to be originated (see e.g. [191, 73] and references therein) by a sudden change in the deformation of the stellar crust with respect to a sphere. This change causes a variation of the moment of inertia which, in turn, causes a variation of the spin frequency so that the angular momentum is conserved. Observing a glitch, and its subsequent relaxation, makes it possible to study the interior of a neutron star and the solid state physics in extreme conditions. The observations point to a scenario where the external crust is solid while the internal one is fluid.

A small (but increasing) number of pulsars occupies the bottom left region of the diagram. These pulsars have periods of the order of milliseconds, magnetic fields of the order 10^8 G and a high characteristic age, close to the Hubble time ($\tau_h \sim 10^{10}$ yr). These properties imply that these *millisecond pulsars* (MSPs) must have ended their lives but have then be "reaccelerated" so as to move through the death line towards the left and be observable again. The scenario that is nowadays accepted to explain this phenomenon is called *recycling* (see e.g. [204]). Binary systems where the companion star has a low mass go through a complete recycling and are reaccelerated to very short periods ~ 1 ms. Systems with an intermediate mass produce mildly recycled pulsars ($\sim$ tens of ms). Systems with a massive

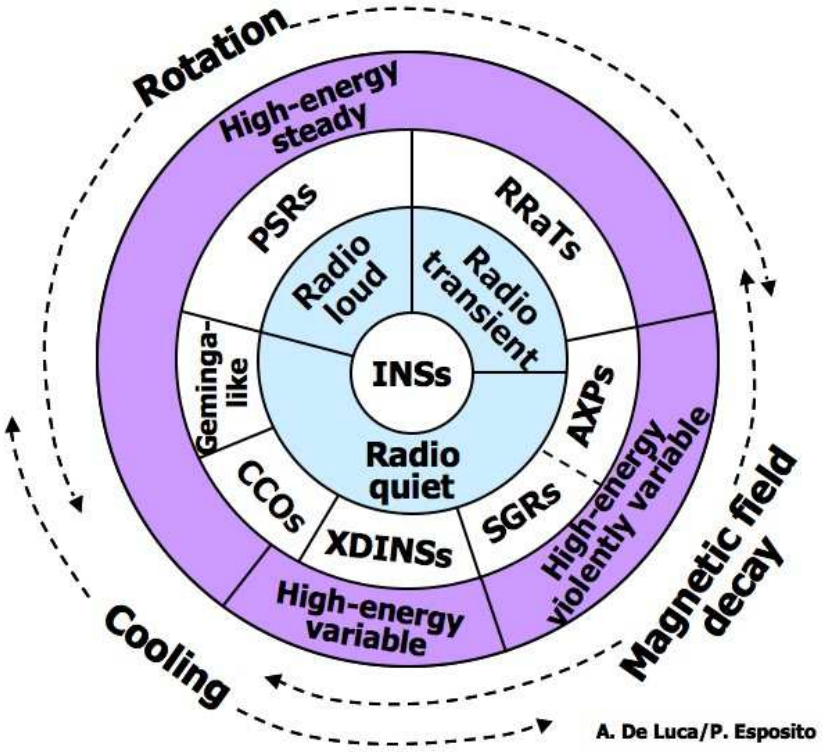

Figure 1.3 A scheme of the variety and properties of the isolated neutron stars. The overall classical distinction among the different classes is mainly based on the mechanism that powers their emission: the rotational energy loss, the magnetic field decay or the cooling. The rotation powered neutron stars are typically non variable, while the magnetic powered are typically highly variable, but a superposition can be observed. In the center, the radio behavior is highlighted, which does not show a definite correlation with the powering mechanism. Credits P. Esposito

companion go through a more catastrophic evolution. The accretion is not stable and it can be carried out by the wind of the main sequence star, if it is particularly massive. The two stars can get attracted towards one another due to the strong gravitational field; they are enclosed by a common envelope which can, in some cases, collapse to give a single remaining compact object. The evolution is fast and irregular and it terminates with a second supernova explosion. This is why it is so rare to observe binary systems composed by two neutron stars or even two pulsars.

1.1.5 Beyond Pulsars: the Ever Increasing Zoo of Non-Pulsar NSs

The last decade has shown that the observational properties of neutron stars can be remarkably diverse. The challenge is to establish an underlying physical theory of neutron stars and their birth properties that can explain the great variety. Here

a schematic presentation is given of the currently identified zoo of neutron stars. We have up to now described pulsars traditionally identified as *"radio pulsars"* but recently dubbed *"rotation powered pulsars"* to have a most observationally accurate and precise definition: these objects are powered by their loss of rotational energy due to braking by their magnetic field. *"Millisecond pulsars"*, though also rotation powered, have different evolutionary histories, involving long lived binary systems and a recycling episode which spun-up the neutron star and quenched its magnetic field. One of the latest additions to the zoo, the *"rotating radio transients"* (or RRATs), do not seem to produce observable periodic emission, the defining property of the rotation powered pulsars, but unpredictable short bursts which occur at integral multiples of an underlying periodicity.

The radio emission has initially been one of the fundamental characteristics of the neutron stars. With the advent of new X-ray satellites, different subclasses of generally radio-quiet neutron stars have emerged. The *"isolated neutron stars"* present, as defining properties, quasi-thermal X-ray emission with relatively low X-ray luminosity, great proximity, lack of a radio counterpart, relatively long periodicities ($P = 3 - 11$ s). *"Magnetars"* have occasional huge outbursts of X-rays and soft gamma-rays, and luminosities in quiescence that are orders of magnitude greater than their spin-down luminosities. They are thought to be young, isolated neutron stars powered by the decay of a large magnetic field. Finally, a handful of *"central compact objects"* constitute an X-ray bright, likely heterogeneous, class: their properties are not well defined yet; their name derives from their central location in supernova remnants (SNRs). Figure 1.3 gives a schematic view of the different types of isolated neutron stars, with a synthesis of the properties that unite them and those that are responsible for the differences. The challenge of the past decade has been to find a way to unify this variety into a coherent physical picture.

1.2 Pulsars' Electrodynamics

Electrodynamics plays a fundamental role in pulsars and, in general, in those sources which present an accretion disc and a linear and moderately collimated jet of matter. The electrodynamics produces relativistic particles and is thus able to explain the gamma-ray and charged-particles emission that is observed from compact objects.

1.2.1 The Oblique Rotator Mechanism

As stated in section 1.1.3, pulsars can lose energy due to the presence of a magnetic dipole $\vec{\mathscr{M}}$, that is inclined with respect to the rotation axis with an angle α. To an external observer this appears as a magnetic field varying in time and it implies an energy loss due to the emission of electromagnetic radiation, following the equation (Landau & Lifschitz, 1985)

$$\dot{E} = -\frac{2}{3c^2}(\ddot{\mathscr{M}})^2, \tag{1.9}$$

which, as seen in section 1.1.3, can be translated into equation 1.2. The source of the missing energy is the rotational energy of the pulsar, $E = I\Omega^2/2$, so that, as already seen,

$$\dot{E} = I\Omega\dot{\Omega}, \tag{1.10}$$

which implies a decrease of the rotational period of the pulsar with time.

The electromagnetic radiation ought to also be responsible for the angular momentum loss, since $I\dot{\Omega} < 0$ (see section 1.1.2) and we assume the star to be located in vacuum. This very mechanism leads, in fact, to the conclusion that the environment surrounding the pulsar is not empty, but it is the household of important physical phenomena. If the pulsar rotates with angular velocity Ω, one would expect that its entire luminosity should be irradiated at frequency $\nu = \frac{\Omega}{2\pi}$,while we mainly observe radio emission from pulsars, i.e. at frequencies of hundreds of MHz or GHz. This means that electrons surround the pulsar, and they convert the energy, which reaches us, as electromagnetic radiation of high amplitude and small period, into kinetic energy that they themselves irradiate.

1.2.2 The Magnetosphere

A comprehensive model that can satisfactorily explain the complex phenomena that take place in the magnetosphere of a pulsar is still to be developed. A basic model can be proposed even from a strictly maxwellian point of view. The reason why we speak about *electrodynamics* for compact objects lies in the fact that the electromagnetic forces that are present on the matter outside the object are much higher than any other force.

Let us initially suppose that the magnetic field is purely dipolar and that the rotator is aligned (see section 1.1.2). The particles can freely flow along the field lines, while the motion in the direction perpendicular to the field is highly hampered. The field lines can be considered as bare wires, as the particles are

strongly connected to their field line and will follow it closely. This is only true as long as the Larmor radius of the particle ($r_L = mvc/eB$) is much smaller than the distance from the compact object, while at great distances from the pulsar the particles can migrate from one line to the other.

To prove that the medium around the pulsar is not empty, one can hypothesize that it is and calculate the electric force acting on the surface charges. Since the internal matter of a pulsar has high conductivity, the electrons inside it are disposed in a way that the force acting on them, i.e. the Lorenz force, is null at equilibrium:

$$\vec{E} + \frac{\vec{v}}{c} \wedge \vec{B} = 0 \tag{1.11}$$

where $\vec{v} = \vec{\Omega} \wedge \vec{r}$ is the rotational velocity of the star. The equation shows that there must be an electric field inside the pulsar and thus there has to be one outside as well, because of the presence of surface charges on the pulsar. If we compare the electric and gravitational forces,

$$\frac{eE_{\|}}{GMm/R_p^2} \simeq 8 \cdot 10^{11} \tag{1.12}$$

where $E_{\|}$ is the electric field component that is parallel to the magnetic field and R_p is the neutron star radius at the pole, it is apparent that the gravitational force is negligible with respect to the electrostatic one, for each electron. If a pulsar were placed in vacuum, its surface fields would be so strong as to pull out the surface charges and fill the vacuum.

As long as a non zero force is applied to the electric charges, they will be extracted from (or created at) the surface of the pulsar. The stationary condition is thus that the total force on the electric charges be null. In this case the total force is the Lorenz force, having assumed that the gravitational force is negligible and therefore considering the particles as massless:

$$\rho\vec{E} + \frac{\vec{j}}{c} \wedge \vec{B} = 0 \tag{1.13}$$

where ρ is the charge density and $\vec{j}$ is the current density. From this equation, it was deduced the fundamental force-free condition (ref):

$$\vec{E} \cdot \vec{B} = 0, \tag{1.14}$$

viz. null electric field in the direction of the magnetic field. Charges are produced outside a pulsar in massive quantities, so as to cancel the sum of the magnetic force

and electric, repulsive force, generated by the charges themselves. Moreover, the charges are not static and they can generate other electric and magnetic fields that should be taken into account when calculating the motion of the charges.

A simple argument leads to believe that the magnetospheric regime should be of charge separation. If the gravitational forces are believed to be negligible with respect to the electrostatic forces, a small electric field can be thought to compensate for them. However, if this is true for the electric charges of one sign, then the opposite should be true for the charges of opposite sign, whose field would add up to the gravitational forces. In this framework, there would be nothing to prevent the charges from falling onto the pulsar, except for pressure, requiring thermal velocities of the order $v_{th}^2 \approx GM/R$, which, for the typical radius of a neutron star ($R \sim 10$ km), implies a temperature $T \sim 10^9$ K. Such a high temperature is hard to keep in the presence of high magnetic fields and would cause relevant radiative losses.

1.2.3 The Goldreich-Julian Model

The model elaborated by Goldreich & Julian (1969) is the first attempt at explaining the magnetosphere of a pulsar. It assumes charge separation. The light cylinder (see section 1.1.2) separates an interior region where the charges rigidly co-rotate with the star and magnetic lines are equipotential, from an exterior region where the charges cannot co-rotate and the field lines cannot be equipotential. The lines inside the light cylinder are closed and originate the *co-rotating magnetosphere*; the others, which cross the light cylinder, do not close and acquire a toroidal component (along $\hat{e}_\phi$), which becomes dominant at large radii and produce a magnetic field that decays as $B_\phi \propto \frac{1}{r}$ for $r \to \infty$, because of the infinite current.

In order to avoid the net loss of charge, the model assumes the presence of a *critical line* (see figure 1.4), which leaves the pulsar's surface with an angle θ_c and whose potential equals the one at infinity. The particles at $\theta < \theta_c$ (small latitudes) will thus have negative potential with respect to the critical line, and vice versa for those at $\theta > \theta_c$. Along the field lines close to the pole the negative charges will flow to infinity, while the positive charges will flow from the lines close to the closed one.

The Goldreich-Julian model, albeit still approximate and not devoid of faults, presents a fundamental result: the pulsar loses energy even in the case of perfect alignment while in the Pacini model it requires the misalignment between the magnetic and rotation axes ($\dot{E} \propto \sin^2\alpha$). The only possible source of energy

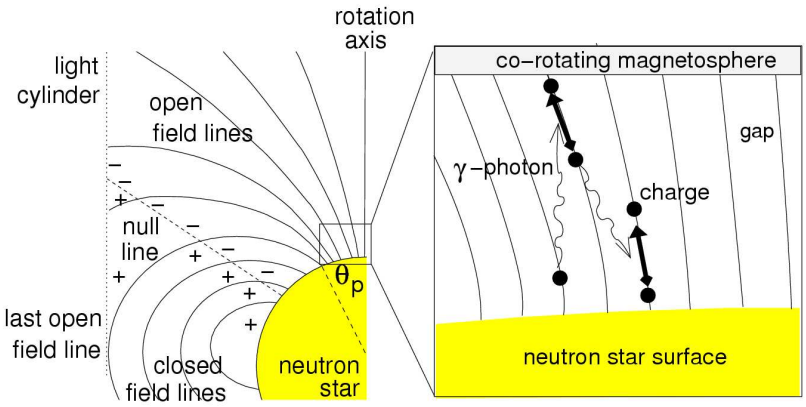

Figure 1.4 Representation of a pulsar magnetosphere, see text for details.

must be the rotational energy. And since the rotational energy is related to the angular momentum loss, the same mechanism must also be able to dissipate angular momentum.

1.3 Particle Acceleration: Modern Models of Magnetosphere

The Goldreich-Julian model, in its assumption of charge separation, predicts a minimum density of the plasma co-rotating with the pulsar. Different radiation mechanisms (see below) require a magnetospheric plasma density that largely departs from the Goldreich-Julian density

$$\rho_e = -\frac{\Omega \cdot B}{2\pi c(1-\Omega^2 r_\perp^2/c^2)}. \tag{1.15}$$

A number of models predict the formation of these plasma excesses in virtue of the presence of *gaps* in the magnetosphere. In these regions the condition of co-rotating magnetosphere is no more valid and the total force is not null, so that a residual electric field is present: $E_\parallel$. The regions where the gaps are expected are the ones where there is plasma depletion. Two such regions have historically been located: the one of open lines above the magnetic pole (*polar cap* models) or the one between the critical line and the last open or closed field line (*outer gap* models).

1.3.1 Low-altitude Models

The polar cap models [193] invoke the the presence of a gap in the polar region to explain the energy emission from a pulsar. Thence a pair cascade originates:

the charged particles are extracted from the star's surface and accelerated from the residual magnetic field up to relativistic energies (the particles reach Lorenz factors $\gamma \lesssim 10^7$). Moving along the magnetic field lines the particles produce gamma-ray photons, by curvature radiation or inverse Compton with low-energy photons. In a high magnetic field the photons can split and generate electron-positron pairs (provided the energy of the photon exceeds the rest energy of electron plus positron: $E \geq 2m_e c^2 = 1.02$ MeV). Yet again these particles, which are still highly energetic, can produce a second photon cascade and then pairs; even a third cascade can originate. The initial plasma density increases of a factor 10 up to 10^4. It is this secondary plasma (or the tertiary) that produces the radio pulsed emission. The lessening or end of these processes is what causes the pulsar to pass the *death line* (see section 1.1.3). The first generations of particles which are accelerated by the open magnetosphere should be responsible for the high energy emission.

1.3.2 Rim Models

The polar cap model already encountered its initial problems when the first sample of gamma-ray pulsars was observed in the Nineties. The model could not easily explain how the sources could show both remarkable similarities and puzzling variations in their light curves and phase-resolved energy spectra. Inconsistencies further arose when comparing gamma-ray light curves to those from other wavelengths. It was proposed that the continuous pair-creation above the top of the acceleration zone would create a dense, approximately force-free, column of pair plasma streaming away from the star. Different versions of these adaptations have been proposed in time: space charge limited flow [23], pair starved [55], two-pole caustic [69] and they seem to have overcome the classical polar cap models problems.

These the classical polar cap model premises: the gamma-ray emission is initiated by the acceleration of electrons from the surface of the star above the pole and towards infinity via the open field lines; the emission is originated by curvature radiation of the electrons along the open field lines; the pair conversion by the magnetic field and the synchrotron radiation by the pairs produce photon-pair cascades from which the observed gamma-radiation emerges. In order to accommodate the discrepancies with the observations, to these were added the requirement of an aligned geometry and that the acceleration of the electrons should occur over an extended distance above the polar cap so that the peak energies are

reached at heights of a few neutrons star radii. Additionally the surface density should be concentrated near the polar cap rim.

1.3.3 Outer Magnetosphere Models

In these models the gaps are assumed to be in the external magnetosphere, near the critical field line which spatially separates the charges of opposite signs. In this region the particles which are removed are not replaced by new particles from the surface of the pulsar [105] and therefore a large gap is formed between opposite charged surfaces.

The actual form of this model has been developed by [47, 189]. It predicts particle acceleration, high energy emission and pair production, in a lower magnetic field than that that of the polar cap models. In general this model is used to explain the high energy emission, not the radio one which, in some cases, was not predicted by this model other than as an exception. The high energy emission is due to synchrotron or curvature radiation with higher Lorenz factors, as the magnetic fields are lower.

The recent discoveries of around 50 new gamma-ray pulsars by the *Fermi*-LAT satellite ([7], see Chapter 4), have led to an observational bias towards outer magnetospheric emission. [227] realized an ”Atlas” of pulsars light curve shapes based on the predictions of Polar Caps, Slot Gaps and Outer Gaps. If one compares *Fermi*-LAT light curves with these theoretical predictions, they would find that the emission seems to preferentially come from the outer gaps.

1.3.4 Other Models

Beside the two main streams, other models have been proposed to explain pulsar emission, of which here a brief overview is given.

Annular Gaps This model [67] predicts the existence of two kinds of acceleration regions, the core and the annular region. The critical field line divides the open field lines region of the magnetosphere into two parts: one that contains the magnetic axis (*core*), while the other one is called *annular* region and is defined by the lines that cross the null charge surface (see section 1.2.3). It is assumed that, for an oblique rotator, the particles in the magnetosphere flow out through the light cylinder and the returning currents are located in the annular region. It is also assumed that the magnetospheric plasma is not completely charge separated. If this is true, the

negative charges stripped off from the stellar surface would be naturally accelerated in the annular region.

External Models They would solve the problem that classical polar cap and outer gap models are not able to fit the polarization properties of the pulses. Two pole caustic gap models do address and solve the problems but a different site for the production of pulsed radiation has been investigated, based on the idea of striped pulsar wind. It is assumed that the magnetic energy is released by reconnection in the thin regions where the toroidal field reverses its polarity, producing a non-thermal electron/positron population. Emission from the striped wind [119, 176] originates outside the light cylinder and the phase coherence of the synchrotron radiation is guaranteed by relativistic beaming effects. The advantage of this model is that the geometry of the magnetic field, key property to determine the emission and polarization, is here relatively well known.

Force Free Magnetosphere Not all authors agree on the fact that the magnetosphere is non force-free ($\vec{J}||\vec{B}$) somewhere. Since the dawn of pulsar theory, a magnetosphere that is entirely force-free was predicted and modeled [49]. Most recently a new model has been proposed to explain the observed gamma-ray light curves in the framework of the force-free magnetosphere and it is the *separatrix layer* model by [30]. The high-energy emission originates from a thin layer on the open field lines just inside the separatrix that bounds the open flux channel. The emission from this layer generates two strong caustics which produce the typical double-peaked light curve (see section 1.5).

1.4 Radio Pulsars

Pulsars have been discovered in the radio and mostly observed in this band for over 40 years. About 2000 radio pulsars are known today and a vast amount of their science has been developed using the radio data. The typical spectrum of a radio pulsar is

$$S \propto \nu^{-\alpha} \tag{1.16}$$

with $1 < \alpha < 3$ and a high degree of polarization (up to 90%).

A pulsar profile represents its signature: every radio pulsar has a different characteristic profile. The profile can sometimes be multi-peaked, giving an indication of the inclination of the emitting beam with respect to our line of sight.

In a few cases it is possible to observe the two beams: in this case the two pulses have a phase difference of 180° between one another and the second pulse is called *interpulse*. Two models have been proposed to explain the structure of the beam: the *core and cone* model [185], where the beam is constituted by a number of emission cones that are concentrically superimposed; the *patchy beam* model [143] which predicts the presence of different emission regions randomly disposed inside the beam.

Timing (see Section 2.2) is a fundamental instrument to study pulsars because it allows the retrieval of their parameters and, therefore, to use pulsars as a base for many other studies. In particular, thanks to these measurements, it is possible to derive informations on the interior of a neutron star and determine the equation of state of the matter in extreme density conditions, to obtain very accurate astrometrical measurements and, thanks to these, map the electron population of the Galaxy; finally, the extremely precise radio pulsar measurements consent (and have already consented) to test gravitational theories in regimes of strong field and in particular the general relativity, which has already been proven right at 99.95% level by pulsar observations (see [42, 142, 124] and Section 1.1.1).

1.5 A Snapshot of Gamma-ray Pulsars before 2007

A gamma-ray pulsar is one that emits pulsed radiation in the gamma-rays (> 30 MeV).

The Earth atmosphere screens the gamma-rays and it was not until the Sixties with the first scientific missions on board balloons that the first observations were performed at these wavelengths. The first telescope for the detection of gamma-rays was launched in 1961 on board the satellite *Explorer-XI*. This telescope collected little more than one hundred photons, uniformly distributed on the galactic plane, leading to the first hint of the presence of a gamma-ray background. Nowadays the gamma-ray observations are also performed from Earth, using indirect detection techniques: the *Čherenkov* radiation produced inside the atmosphere from very high energy gamma-rays ($E \sim$ Gev $\div$ TeV) can be detected from special optical telescopes (see Section 2.3.4).

In the Seventies two very important satellites for the gamma-ray astronomy were launched: *SAS-2* from NASA, which only lasted 8 months, but highlighted the diffuse emission from the Galactic plane and detected with large statistics two point sources: the Vela and Crab pulsars; and *COS-B*, launched by ESA in

1975 and lasted till 1982, which produced the first gamma-ray sources catalog, comprising around 20 objects. A very fruitful gamma-ray mission before 2000 was the *Compton Gamma-Ray Observatory* (*CGRO*), a NASA mission launched in 1991 which lasted almost ten years. On board *CGRO* was the *Energetic Gamma-Ray Telescope* (*EGRET*), observing at energies between 20 MeV and 30 GeV. It produced an all-sky map of the diffuse emission from the gamma-rays produced in the ISM of the Milky Way by the energetic cosmic rays and it also brought relevant results in the pulsar field.

Before 2007 the ”classical” gamma-ray pulsars were Vela (B0833-45), Geminga (J0633+1746), Crab (B0531+21), B1509-58 (see Chapter 6), B1706-44, B1951+32 and B1055-52. The gamma-ray pulsars represent the brightest galactic gamma-ray sources. Typically the gamma-ray pulsars are young (see section 1.1.4) and energetic. Vela and Crab produce a very strong signal and emit in most of the bands of the electromagnetic spectrum, which makes them the most studied pulsars at present. The gamma-ray emission is usually highly pulsed, it is collimated and non thermal in origin. Not all sources are bright enough to show the pulse profile with the folding of photons through the ephemeris obtained from the radio timing (see Section 2.5.1). When observable, the pulse is double-peaked, but it may vary with growing energy, indicating that geometry plays an important role.

At the end of the *EGRET* mission, 170 sources had been detected but not identified and most of them seemed to belong to the Milky Way. Due to *EGRET*'s low angular resolution ($\sim 1^{\circ}$) with respect to a radio telescope, and the small number of photons collected for each source, for most of them no counterpart was found. Nonetheless, in some cases associations have been found with known gamma-ray pulsars or, afterwards, with subsequently discovered new radio pulsars. The main problem in the identification resides in the fact that usually more than a pulsar (or source in general) can be fitted into *EGRET* error box.

The first unidentified gamma source [75] remained unidentified for almost 20 years before the X-ray satellite *ROSAT* observed a periodicity of 237 ms showing it to be a pulsar [88]. The source was called *Geminga* as *GEMINi GAmma-ray source*, which in milanese dialect also means *there is not* because this was the first pulsar not to be visible in the radio band but only at other wavelengths. Over 30 years of observations of this source confirmed the peculiarity of this pulsar, in everything else comparable to the other rotation-powered pulsars. The reasons of the non visibility of the gamma-ray emission could be geometrical (because the radio beam

sweeps a less wide cone than the gamma-ray one) or simply of weakness of the gamma-ray emission. The question was whether Geminga was the only outlier.

Despite their very low values of period derivatives ($\dot{P} \sim 10^{-20} ss^{-1}$), the MSPs have spin-down luminosities comparable with those of the young pulsars $\dot{E} \propto \dot{P}/P^3$), due to their much smaller rotational period. Emission from these sources was, therefore, also expected.

1.5.1 The Models' Predictions

The possible processes for the non-thermal emission observed in optical, X- and gamma-rays are: synchrotron, curvature emission, inverse Compton scattering. The emission regions are the ones already identified: the polar caps or the external field lines close to the light cylinder.

In the polar cap model the emission is due to inverse Compton with infrared photons from the cascades of particles coming from the polar caps and directed towards infinity. In this model the gamma-ray emission is cut off at high energies because they are absorbed by the high magnetic field they travel across. In the outer gap model the emission is a combination of curvature and synchrotron radiation from couples which propagate downwards in the region close to the light cylinder. In this case the spectrum can extend to higher energies.

1.5.2 Supporting Observational Evidences

The information available at the *EGRET* times could not discern between the models and in particular the two main streams. Both predict most of the gamma-ray characteristics of the impulse, such as the fact that the gamma-ray beam appears in general larger than the radio one. The outer gap models predict the prominent double-peaked profiles observed at high energies and other characteristics are explained by geometrical factors. On the other hand, the models which explain the radio emission hint to the fact that pairs are created in vacuum at the polar caps and it would be straightforward to apply the same mechanism to the high-energy emission. The polar cap model predicts that the MSPs should have a high energy component up to energies of ~ 50 MeV due to curvature radiation.

A substantial difference among the predictions of the two models resides in the cutoff at high energies which is only assumed by the polar cap model. The models predict a different number of expected radio-"quiet" (Geminga-like) pulsars with respect to the radio-loud ones. The outer gap models, for example, do not predict

the radio emission and therefore expect the high energy emission to come from a different region than the radio and be completely unrelated to it. Another test of the models resides in the number of MSPs that are expected to be observable in globular clusters.

To these and other questions the detections of the new generation gamma-ray satellites *AGILE* and *Fermi*-LAT have partly answered and to this topic is devoted this Thesis. Many more questions have been raised by the new discoveries which will constitute the new challenges of pulsars studies for the next decades.

Chapter 2

Pulsar Observations

This Thesis is based on the observation of gamma-ray pulsars. As will be clearer in the second part of this chapter, the gamma-ray observations typically cannot be performed without the support of the radio observations. My preliminary work was based on the radio timing of pulsars, that is detailed in the following.

In the second part of this chapter, *AGILE* techniques for gamma-ray observation and timing of pulsars are described. These techniques are also detailed in the first pulsar work from the *AGILE* Collaboration, [173], where we solved for the first time the problem of analyzing long data-spans, perfectly accounting for the pulsar rotational parameters, without being affected by heavy light curve smearing. The techniques used for the *Fermi*-LAT observations of pulsars are fairly similar in their general outline, but are not detailed here as their development was not a part of this Thesis' work.

2.1 Radio Pulsars' Observations

It is estimated that there are about 160,000 pulsars in the Milky Way; only 2000 of them are known and, due to the width or casual inclination of the beam with respect to our line of sight, most of them will never be visible. Outside the Galaxy, pulsars have been observed only in the Magellanic Clouds and, with the present instruments, it is hard to go farther, since the flux density (usually indicated with S in the radio band) scales with the distance d as $S = \frac{L}{4\pi d^2}$. With intrinsic luminosities, at $\nu = 1.4$ GHz, $0.1 \lesssim L \lesssim 1000$ mJy kpc^2 (1milliJansky=10^{-29} W m^{-2} Hz^{-1}), typical of pulsars, and the beaming factor to take into account, there is no possibility to detect them at $d > 50$ kpc with the present instrumentation. To improve the lowest flux that can be detected, one can act on many parameters (temperature of the receiver, gain, integration time, amplitude of the frequency band), but the

present receivers already are pushed to their best performances for most of them. The situation will notably change when the Square Kilometer Array (SKA) will operate. For some of these parameters, no easy solution can be adopted because a compromise is to be found between the requirements to reach lower fluxes and the optimization of the observations. For example (see Section 2.1.2), by increasing the frequency band of the observations, the minimum flux observed can be lower, but one incurs in a higher contribution from the *dispersion* phenomenon.

2.1.1 Characteristics of the Pulsed Signal: Single, Integrated and Standard Profile

When a pulsar is observed, every single pulse coming from it represents a snapshot of the magnetosphere at the moment of the emission, but it does not convey a stable information on a pulsar. The profiles of the single pulses are in general quite different from one another while what we need is a general information. An integrated profile of a pulsar is what constitutes its signature. In order to obtain a stable information the *folding* of the pulses has to be performed (see Section 2.1.2). A pulse that is particularly stable and presents a high signal to noise ratio (SNR), is considered as the *standard profile* of a pulsar. It represents the general characteristics of that pulsar and is used as the basis of the timing model (see Section 2.2.2).

2.1.2 Dedispersion and Folding

Dedispersion The pulsed signal from a pulsar reaches us after crossing a not-empty medium, in the condition of partially ionized plasma. The signal has a *group velocity*

$$v_g = c\sqrt{1 - \frac{n_e e^2}{2\pi m_e \nu^2}} = c\sqrt{1 - \frac{\nu_p^2}{\nu^2}} \tag{2.1}$$

where c is the velocity of light in vacuum, n_e, e and m_e are the density, charge and mass of the electron, ν is the signal frequency and ν_p is the *plasma frequency*, which depends on the density of electrons in the medium and below which the signal is completely absorbed by the medium. Given this group velocity, it takes $t = \int_0^d \frac{dl}{v_g}$ to cover a distance d. This means that, if the observation is performed within a non-infinitesimal frequency band, the time profile will widen as

$$\Delta t_{DM} = \frac{e^2}{2\pi m_e c} \cdot \left(\frac{1}{\nu_{lo}^2} - \frac{1}{\nu_{hi}^2}\right) \int_0^d n_e dl \tag{2.2}$$

where ν_{lo} and ν_{hi} are the borders of the frequency interval and $\int_0^d n_e dl = DM$ is the *dispersion measure* and it represents the column density of the free electrons along the line of sight. Because of the dispersion, the high-frequency signals reach us before the low-frequency ones. For a small frequency interval $\Delta\nu$, this relation can be written in the approximate form:

$$\Delta t_{DM} \approx 8.3 \cdot 10^3 \frac{\Delta\nu}{\nu^3} DM \text{ s} \tag{2.3}$$

where frequencies are in MHz and DM in pc cm^{-3}.

As can be seen from this last equation, the widening of the time signal depends on the amplitude of the frequency band that is used. This means that the amplitude of the profile partly depends on the dispersion. The solution used to solve this problem is the *dedispersion*. Since a large band prevents the observation of the pulsed signal (which would be wider than the pulsation period), the whole band is divided into small intervals where the signal is visible. At the end, all the frequency channels are summed up, each with a different shift corresponding to its specific frequency. In this way the peaks from every channel are superimposed in phase and can be added coherently.

Folding As said (Section 2.1.1), the single pulses from pulsars are not useful for the timing because they do not give a stable information on the pulsar behavior. To obtain a general information, the operation we use is the *folding* of the pulses. The time series is folded modulo the period of the candidate signal. First, a preliminary estimate of the rotational period is obtained: a Fast Fourier Transform (FFT) is applied to the time series and we obtain a power spectrum whose peaks correspond to the periodicities found in the data. A periodic signal shows a family of harmonics in its spectrum, which can only be observed when added up, when the spectrum is weak. The secondary harmonics give a relevant contribution in the case of pulsars which have a sharply peaked profile and not a wide sinusoidal profile.

After this indication of the period is obtained with the Fourier analysis, the time series is split into a number of sub-integrations which all should include a significant number of periods. The folding of the time series modulo the pulse period is performed within each sub-integration and subsequently the sub-integrations are themselves added up, each with a different phase shift to maximize the SNR. The first estimate of the period should be as accurate as possible so as not to compromise the folding: if it is not, the error gets propagated into all sub-integrations and a drift

of the signal is observed, that is not compensated for by the phase shifts. Instead of maximizing the signal, the risk is to lose it completely. If, on the contrary, the estimate is correct, what is obtained from the folding is the integrated profile of that pulsar (see Section 2.1.1).

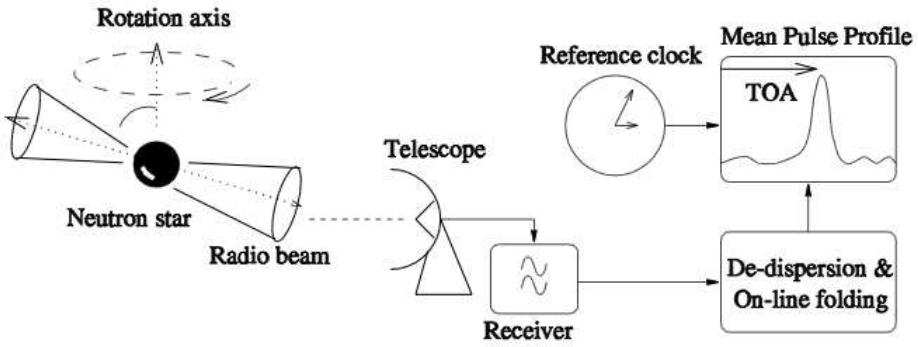

Figure 2.1 Schematic view of the timing process. The process is detailed in the text.

2.2 Timing a Pulsar

Those that have just been illustrated are the preliminary operations one has to perform with the raw data before the actual *timing*. The timing, schematically illustrated in Figure 2.1, is the fundamental instrument in the study of pulsars because it is the means to obtain very precise values of the parameters of a pulsar and heretofore is the basis for the use of pulsars as probes. The timing of a pulsar consists in the regular monitoring of the rotation of the neutron star through the study of the Time of Arrivals (ToAs) of the radio pulses. As will be seen later on (see Section 2.4), the timing at other wavelengths does not necessarily follow this procedure.

2.2.1 The Time of Arrivals of the Pulse

Usually the timing measurements take place as soon as the pulsar is discovered. Firstly, to each observation are assigned GPS spacial coordinates, relative to the receiver (or in general the observing instrument), and a temporal coordinate, from a hydrogen maser or a cesium clock present at the observatory. Once the standard profile (see Section 2.1.1) has been produced, it is convolved with the integrated profile relative to each observation and from the convolution we obtain the ToA of

the pulsed signal at the telescope, which is relative to the telescope and not inertial, as it is, i.e. *topocentric*.

Preliminary is the definition of an expression to describe the rotation of the pulsar in a co-moving reference frame; the rotational frequency of the pulsar can be written in the form of a Taylor expansion:

$$\nu = \nu_0 + \dot{\nu}_0(t-t_0) + \frac{1}{2}\ddot{\nu}_0(t-t_0)^2 + ... \tag{2.4}$$

where $\nu_0 = \nu(t_0)$ is the frequency at the reference epoch t_0 and so are its derivatives. The observed parameters, ν and $\dot{\nu}$ are related to the physical processes that determine the pulsar slow down; $\ddot{\nu}$ is generally measurable only in the youngest pulsars. Since the spin frequency corresponds to the regime of variation of the number of pulses N, this can be re-written as

$$N = N_0 + \nu_0(t-t_0) + \frac{1}{2}\dot{\nu}_0(t-t_0)^2 + \frac{1}{6}\ddot{\nu}(t-t_0)^3 + ... \tag{2.5}$$

where N_0 is the number of pulses at the reference epoch t_0. If t_0 is coincident with the arrival of a pulse, and the spin-down time is known with accuracy, then the pulses should appear as integer values of N when observed from an inertial reference frame.

The ToAs which are thus obtained are not referred to an inertial reference frame: we want them to be referred to the Solar System Barycenter (SSB). The passage is twofold: as a first thing the topocentric arrival times are referred to the center of the Earth, thus becoming *geocentric* ToAs; secondly, let us consider T to be the *barycentric* arrival time and t the geocentric one: the difference is calculated as [212]

$$T - t = \Delta R_\odot + \Delta E_\odot + \Delta S_\odot - \Delta t_{DM}. \tag{2.6}$$

To the difference contribute the corrections of, respectively, Rœmer, Einstein and Shapiro to the ToAs, plus the contribution of the DM. The Rœmer correction, $\Delta R_\odot$, is the sum of two terms: one that takes into account the time for the light to travel from the Earth to the SSB, the other which introduces a delay due to the fact that the wave fronts are spherical, even though, for the majority of pulsars, except the closest ones, the approximation of plane wave can be held valid. The Einstein and Shapiro correction are due to the effects of the general relativity within the solar system.The dispersion term relates the observed ToA to the one that would be observed at infinite frequency, otherwise every observing frequency would carry its own time delay.

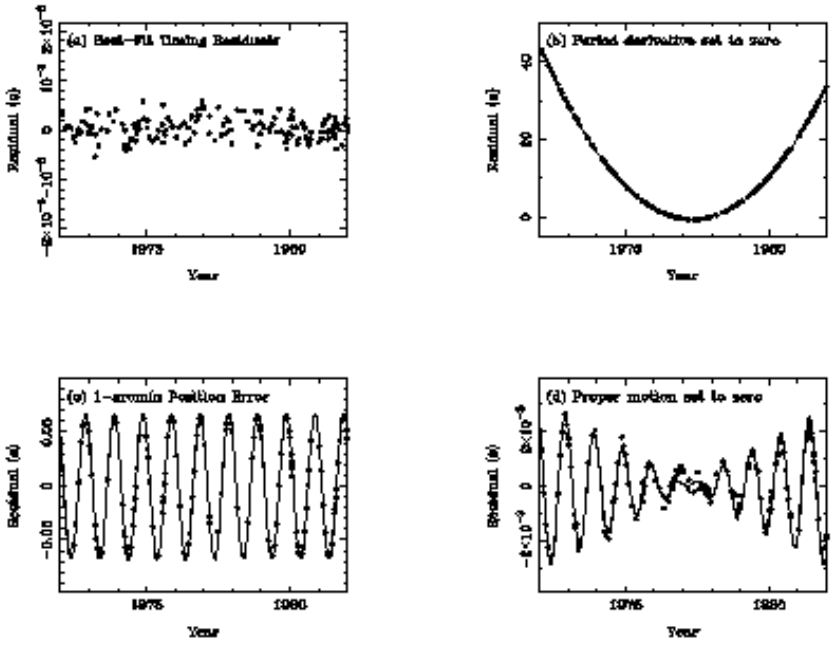

Figure 2.2 Residuals in the timing model for PSR B1133+16. (a) shows the residuals obtained with the best fit model, including period, period derivative, position and proper motion. (b) is what is obtained by fixing the period derivative to zero for this model. (c) shows the effect of a 1 arcmin error in the estimated declination. (d) shows the residuals one would obtain with the proper motion set to zero. The lines in (b), (c) e (d) show the predicted trend for the residuals relative to each effect (see text).

2.2.2 The Timing Model and the Residuals

The barycentric ToAs only depend, at this point, on the pulsar parameters: rotational, positional, of proper motion and also dispersion measure. By assigning an initial value to these parameters, we create a *timing model* which, in turn, is able to predict the barycentric ToAs of pulses at infinite frequency. The ToAs obtained by the model estimates are to be compared with observations. The differences between predicted and observed ToAs constitute the *timing residuals*. If the model is correct, then the residuals would randomly be spread around zero, meaning that the difference between the predicted and observed ToAs is null within the errors. If, on the other hand, the differences are relevant and one or more parameters have been wrongly estimated, the residuals will be characterized by systematic trends.

Usually, if the error only affects one parameter, it can be easily spotted by the trend of the residuals: it is a straight line if the error is on the estimate of the period, a parabola if the error is on $\dot{P}$, a sinusoid with yearly period if the error is on the position, and so on. Not always the trends are so easily distinguishable

from one another as in Figure 2.2: more than one parameter can be not accurate, or the observations are not enough or are too discontinuous to help separate different trends.

The timing process is iterative. At each step the residuals are minimized and eventually, when the observations have been carried on long enough, the timing allows to determine the spin parameters (P, $\dot{P}$, $\ddot{P}$, ...) and the astrometric ones (position, proper motion, parallax, dispersion measure), for the isolated pulsars. For pulsars in binary systems also the orbital parameters can be assessed. The five Keplerian parameters that can be obtained are: the orbital period P_b, the longitude of the periastron ω, the epoch of passage at periastron T_0, the eccentricity e and the projection of the semi-major axis $x = a \sin i$, where a is the semi-major axis and i the inclination angle of the orbital plane. From these parameters it is possible to determine the mass function:

$$f(m_p, m_c) = \frac{4\pi^2}{G} \frac{(a_p \sin i)^3}{P_b^2} = \frac{(m_c \sin i)^3}{(m_p + m_c)^2} \tag{2.7}$$

where m_p and m_c are the pulsar and companion masses, G is the gravitational constant and the rest are the above mentioned keplerian parameters. From the mass function, assuming a standard pulsar mass of $1.4 M_\odot$, it is possible to estimate the companion mass as a function of the inclination angle of the orbit, i, with a minimum in correspondence of $i = 90^o$. If the system is very tightly bound, and therefore relativistic, in a longer time it is also possible to retrieve the five Post-Keplerian (PK) parameters: $\dot{P}_b$, orbital period derivative; $\dot{\omega}$, periastron longitude derivative; r and s, Shapiro relativistic corrections, and γ relativistic correction due to the gravitational redshift. In the gravitational theories, the PK parameters depend on the known keplerian ones and on the two masses of the system, unknown at first. The measurement of one PK parameter puts constraints on the masses values; the measurement of two determines the masses in the framework of a specific theory. The results obtained after 3 years from its discovery, from the binary pulsar J0737-3039, consented the confirmation of Einstein's relativity theory at, at least, 99.95 % [124]. Even better results are expected from the follow-ups from recent years and these are in fact some of the more interesting prospects for future pulsar studies (see Section 1.1.1).

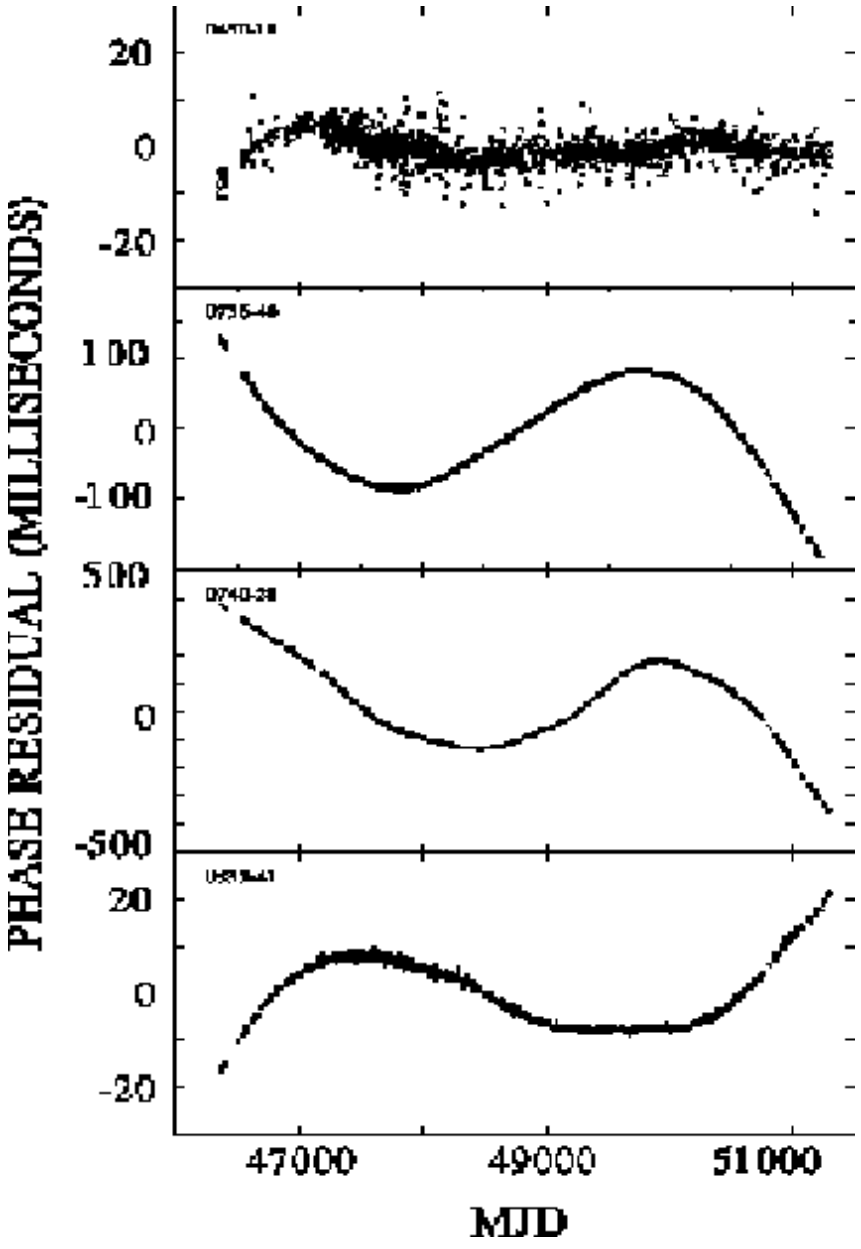

Figure 2.3 Effect of the timing noise on pulsar residuals. As can be observed, no specific trend can be distinguished in the noise, nor a specific amplitude.

2.2.3 The Timing Noise

The *timing noise* is a quasi-random variation of one or more rotational parameters in time scales of months or years. In general, it scales with the period derivative, $\dot{P}$, and thus it usually affects the timing of young pulsars, even though examples of timing noise can be observed, of lower amplitude, even in millisecond pulsars [115, 48]. In general the timing noise is reflected in the measurement of the second derivative of the rotational frequency, $\ddot{\nu}$, which presents values that are strongly inconsistent with those that would be expected from the standard evolution of the pulsar period with braking index $n = 3$ (see Section 1.1.3). From equation 1.4 it emerges an expected $\ddot{\nu}$ value:

$$\ddot{\nu} = n\frac{\dot{\nu}^2}{\nu}. \tag{2.8}$$

Assuming for an ordinary pulsar $\nu \sim 1$ Hz and $\dot{\nu} \sim 10^{-15}$ Hz s^{-1}, for $n = 3$ one finds $\ddot{\nu} \sim 10^{-30}$ Hz s^{-2}. These values are hard to measure but for the youngest pulsars. In some cases the timing procedure leads to much larger values than this, either positive or negative, and this is an index of the timing noise.

While it has proven difficult to find out what causes of the timing noise, some progress has been made on excluding some possible origins. It is not to be due to effects introduced by pulsar timing packages, nor the observatories or receiver systems [104, 102]. The same authors concluded that it is not caused by off-line processing either. [51] found that the timing noise is not correlated with height above the Galactic plane, luminosity or pulse shape changes. The effects of interstellar or interplanetary DM variations do not seem to cause it either. The physical models to explain the timing noise can be divided into those intrinsic to the pulsar or related to the companion and those that are extrinsic. Among the intrinsic models, it is suggested that rotational irregularities might arise from a random walk process that involves unresolved step functions in the pulse phase, spin frequency or frequency derivative [39]. Various models are based on the superfluid interior of the neutron star affecting the pulsar rotation, or on the neutron star undergoing some precession, which would explain the sinusoidal features observed in some cases, or variations in the outer magnetosphere that give rise to changes in the braking torque which will lead to a random walk in the rotational frequency. Any unmodeled orbiting companion could cause timing noise-like behavior. Extrinsic causes such as terrestrial clock errors, inaccuracies in the solar system ephemeris and even gravitational waves can be responsible for noise in the residuals. If this

happened, however, one would observe it in different pulsars with a similar trend.

In order to remove the timing noise from the data, it is possible to include higher order frequency derivatives in the timing model (see Section 2.2.1). Many orders can be necessary to remove the noise. A more refined method that has been implemented in the latest versions of the radio softwares used to analyze pulsar data is the *FITWAVES* technique [103, 104, 70]. The long term behavior is modeled by a sum of harmonically correlated waves which are subtracted to the residuals before the rest of the analysis. This will not affect periodicities like, for example, a sinusoid of growing amplitude produced by the proper motion which can be successively retrieved. This same innovative procedure has ben applied for the first time in gamma-ray timing analysis by our group on *AGILE* data (see Section 2.5.3).

2.3 Gamma-Ray Pulsars' Observations

The main aim of this Thesis has been the characterization of pulsars in gamma-rays. I mainly operated on data from the Italian satellite *AGILE*, being a member of the *AGILE* Team and *AGILE* Pulsar Working Group, so I will mostly concentrate on data reduction and analysis from the *AGILE* observations. I also worked on data from the *Fermi*-LAT satellite and the *MAGIC* telescope, which will be presented in their context. Details on the operations of the three telescopes are in the following.

2.3.1 Gamma-Ray Astronomy

The gamma radiation is produced by non-thermal processes, originated in interactions by high-energy particles. In general, in the case of diffuse radiation, the emission comes from the interaction between the cosmic rays and the ISM. If the emission comes from discrete sources, then the emission is due to the curvature radiation, non-thermal synchrotron, Inverse Compton (IC) or non-thermal Bremsstrahlung mechanisms.

The gamma-rays can only be observed from space up to about 30 GeV. In April 2007, almost ten years after the demise of the *CGRO*, the Italian Space Agency (ASI) launched the *AGILE* satellite for gamma-ray astronomy. In June 2008 the NASA launched its own heir of the *EGRET* telescope: formerly the *Gamma-rays Large Area Space Telescope, GLAST* then dubbed *Fermi*-LAT satellite after the successful launch. A dedicated description of the two telescopes is presented in the next two Sections.

The observation at Very High Energies (VHE, above ~ 50 GeV) is not feasible from space, due to the low fluxes involved, so it is performed from Earth using Ionizing Atmospheric Cherenkov Telescopes (IACTs), whose primary scope is to collect shower images, focusing the Cherenkov light emitted by atmospheric shower particles during their passage through the atmosphere. They make use of the Cherenkov light produced in the atmosphere by transversing cascades of the particles that are originated by the incoming gamma-ray when passing the higher layers of the magnetosphere. Three major telescopes are at present operating at the VHE: *MAGIC* in the Canary Islands, *HESS* in Namibia and *VERITAS* in Arizona. They operate in slightly different ranges between around 50 GeV up to 50 TeV. The *MAGIC* telescope, on whose data part of the work of this Thesis is based, is described in more detail in Section 2.3.4.

2.3.2 The AGILE Satellite

The *Astro-rivelatore Gamma a Immagini LEggero* (*AGILE*) is an Italian satellite which uses the new solid state detectors' techniques. As its name says, it is extremely light (it weighs only ~ 100 kg) and nonetheless efficient in the the detection and monitoring of the gamma-ray sources between 30 MeV and 50 GeV. The energy interval is similar to the *EGRET* one but the field of view much wider: 1/5 of the sky. The system is designed to have a very good angular resolution (with an accuracy for the position determination of a source of $\sim 5' - 20'$ for the bright sources) and, as said, a large field of view ($\gtrsim$2 sr), with a sensitivity comparable to *EGRET*'s for point sources on-axis and even better than *EGRET*'s for off-axis sources. The basic concept of *AGILE* is an integrated instrument constituted by three detectors with a large detection band and with imaging capabilities. The three detectors are: the *GRID*, *Super-AGILE* and the *Mini-Calorimeter*. An anti-coincidence system surrounds the whole instrument along 5 parts (upwards and laterally) and it separates gamma-rays from particles: the plastic scintillators collect the spurious signals, not coming from the gamma-ray radiation, and they are conveyed towards the photomultipliers, which communicate to the read-out system that the instrument is being passed by a high energy charged particle and not radiation. *AGILE* electronics allows fast readout operations and data-processing.

Among the three instruments, the *Gamma-Ray Imaging Detector* (*GRID*) is the main detector and the one that has been used for the purposes of this work. Sensitive to the energy band between 30 MeV and 50 GeV, it is made of a silicon

tracker and a mini-calorimeter of cesium iodide (CsI). The silicon layers give the *x* and *y* coordinates of the charged particles for each pair, as it crosses the *GRID* and all of them in the end keep track of the path, so as to reconstruct the arrival direction of the initial photon. The signal from the silicon tracker goes to the readout system. The mini-calorimeter helps determining the total energy of the incident photon. The *angular resolution* of the *GRID* at 1 GeV, with a containment radius of 67% is lower than 0.5° with a positioning capability of 5'–20'. The nominal *time resolution* is $\sim 1\mu$s with a dead time of ≤ 200 μs. The *energy resolution* combining tracker and mini-calorimeter is $\Delta E/E \sim 1$ at 200 MeV and even better below 100 MeV (see also Chapter 3). The *GRID* has an *effective area* of ~ 500 cm^2 which is dependent on the energy and incident angle of the collected photon, which decreases for angles $> 60^\circ$ off-axis.

The *AGILE* spacecraft was launched on April 23 2007 and placed in a Low Earth Orbit (LEO) at ~ 535 km of mean altitude with an inclination of 2.5°: Earth occultation strongly affects the exposure along the orbital plane, as well as a high particle background rate during the South Atlantic Anomaly (SAA) transits. However, the exposure efficiency is $> 50\%$ for most *AGILE* revolutions. *AGILE* pointings consist of long exposures (typically lasting 10- 30 days) slightly drifting ($\leq 1^\circ$/day) with respect to the starting pointing direction in order to match solar-panels illumination constraints. The relatively uniform values of the effective area and point-spread function (PSF) within $\sim 40^\circ$ from the center of the Field of View (FoV) of the *GRID* allow for one-month pointings without significant vignetting in the exposure of the target region. In late October 2009, *AGILE* started observing in spinning mode due to reaction wheel failure. This failure is not affecting *AGILE*/*GRID* sensitivity and pulsar observations although the new spinning mode required calibration revisions.

2.3.3 The Fermi - Large Area Telescope

The Large Area Telescope (*Fermi*-LAT, hereafter LAT), the primary instrument on the *Fermi Gamma-ray Space Telescope* mission, is an imaging, wide FoV, high-energy gamma-ray telescope, covering the energy range from below 20 MeV to more than 300 GeV. The LAT was built by an international collaboration with contributions from space agencies, high-energy particle physics institutes, and universities in France, Italy, Japan, Sweden, and the United States. The LAT is a pair-conversion telescope with a precision tracker and calorimeter, each consisting

of a 4×4 array of 16 modules, a segmented anti-coincidence detector that covers the tracker array, and a programmable trigger and data acquisition system. The calorimeters depth and segmentation enable the high-energy reach of the LAT. The aspect ratio of the tracker (height/width) is 0.4, allowing a large FoV (2.4 sr) and ensuring that most pair-conversion showers initiated in the tracker will pass into the calorimeter for energy measurement.

Fermi-LAT was launched into a LEO and, after a six-week commissioning phase, began nominal sky-survey observations on 2008 August 11. The LAT, the main instrument on board Fermi, is a pair-production telescope [28] sensitive to gamma-rays from 20 MeV to at least 300 GeV with on-axis effective area > 1 GeV of ~ 8000 cm^2, exceeding that of *EGRET* by a factor of about 5. In survey mode, it observes the entire sky every 3 hr. The LAT was tested in the initial 35 days in on-orbit verication that included sky-survey tuning and pointed-mode tuning on Vela, from 2008 June 30 to August 3, as well as the initial 15 weeks of sky survey, from 2008 August 3 to November 16.

During its first three years of operation, *Fermi*-LAT has provided an unprecedented view of the high-energy gamma-ray sky. More than 70% of the photons detected by the LAT are produced in the interstellar space of our Galaxy by interactions of high-energy cosmic rays (CRs) with matter and low-energy radiation fields. An additional diffuse component with an almost isotropic distribution, and therefore thought to be extragalactic in origin, accounts for another sizable fraction of the LAT photon sample. The rest consists of sources detected by the LAT from a variegate zoo of objects including active galactic nuclei and normal galaxies, pulsars and their relativistic wind nebulae, globular clusters, binary systems, shock-waves remaining from supernova explosions and nearby solar-system bodies like the Sun and the Moon. The first *Fermi*-LAT catalog (1FGL), based on 11 months of data, comprised 1451 sources, with respect to the 271 of the third *EGRET* catalog (3EG). After 24 months of observations, the second catalog released on July 2011 contains 1873 sources detected and characterized in the 100 MeV to 100 GeV range.

2.3.4 Observing at Very High Energies: science with *MAGIC*

The 17 m diameter *Major Atmospheric Gamma Imaging Cherenkov-telescope*, *MAGIC*, is a state of the art instrument for exploring the very high energy (VHE) gamma-ray sky. It is located on the Roque de los Muchachos Observatory, in La Palma (Canary Islands, Spain). *MAGIC* was built and is operated by a large

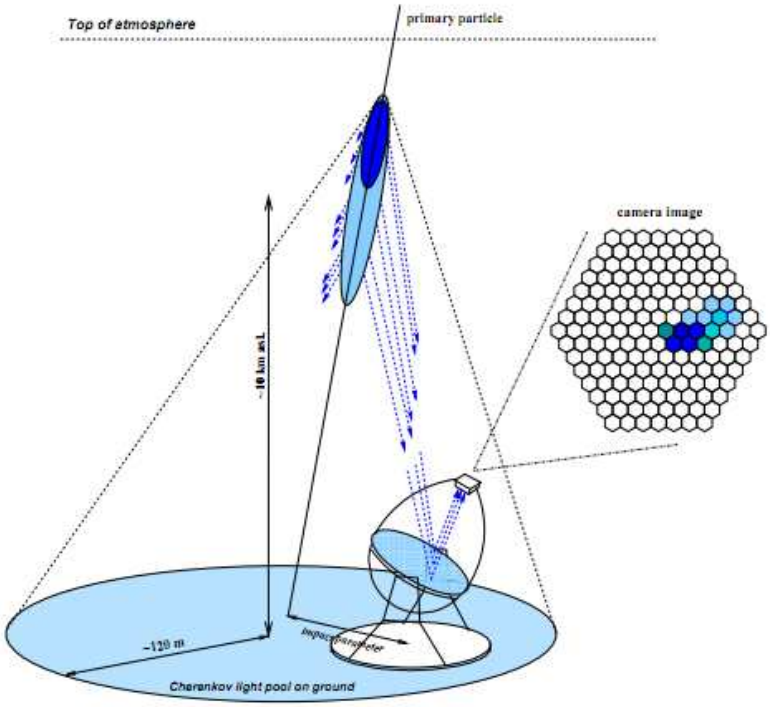

Figure 2.4 Schematics of the IACT detection of atmospheric showers. When the primary particle interacts in the top layers of the atmosphere, an air shower of particles is generated, characterized by a head (dark blue) and a tail (light blue). From the shower, the Cherenkov photons (blue lines) propagate to the ground at increasing angle with increasing shower development and atmospheric depth. The photons are reflected onto the focal plane at a distance from the center of the camera which reflects the shower impact parameter, i.e. the distance from the telescope axis. The camera is ”pixelized” and the image can be reconstructed. Figure from [139] .

international collaboration. A gamma-ray source emitting at a flux level of 1.6% of the Crab Nebula can be detected at a 5σ significance level in 50 hours of observations. The relative energy resolution above 100 GeV is better than 30% and the angular resolution is $\sim 0.1^{\circ}$. The construction of a second telescope is now complete and *MAGIC* started stereoscopic observations after the commissioning phase of MAGIC-II in mid-april 2009.

MAGIC works by detecting the faint flashes of Cherenkov light produced when gamma-rays (or CRs) plunge into the Earth atmosphere and initiate showers of secondary particles. The Cherenkov light emitted by the charged secondary particles is reflected by the telescope mirror and an image of the shower is obtained in the telescope camera (see Figure 2.4). An off-line analysis of the shower images allows the rejection of the hadronic CR background, the measurement of the incoming direction of the gamma-rays, and the estimation of their energy. The *MAGIC* telescope was built with the aim of achieving the lowest possible energy threshold, and since 2004 it operates with the lowest threshold worldwide, namely $\sim$ 50 GeV. An even lower threshold was achieved with a new trigger concept, the sum-trigger (see e.g. [146] and references therein), which provides a better discrimination of the faint flashes of Cherenkov photons from the night-sky background and made it possible to reach a threshold of 25 GeV and to detect pulsed emission from the Crab pulsar (see [18] and Section 3.5).

2.4 Timing a Pulsar in Gamma-Rays

The basics of pulsar timing in gamma-rays are given, mainly referred to the analysis as it is done using data collected from the *AGILE* telescope. The techniques are similar to those employed in their analysis by all gamma-ray telescopes

Pulsar data were collected during the mission Science Verification Phase (SVP; 2007 July - November) and early pointings (2007 December - 2008 April) of the AO 1 Observing Program. It is worth noting that a single *AGILE* pointing on the Galactic Plane embraces about one-third of it, allowing for simultaneous multiple source targeting (e.g., the Vela and Anti-Center regions in the same FoV with Crab, Geminga, and Vela being observed at once; see Figure 2.5). The *AGILE* Commissioning and SVP lasted about seven months from 2007 April 23 to November 30, also including Instrument Time Calibration. On 2007 December 1, baseline nominal observations and a pointing plan started together with the Guest Observer program AO 1. Timing observations suitable for pulsed signal analysis of

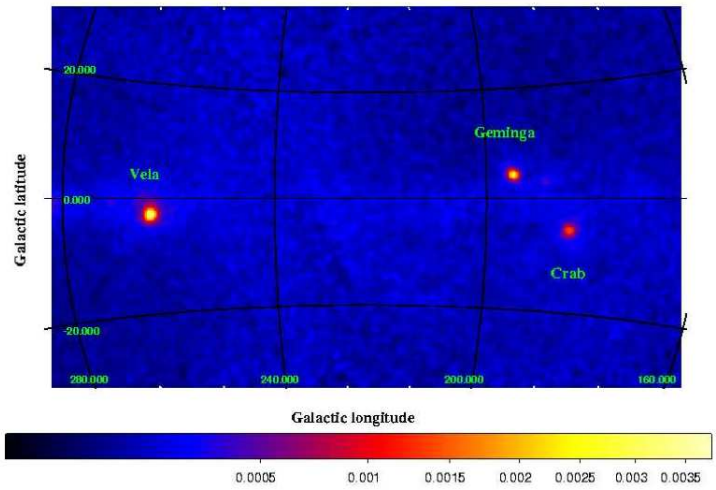

Figure 2.5 Gaussian-smoothed *AGILE* intensity map ($\sim 120^\circ \times 60^\circ$, units: ph cm^{-2} s^{-1} sr^{-1}, $E > 100$ MeV) in Galactic coordinates integrated over the observing period (2007 July 132008 April 10) and centered at $l = 223^\circ$, $b = 0^\circ$. The *AGILE* field of view (radius $\sim 60^\circ$) can embrace in a single pointing Vela ($l = 263.6^\circ$, $b = -2.8^\circ$), Geminga ($l = 195.1^\circ$, $b = 4.3^\circ$) and Crab ($l = 184.6^\circ$, $b = -5.8^\circ$) as well as diffuse emission from the Galactic Disk.

the Vela pulsar started in mid 2007 July (at orbit 1146) after engineering tests on the payload.

2.5 *AGILE* New Techniques for Gamma-Ray Timing

Data screening, particle background filtering, event direction and energy reconstruction are performed by the *AGILE* Standard Analysis Pipeline at $E > 100$ MeV. Observations affected by coarse pointing, non-nominal settings or intense particle background (e.g. orbital passages in SAA), and albedo events from the Earths limb were excluded from the processing. A specific optimization on the events extraction parameters is performed for each target in order to maximize the SNR for a pulsed signal. The optimal event extraction radius around pulsar positions varies as a function of photon energy (and then it is related to pulsar spectra) according to the PSF. However, for $E > 100$ MeV broadband analysis, a fixed extraction radius of $\sim 5^\circ$ (a value slightly higher than the PSF 68% containment radius) produces comparable results with respect to energy-dependent extraction.

Quality flags define different *GRID* event classes. The G event class includes events identified with good confidence as photons. Such selection criteria correspond to an effective area of ~ 250 cm^2 above 100 MeV (for sources within

30° from the center of the FoV). The L event class includes events typically affected by an order of magnitude higher particle contamination than G, but yielding an effective area of ~ 500 cm^2 at $E > 100$ MeV, if grouped with the G class. We performed our timing analysis looking for pulsed signals, using both G class events and the combination of G+L events. In general, the SNR of the pulsed signal is maximized using photons collected within $\sim 40 - 60°$ from the center of the *GRID* FoV and selecting the event class G. For very strong sources, such as Vela, or sources located in low background regions, it is also possible to include photons in the $40 - 60°$ off-axis range and belonging to the G+L event class typically improving the count statistics by up to a factor of 3 (obviously also implying a much higher background), without affecting or even improving the detection significance.

The corresponding total exposure was calculated with the *GRID* scientific analysis task AG_ExpmapGen according to the above parameters. Summing up the photon numbers, we see that the overall photon statistics accumulated during the first year of *AGILE* (accounting for background contamination) is comparable with that collected by *EGRET* for the same pulsars. A maximum likelihood analysis (ALIKE task) on the *AGILE* data from the sky areas containing the gamma-ray pulsars yields source positions, fluxes, and spectra. We also calculate the pulsed flux starting from the pulsed counts and compare it with that obtained from the spacial analysis: it will typically be affected by higher errors, but it accounts for only the flux actually coming from the pulsar and not contaminations from the pulsar wind nebula or supernova remnant, or nearby underlying sources.

2.5.1 The Fundamental Role of the Radio Timing

A gamma-ray telescope typically will not be able to collect a large number of photons for each observation. A pulsar emits a few gamma-ray photons compared to the number of rotations. Even for a pulsar like the Crab, among the three brightest in the gamma-ray sky, only one photon is received over hundreds of rotations. Even a new generation telescope like *AGILE*, therefore, is helped by, and sometimes cannot operate without, the radio observations. It has to be noted that *Fermi*-LAT, with its large effective area, has been optimized to be also able to perform a blind search (see [29] for details) which has actually led to the discovery of a number of new pulsars not previously known in radio [6, 196]. Even in the *Fermi*-LAT's case, though, the radio support leads to a more accurate characterization of the light curves.

The limited statistics makes it impossible to use in the gamma-ray band

the same methods that are used in the radio to look for periodicities: direct resolution methods such as the FFT and the folding (see Section 2.1.2) are hardly efficient to detect a pulsed signal in gamma-rays. A solution to this problem is found in combining accurate and intensive radio observations to long high-energy observations. The long observing times are needed to collect a statistically significant number of photons; the analysis of radio pulsars provides extremely accurate rotational ephemerides (see Section 2.2.2) which make it possible to obtain the rotational phase of each of the arriving photons. At this point the collected gamma-ray photons are all used to produce a single light curve and, in the favorable cases, this leads to enough statistics as to be able to recognize a pulsed signal. Even after the detection of a new gamma-ray pulsar, in order to keep observing, it is still necessary to fold the photons using the ephemerides obtained from the radio observations.

In most cases the pulsars observed in gamma-rays are young and they present glitches and timing noise (see Sections 1.1.4 and 2.2.3). Their effects are relevant in the timing: the noise ”pollutes” the residuals and this makes the evaluation of the parameters of a pulsar less precise. The glitches provoke jumps in the rotational period, which bring to a discontinuity in the data-set: the residuals pre- and post-glitch cannot be aligned unless the glitch is fitted for. Seeing as pulsars, and in particular those observed by gamma-ray telescopes, are affected by such timing irregularities, the ephemeris relative to a given epoch cannot be extrapolated for a time-span longer than a few months. It is thus required to continuously observe the pulsars in the radio, to have a thorough coverage of the gamma-ray telescope observations. In summary, the radio timing of known or candidate pulsars, before and during its observations, is fundamental for the operation of a gamma-ray telescope.

In order to perform the *AGILE* timing calibration through accurate folding and phasing, pulsar timing solutions valid for the epoch of *AGILE* observations were required. Thus, a dedicated pulsar monitoring campaign (that will continue during the whole *AGILE* mission) was undertaken, using two telescopes (namely Jodrell Bank and Nançay) of the *European Pulsar Timing Array* (*EPTA*), as well as the Parkes radio telescope of the *Commonwealth Scientific and Industrial Research Organisation* (*CSIRO*) *Australia Telescope National Facility* (*ATNF*) and the 26 m Mt Pleasant radio telescope operated by the University of Tasmania. In particular, the observations of the Vela Pulsar have been secured by the Mt. Pleasant Radio

Observatory. Data were collected at a central frequency of 1.4 GHz. Given the pulsar brightness, it is possible to extract a pulse ToA about every 10 s, so that a total of 4098 ToAs are obtained for the time interval between 2007 February 26 (MJD 54,157) and 2008 March 23 (MJD 54,548), encompassing the whole time span of the *AGILE* observations.

The timing of all pulsars in radio is performed using the TEMPO2 software [104, 70]. It first converts the topocentric ToAs to solar-system barycentric ToAs at infinite frequency (using the Jet Propulsion Laboratory (JPL) DE405 solar system ephemeris) and then performs a multi-parameter least-square fit to determine the pulsar parameters. The procedure is iterative and improves with longer timescales of observations. An important feature developed by TEMPO2 is the possibility of accounting for the timing noise in the fitting procedure. TEMPO2 corrects the effects of the timing noise on the residuals by modeling its behavior as a sum of harmonically correlated sinusoidal waves that is subtracted from the residuals (see Section 2.5.3).

2.5.2 Folding and Light Curve Generation

In this section, the timing procedures we have adopted will be described. They have been implemented with two aims: to verify the timing performances of *AGILE* and to maximize the quality of the detection of the targets.

AGILE on-board time is synchronized to Universal Coordinate Time (UTC) by the Global Positioning System (GPS) time sampled at a rate of 1 Hz. Arrival time entries in *AGILE* event list files are then corrected to Terrestrial Dynamical Time (TDT) reference system at a ground segment level. In order to perform the timing analysis, they also have to be converted to Barycentric Dynamical Time (TDB) reference and corrected for arrival delays at SSB. This conversion is based on the precise knowledge of the spacecraft position in the solar system frame. To match the instrumental microsecond absolute timing resolution level, the required spacecraft positioning precision is ≤ 0.3 km. This goal is achieved by the interpolation of GPS position samples extracted from telemetry packets. Earth position and velocity with respect to SSB are then calculated by JPL planetary ephemeris DE405. All the above barycentric corrections are handled by a dedicated program (implemented in the *AGILE* standard data reduction pipeline) on the event list extracted according to the criteria described in Section 2.4.

As said, pulsed signals in *GRID* gamma-ray data cannot be simply found

by Fourier analysis of the photon SSB arrival times, since the pulsar rotation frequencies are 4–5 orders of magnitude higher than the gamma-ray pulsars typical count rates (10–100 counts/day). The determination of the pulsar rotational parameters in the gamma ray must then start from at least approximate knowledge of the pulsar spin ephemeris, provided by observations at other wavelengths. Standard epoch folding is performed over a tridimensional grid centered on the nominal values of the pulsar spin frequency ν_0 and of its first- and second-order time derivatives, $\dot{\nu}_0$ and $\ddot{\nu}_0$, as given by the assumed (radio or X-ray) ephemeris at their reference epoch $t_0 = PEPOCH$. The axes of the grid are explored with steps equal to $1/T_{span}$, $2/T_{span}^2$, and $6/T_{span}^3$ (all of them oversampled by a factor of 20), where T_{span} is the time span of the gamma-ray data. For any assigned $[\nu;\dot{\nu};\ddot{\nu}]$, the pulsar phase Φ^* associated to each gamma-ray photon is determined by the expression

$$\Phi^* = \Phi_0 + \nu\Delta T + \frac{1}{2}\dot{\nu}\Delta t^2 + \frac{1}{6}\ddot{\nu}\Delta t^3, \tag{2.9}$$

where $\Delta t = t - t_0$ is the difference between the SSB arrival time of the photon, t, and the reference epoch t_0 of the ephemeris and Φ_0 is a reference phase.

A light curve is formed by binning the pulsar phases of all the phases of the photons and plotting them in a histogram. Pearson's χ^2 statistics is then applied to the light curves resulting from each set of spin parameters, yielding the probabilities of sampling a uniform distribution. These probabilities $\mathscr{P}(\nu;\dot{\nu};\ddot{\nu})$ are then weighted for the number of steps $\mathscr{N}_{st}$ over the grid, which has been necessary to reach the set $[\nu;\dot{\nu};\ddot{\nu}]$, starting from $[\nu_0;\dot{\nu}_0;\ddot{\nu}_0]$. The maximum value over the grid of $\mathscr{S} = 1 - \mathscr{N}_{st}\mathscr{P}(\nu;\dot{\nu};\ddot{\nu})$ finally determines which are the best rotational parameters for the target source in the surroundings of the given ephemeris. Of course, the higher the value of $\mathscr{S}$, the higher is the statistical significance of a pulsating signal. We note that this approach allows us to avoid any arbitrariness in the choice of the range of the parameters to be explored, which otherwise can affect the significance of a detection.

The effective time resolution of *AGILE* light curves results from the combination of the different steps involved in the processing of gamma-ray photons arrival times. The on-board time tagging accuracy is a mere $\sim 1\mu$s, with negligible dead time. For comparison, the corresponding *EGRET* time tagging accuracy was $\sim 100\mu$s. The precise GPS space-time positioning of the *AGILE* spacecraft allows for the transformation from UTC to the SSB time frame (TDB) with only a moderate loss ($\leq 10\mu$s) of the intrinsic instrumental timing accuracy. The innovative folding technique which also accounts for pulsar timing noise (see next Section) also

reduces the smearing effects in the light curves, fully exploiting all the information from contemporary radio observations. In summary, the effective time resolution of the current *AGILE* pulsar light curves (and then multi-wavelength phasing accuracy assuming $t_{err} = 1\mu$s) is mainly limited by

$$\Delta t = \frac{P}{N} = \frac{\sigma^2(C_p + 2B)}{C_p^2}, \tag{2.10}$$

where P is the pulsar period, N is the number of bins in the light curve histogram, σ is the SNR, C_p are the pulsed counts and B are the background counts. In order to keep the average SNR of the light curve bins (during the on-pulse phase) at a reasonable level ($> 3\sigma$), the resulting effective time resolution is constrained to $200 - 500\mu$s. At present the best effective time resolution ($\sim 200\mu$s) is obtained for the 400 bin light curve of Vela (G+L class selection) although a 100 bin light curve is better suited to study pulse shapes and to search for possible weak features. The effective time resolution will obviously improve with exposure time as $\Delta t \propto T_{exp}^{-1}$.

2.5.3 Timing Noise Correction

An additional significant improvement in the detection significance has been obtained by also accounting for the pulsar timing noise (see Section 2.2.3) in the folding procedure. This exploits a tool of TEMPO2 [104, 70], namely the possibility if fitting timing residuals with a polynomial harmonic function ΔR in addition to the standard positional, rotational and (when appropriate) binary parameters [103]:

$$\Delta R(\Delta t) = \sum_{k=1}^{N} a_k \sin(k\omega\Delta t) + b_k \sin(k\omega\Delta t), \tag{2.11}$$

where N is the number of harmonics (constrained by precision requirements on radio timing residuals, as well as by the span and the rate of the radio observations), a_k and b_k are the fit parameters (i.e. the *WAVE* terms in the TEMPO2 ephemeris files), and $\omega = 2\pi(T_{radio}(1 + 4/N))^{-1}$ is the main frequency (i.e. $WAVE_{OM}$ in the TEMPO2 ephemeris files) related to the radio data time span T_{radio}.

If the spin behavior of the target is suitably sampled, the harmonic function ΔR can absorb the rotational irregularities of the source, in a range of timescales ranging from $\sim T_{radio}$ down to about the typical interval between radio observations. As an example, the peak-to-peak amplitude of the ΔR fluctuations for Crab related to the radio monitoring epochs 54,07454,563 MJD covering our *AGILE* observations is of the order of ~ 1 ms (see Figure 2.6), corresponding to a phase smearing of > 0.03, a

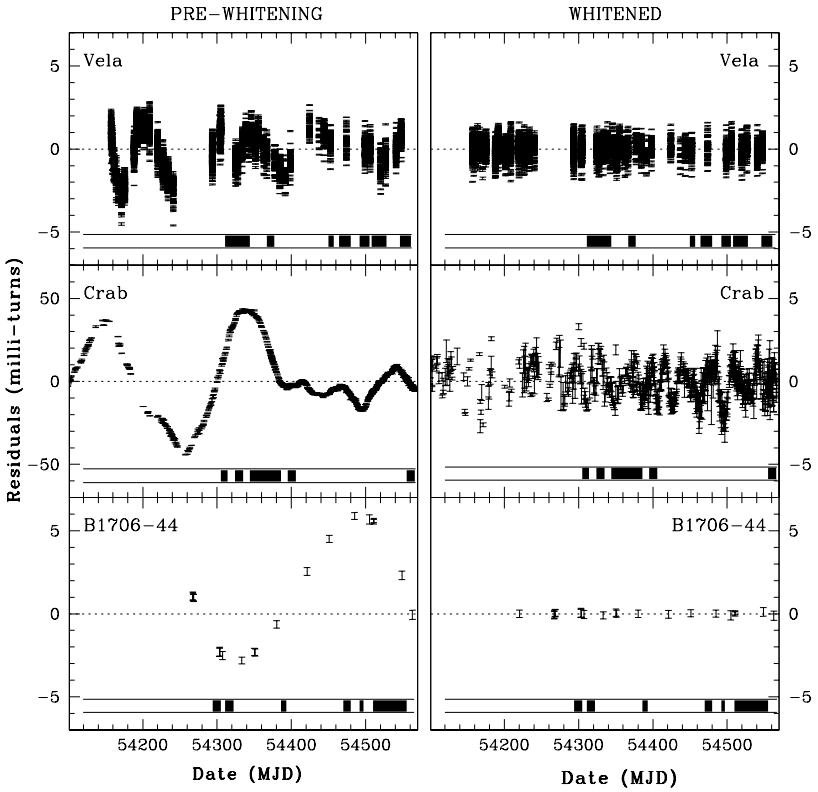

Figure 2.6 Post-fit timing residuals (in milli-turns) as a function of the Modified Julian Day resulting from the observation at 1.4 GHz of the three radio pulsars which are discussed in this paper: from the top Vela, Crab and PSR B1706–44. The panels in the left (right) column report the residuals of the best available timing solutions obtained over the data span not including (including) the correction of the timing noise via the use of the ΔR term (see Section 2.5.3). Note that for the Crab pulsar the scale on the vertical axis of the panel in the right column is amplified by a factor 10 with respect to that in the left panel. The time intervals corresponding to the useful *AGILE* pointings for each target are also given as the black sections of the bar at the bottom of each panel. .

value significantly affecting the time resolution of a > 50-bin light curve. Under the assumption that the ToAs of the gamma-ray photons are affected by timing noise like in the radio band, gamma-rays folding can properly account for ΔR, extending Equation 2.11 to

$$\Phi = \Phi_0 + (\nu + \dot{\nu}\Delta t + \frac{1}{2}\ddot{\nu}\Delta t^2)\Delta R \simeq \Phi_0 + \nu\Delta t(1 + \frac{\Delta R}{\Delta T}) + \frac{1}{2}\dot{\nu}\Delta t^2 + \frac{1}{6}\ddot{\nu}\Delta t^3 \quad (2.12)$$

This innovative phasing technique significantly improves the gamma-ray folding accuracy for young and energetic pulsars, especially when using long data spans, like those of the *AGILE* observations. Of course, the implementation of this procedure requires radio observations covering the time span of the gamma-ray observations making the radio monitoring described in Section 2.5.1 all the more important.

2.5.4 Gamma-Ray Folding of Long Data Spans

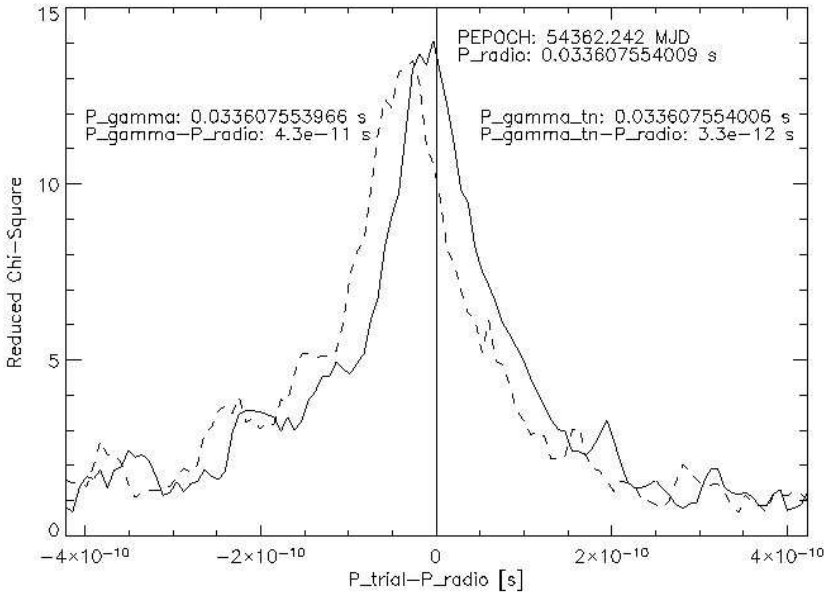

Figure 2.7 Effect of the timing noise correction on the significance of the detection and matching with radio parameters. The dashed line represents the period search result without the use of the timing noise correction; the full line represents the period search after the application of the timing noise correction.

Figure 2.7 shows the *AGILE* period search result for the Crab pulsar (corresponding to the MJD 54,305–54,406 observations, significantly affected by timing noise, as shown in Figure 2.6). The implementation of the folding method described in Section 2.5.2, including timing noise corrections as given by Equation

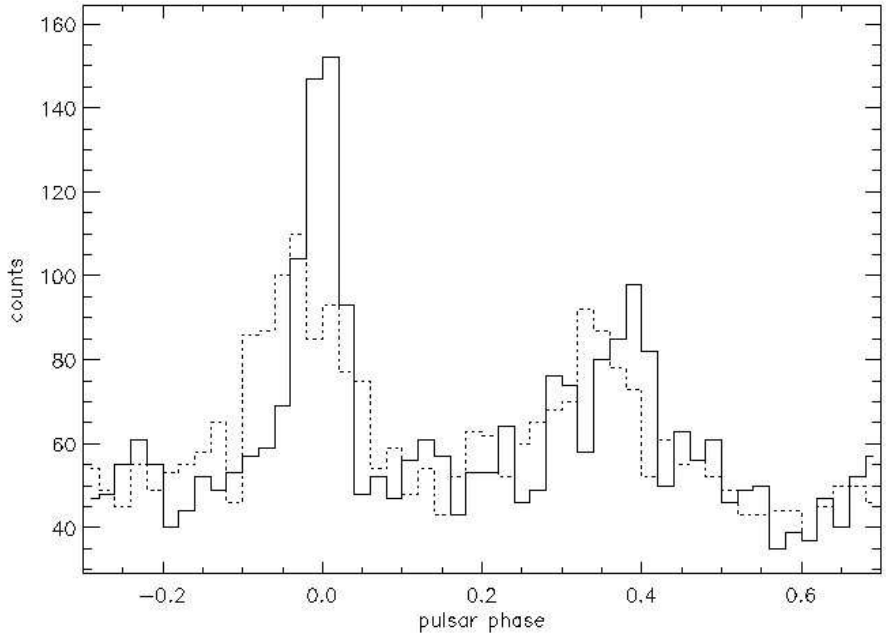

Figure 2.8 Effect of the timing noise correction on the pulsar light curve. As in the previous Figure, the dashed curve represents the result without the use of the timing noise correction, while the full line represents the light curve obtained after the application of the timing noise correction to the period search.

2.12, allowed for a perfect match between the best period resulting from gamma-ray data and the period predicted by the radio ephemeris with discrepancies $\Delta P_{Crab} \sim 3 \times 10^{-12}$ s, comparable with the period search resolution $r_{Crab} \sim 2 \times 10^{-12}$ s. This also represents an ultimate test for the accuracy of the on-board *AGILE* Processing and Data Handling Unit (PDHU), time management (clock stability in particular), and on-ground barycentric time correction procedure.

In order to verify the performances of the timing analysis procedure described, a crucial parameter to check is the difference between pulsar rotation parameters derived from radio, X-ray, and gamma-ray data. Despite the very satisfactory matching of the pulsar spin parameters found in radio (or X-ray) and gamma-ray (supporting the clock stability and the correctness of the SSB transformations), possible systematic time shifts in the long *AGILE* event lists could be, in principle, affecting phasing and must be checked. For example, a hypothetical constant discrepancy of t_{err} of the on-board time with respect to UTC would result in a phase shift $\Phi_{err} = (t_{err} \mathrm{modP})/P$, where P is the pulsar period. The availability of radio observations bracketing the time span of the gamma-ray observations (or of X-ray observations very close to the gamma-ray observations for the case of Geminga)

also allowed us to perform accurate phasing of multi-wavelength light curves. In doing so, the radio ephemeris reference epochs were set to the main peak of the radio light curves at phase $\Phi_{peak} = 0$. In view of Equations 2.11 and 2.12, this is achieved by setting $\Phi_0 = -\nu \sum_{k=1}^{N} b_k$ (typically, $\Phi_0 < 10^{-2}$).

Standard folding without the ΔR term implies radio-gamma period discrepancies one order of magnitude higher ($\Delta P_{Crab} \sim 4 \times 10^{-11}$ s). Moreover, it also lowers the statistical significance of the detection and effective time resolution of the light curve. For the Crab, the value of the Pearsons χ^2 statistic introduced in Section 2.5.2 (we quote reduced χ^2 values) goes from ~ 6.3 (when using the ΔR term) down to ~ 4.2 (ignoring the ΔR term) when folding the data into a 50-bin light curve (see Figure 4). Obviously, ignoring timing noise in the folding process would yield discrepancies (and light curve smearing) that are expected to grow when considering a longer observing time span. Thus, the contribution of timing noise should be considered both in high-resolution timing analysis and in searching for new gamma-ray pulsars.

Chapter 3

The New AGILE Sub-Millisecond View on Gamma-Ray Pulsars

In this Chapter, the first new results from *AGILE* pulsar observations are presented. These results, on the known gamma-ray pulsars (see next Section), were published in [173], to which I gave major contributions in the calibration and data analysis. The study of the Crab pulsar is completed with the observations performed with the *MAGIC* telescope. I participated to the last two works on the modeling of the Crab pulsar spectrum at the VHEs by *MAGIC*: [146, 147]. In particular, I contributed to the analysis of the *Fermi*-LAT publicly available data that provide the spectral points below the *MAGIC* energy range. Finally, pulsars B1055–52 (J1057–5226) and B1951+32 (J1952+3252), which belonged to the *AGILE* Guest Observer (GO) Program, have been most recently analyzed and the results presented here have not been published yet, but will appear in the *AGILE* Catalog of Gamma-Ray Pulsars that is in preparation. The Chapter, as well as this Thesis in general, concentrates on the results obtained by the *AGILE* satellite, as I mainly worked on proprietary data from the *AGILE* Team, but the same sources and some of the phenomena have been observed by *Fermi*-LAT as well. I do not exploit the *Fermi*-LAT observations, but notes and references will be given on them as well.

3.1 The Gamma-Ray Pulsars before *AGILE*

Among the $\sim$ 1800 known rotation-powered pulsars, mainly observed in the radio band, seven objects had been identified as gamma-ray emitters before 2007: Vela (B0833–45), Crab (B0531+21), Geminga (J0633+1746), B1706–44, B1509–58, B1055–52 and B1951+32 (see Section 1.5 and [216]. In addition, B1046–58 [114], B0656+14 [184] and J0218+4232 [128, 127] were reported with lower confidence

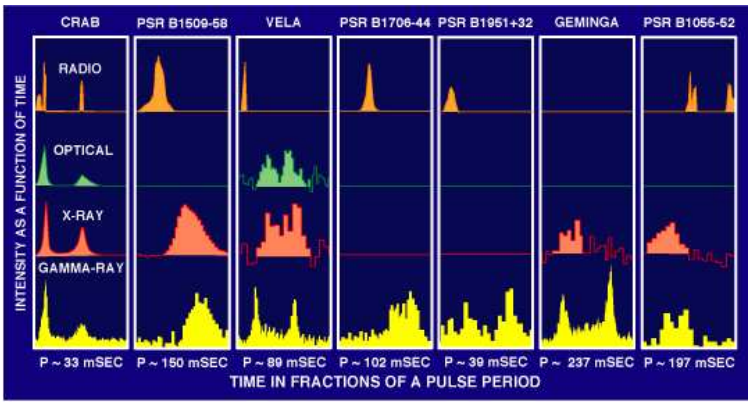

Figure 3.1 The seven RPPs firmly identified in gamma-rays before *AGILE*.

(probability of periodic signal occurring by chance in gamma-rays of $\sim 10^{-4}$).

In spite of the paucity of pulsars identifications, gamma-ray observations were already used as a a valuable tool for studying particle acceleration sites and emission mechanisms in the magnetosphere of the spin-powered pulsars.

Spin-powered pulsars were the only class of Galactic sources firmly identified by *CGRO/EGRET*. It was thought that some of the unidentified gamma-ray sources would turn out to be associated to young and energetic radio pulsars discovered in subsequent radio surveys [149, 123]. In fact, several unidentified gamma-ray sources had characteristics similar to those of the known gamma-ray pulsars (hard spectrum with high energy cutoff, no variability, possible X-ray counterparts with thermal/non-thermal component, no prominent optical counterpart), but they lacked a radio counterpart as well as a SNR and/or PWN association. Radio-quiet, Geminga-like objects had also been invoked but no identification had been confirmed at the time.

3.2 The Advent of *AGILE*

With about ten years since the last gamma-ray observations of pulsars, the improved time resolution of *AGILE* and the much longer observation campaigns, the opportunity arose to search for new features in the shape of the light curves of the known gamma-ray pulsars and to investigate the possible occurrence of variations in the gamma-ray pulsed flux parameters.

After nine months of observations in the frame of the SVP (2007 July - November, see Section 2.4) and of Scientific Pointing Program AO 1 (pointings 1 - 7, 2007 December 1 – 2008 April 10), *AGILE* reached $\sim 10,000$ pulsed counts from

the Vela pulsar and an exposure of the Vela region $\geq 10^9$ cm^2 s at $E > 100$ MeV, comparable to that of the nine-year lifetime of *EGRET* (although *AGILE* data had a higher residual particle background). An even better exposure (1.5×10^9 cm^2 s) was reached in the core region of the Galactic Plane ($l = 310^\circ - 340^\circ$), corresponding to the Southern Hemisphere. From PSR B1706–44, *AGILE* observed ~ 2400 pulsed counts up to April 2008, a factor 1.5 better counts statistics than *EGRET* for this source. For Crab and Geminga, an exposure level comparable with that obtained by *EGRET* was reached at the end of AO 1 pointing number 15 in the Anti-Center region (October 2008).

The following Sections will illustrate in detail how *AGILE* observations started to assess new features in the gamma-ray pulsars light curves. Narrower and better resolved main peaks were revealed, together with previously unknown secondary features, to be confirmed when more counts statistics would be available. *AGILE* allowed for a long monitoring of gamma-ray pulsar light curves shapes. We carefully looked for possible light curve variations by KS tests (two-dimensional Kolmogorof-Smirnoff test [KS]; [169, 74]). For each pulsar, different gamma-ray light curves (with 10, 20 and 40 bins) were obtained grouping contiguous data sets and requiring at least 30 counts bin^{-1} (300-1000 counts for each light curve). Each light curve was compared by KS test with each other and with the average shape corresponding to the entire data set. No pulse shape variation was detected with a significance $> 3\sigma$ on timescales ranging from 1 day (Vela) to few months (Crab, Geminga and PSR B1706–44).

3.3 The Vela Pulsar

The first pulsar to be discovered in the Southern hemisphere [132], the Vela pulsar (or PSR J0835–4510) is located at the center of the Vela SNR and it contributed to the identification of pulsars as the aftermath of the death of massive stars in the supernova explosion (SNE) and the result of their core collapse. Its age, 10^4 years, makes it a bridge pulsar between the very young (e.g. Crab) gamma-ray emitting pulsars and the old ones (e.g. PSR J1057-5226). Its emission at different wavelengths seems to be the superposition of different spectral components. Ten years after its discovery in the radio band, it was observed in the optical [225]. It was subsequently detected also at UV, X and gamma-rays. The Vela pulsar is the brightest persistent gamma-ray source of the sky. Its gamma-ray spectral properties, first highlighted with *EGRET* [112], make it more similar to the old gamma-ray

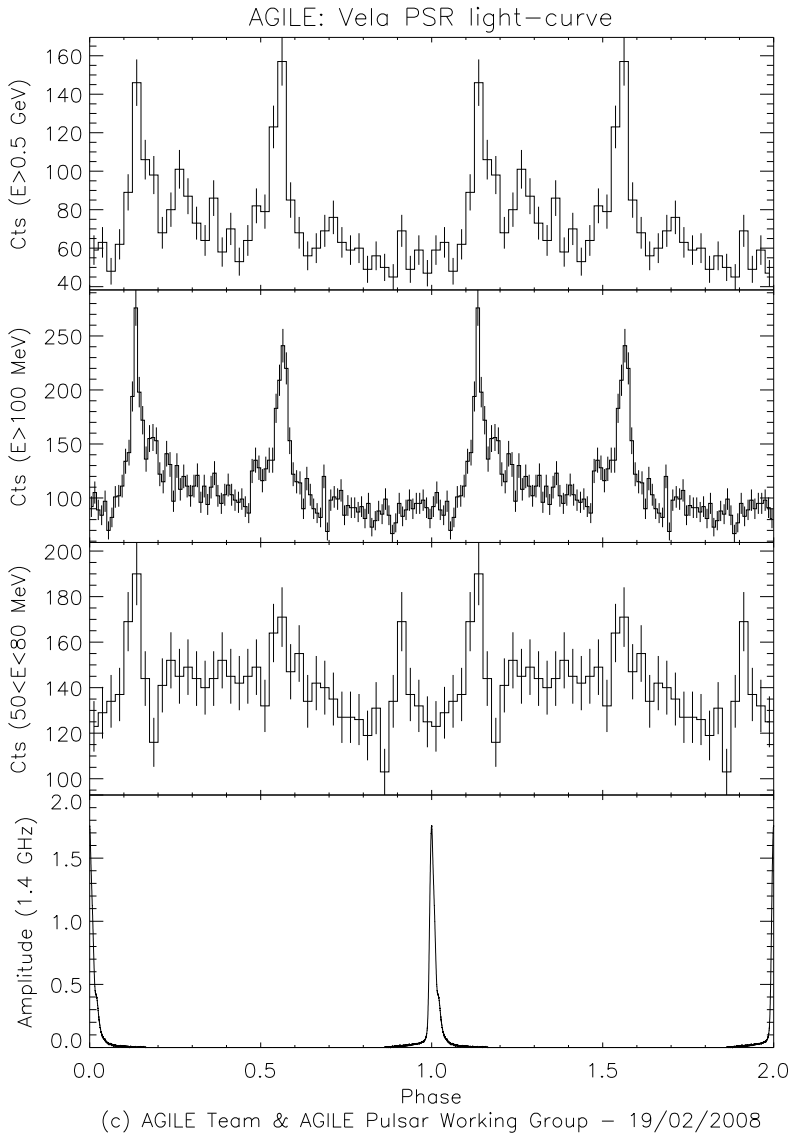

Figure 3.2 Vela pulsar light-curves ($P \sim 89.3$ ms) for different energy bands ($E < 100$ MeV, 40 bins, resolution: ~ 2.2 ms; $E > 100$ MeV, 100 bins, resolution: ~ 0.9 ms; $E > 1$ GeV, 20 bins, resolution: ~ 4.5 ms; G+L class events) obtained by integrating all available post-glitch data (5432054561 MJD). The radio ephemeris and the 8192 bins light-curve (bottom panel) are obtained by the analysis of ~ 4100 ToAs observed at Mt. Pleasant Radio Observatory in Tasmania (radio observation interval 5415754548 MJD).

pulsars than to the older ones.

The Vela light curves for different energy bands are shown in Figure 3.2. A Gaussian fit to the Vela main peak (P1) at $E > 100$ MeV provides a FWHM of 0.018 ± 0.002, centered at the rotational phase $\phi = 0.1339 \pm 0.0007$, consistent with the *EGRET* observations [112]. The apex of the main peak is resolved by *AGILE* with a width of ~ 0.8 ms and its apparent trail ($\phi = 0.13 - 0.3$) could be due to the occurrence of one or more secondary peaks. In fact, marginal evidence of a relatively narrow lower peak (P3) at $\phi \sim 0.25$ is present in the $E < 100$ MeV (3.3σ fluctuation with respect to the average interpulse rate) and in the $E > 1$ GeV light curves. P3 is located at the phase of the optical peak 1 [225] and also at the phase of a bump predicted in a TPC model [69], due to overlapping field lines from opposite poles near the light cylinder. In the outer gap model, this bump is the first peak of the light curve and also comes from very near the light cylinder. The peak at $\phi = 0.5 - 0.6$ (P2) in the $E > 100$ MeV light curve cannot be satisfactorily fit with a single Gaussian or a Lorentzian curve ($\chi^2_r > 3$), due to the possible presence of a bump at $\phi \sim 0.5$ (P2a). The phase separation between the main gamma-ray peaks $\Delta\phi = 0.426 \pm 0.002$, as well as that between the gamma-ray and the radio peak, are unchanged since the *EGRET* observations [112, 183]. In the $E < 100$ MeV band a secondary peak+valley structure (P4) appears at $\phi \sim 0.9$ ($\sim 4\sigma$ level). It is worth noting its symmetric position around the radio peak with respect to the main peak (P1) and a possible correlation of P4 with features seen in the X-ray light curves [151]; P4 also coincides with peak number 3 of the *RXTe* light curve [91]. *Fermi*-LAT observations [2] confirmed the presence of the structure in the second peak and also confirm the presence of a third peak (P3) in between P1 and P2, with a strong dependence on the energy range.

3.3.1 The Vela glitch of August 2007

During early *AGILE* observations, Vela experienced a weak glitch clearly detected in radio as a discontinuity in the pulsars spin parameters.

What is a Glitch

Glitches (see Section 1.1.4) are small ($\Delta\nu/\nu \sim 10^{-9} - 10^{-6}$) and sudden ($\lesssim$1 day) discontinuous increases in the pulsar frequency, often followed by a recovery (1100 days) to the pre-glitch frequency. About $\sim 6\%$ of pulsars are known to have shown glitches (see for example [73]), with a higher incidence of events in younger pulsars.

This phenomenon is potentially a very promising tool for probing the physics of the neutron star interiors [144]. Although no general consensus has been reached to date about the origin of the glitches, many models are based on the exchange of angular momentum between the superfluid neutron star core and its normal, solid, crust [191, 194, 20, 19].

Glitches in Gamma-Rays

This angular momentum transfer may excite *starquake* waves, propagating towards the neutron star surface. Since the magnetic field frozen in the crust is shaken, the resulting oscillating electro-magnetic potential could generate strong electric fields parallel to the magnetic field, which in turn would accelerate particles to relativistic energies, possibly emitting a burst of high-energy radiation.

The Episode of August 2007

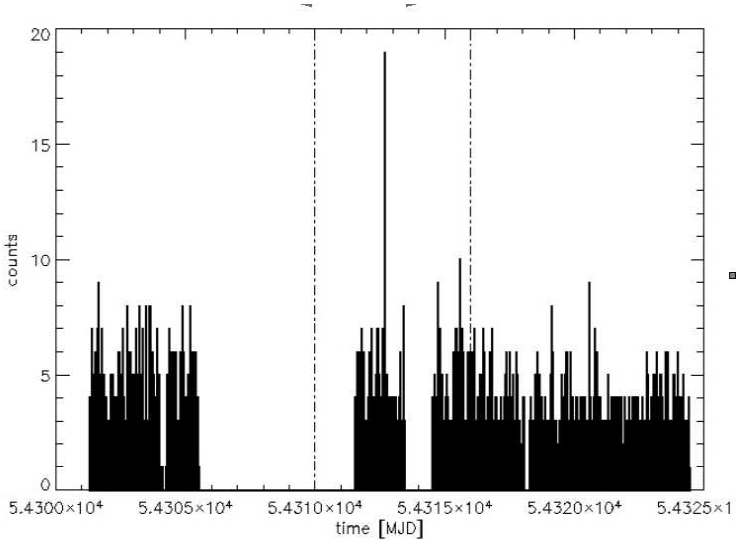

Figure 3.3 Unfolded Vela pulsar light-curve (4.5 min bin size, $E > 50$ MeV, G-class events). Dashed lines bracket glitch epoch uncertainty range (54313 ± 3 MJD). A $> 5\sigma$ count excess at ~ 54312.693 MJD could be associated to gamma-ray bursting emission from the glitch.

Since the first observation of a pulsar glitch in 1969 [182], Vela has shown ~ 10 major glitches. Due to its large field of view, the quest for possible gamma-ray bursting behavior due to a glitch is then an effective opportunity for *AGILE*. Despite the fact that the August 2007 glitch was a weak one ($\Delta\nu/\nu \sim 10^{-9}$), it was worthwhile to search for a signal in the *AGILE* data. The characteristic energy of a pulsar glitch can be roughly estimated from the associated pulsar frequency jump

$E_{glitch} = \Delta E_{rot} = 4\pi^2 I \nu \Delta\nu$, where I ($\sim 10^{45}$ g cm^2) is the neutron star moment of inertia. The corresponding expected gamma-ray counts would be:

$$C_\gamma^{glitch} = \eta \frac{E_{glitch} A_{eff}}{4\pi d^2 E_\gamma} \simeq 10^{11} \eta \frac{\Delta\nu}{\nu} \tag{3.1}$$

where $\eta = [0,1]$ is the unknown conversion efficiency of the glitch energy to gamma-ray emission, d (~ 0.3 kpc) is the pulsar distance, E_γ (~ 300 MeV) is the average gamma-ray photon energy assuming a spectral photon index $\Gamma = -2$, and A_{eff} is the *AGILE* effective area.

Even in the virtual limit assumption that the entire glitch energy could be driven into gamma-ray emission, a weak glitch with a frequency shift of $\Delta\nu/\nu = 1.3 \times 10^{-9}$, as that observed in August 2007, cannot produce a strong signal ($C_\gamma^{glitch} < 100 - 200$ counts), if the core fluence is spread in ~ 1 day. In fact, no excess on daily timescales was detected, although for much shorter timescales of $3 - 6$ minutes a $> 5\sigma$ excess (~ 15 counts) in the photon counts is seen at $\sim 54,312.693$ MJD (see Figure 3.3).

On the other hand, stronger Vela glitches, such as the one of 1988 Christmas [157], with a frequency shift of $\Delta\nu/\nu = 2 \times 10^{-6}$ could in principle produce more significant transient gamma-ray emission. Typical count-rate from Vela is $\sim 100 - 200$ counts day^{-1}, then a fluence of ≤ 1000 counts in ~ 1 day or less from the hypothetical gamma-ray glitch burst should be easily detectable. According to Equation 3.1 such a flux could arise from a glitch with $\Delta\nu/\nu \sim 10^{-7}$ (typical Vela glitch size), converting a relatively small fraction ($\eta \sim 0.1$) of its energy in gamma-rays. The chance occurrence of a strong Vela glitch in the *AGILE* field of view over three years of mission operations is of $\sim 20\%$.

3.3.2 Other Glitches

Other pulsars are known to glitch frequently and are observable in gamma-rays. Up to now no other glitch has been observed to emit in gamma-rays. [72] published a comprehensive study of the glitches of 102 pulsars observed since 1978 analyzing the Jodrell Bank database on the monitoring of 700 pulsars. They were able to give some insights and a phenomenological characterization of the glitches, together with a wealth of candidates in the northern sky for *AGILE* observations. A similar work on a smaller sample had been compiled from the Urumqi Observatory in China [226], and from the HartRAO in South Africa, for the Vela pulsar [40]. A monitoring program of glitches is active in a number of radio telescopes, including

the Hobart telescope in Tasmania, that does the monitoring of the Vela pulsar for the *AGILE* observations. Alerts are sent to the gamma-ray telescopes when a glitch is observed.

3.4 The Crab Pulsar

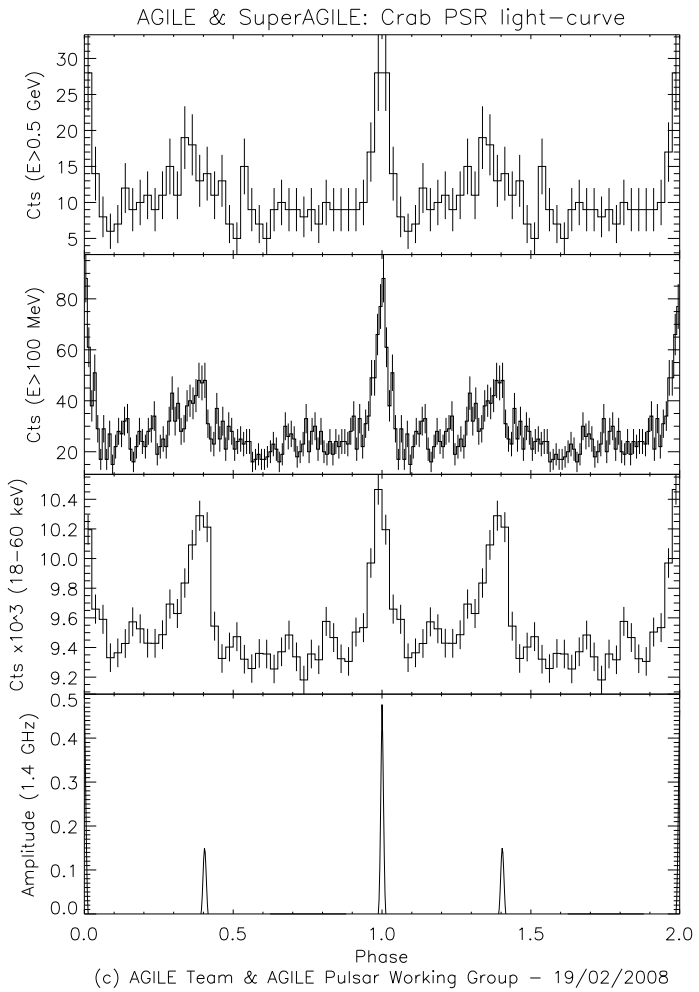

Figure 3.4 Crab pulsar light curves ($P \sim 33.1$ ms) for different energy bands ($E > 100$ MeV, 50 bins, resolution: ~ 0.7 ms; $E > 500$ MeV, 40 bins, resolution: ~ 0.8 ms; G class events) obtained by integrating all available data. The X-ray (1860 keV) *SuperAGILE* 50 bins light-curve is obtained from a ~ 41 ks observation taken at ~ 54361 MJD. The radio ephemeris and the 2048 bins light curve (bottom panel) are obtained by the analysis of 334 ToAs observed by Jodrell Bank and Nançay radio telescopes (observation interval 5407854566 MJD).

The Crab pulsar was not the first to be discovered, but it definitely has been one of the best and most studied. Its age is very well known, since its SNE was recorded by Chinese astronomers in 1054 a.C.. Being so young, and thus bright,

and so close, the Crab has widely been used as a prototype and a calibration star, although recent developments proved it far from stable and standard (see Section 3.4.1)

The Crab light curve for $E > 100$ MeV (Figure 3.4) shows a previously unknown broad feature at $\phi = 0.65 - 0.8$ (P3), in addition to the main peaks P1 and P2 ($\phi_{P1} = 0.999 \pm 0.002$, FWHM 0.054 ± 0.005; $\phi_{P2} = 0.382 \pm 0.008$, FWHM 0.14 ± 0.04). The probability of P3 of being a background fluctuation is of $\sim 10^{-4}$ (3.7σ). P2 could be possibly resolved into two sub-peaks in future longer observations. P3 is coincident with the feature HFC2 that appears in the radio profile above 4 GHz. [161] suggest that this peak may come from a lower emission altitude, near the polar cap. P3 is actually at a phase that could plausibly come from low altitude cascades in the slot gap model [164], the pairs from which may be also causing the HFC2 radio component(s), while P1 and P2 come from the high-altitude slot gap. *Fermi*-LAT subsequent observations [8], which showed extremely well resolved multi-wavelength light curves, present the canonical two peaks. They cannot claim the presence of P3, as they too observe it at a non significant 2.3σ level. The fact that *AGILE* and possibly also *MAGIC* [146] observe this same structure at the same frequency, constitutes at least an indication in favor of its presence, possibly of the variable kind (see Section 4.5.1).

According to the observations of *SAS-2*, *COS B* and *EGRET*, the ratio P2/P1 of the main peak intensities could present a variability pattern (possibly ascribed to the nutation of the neutron star) that can be fit with a sinusoid with a period of ~ 13.5 years [110, 183] although this is not required by *EGRET* data alone [218]. We observed a P2/P1 intensity ratio 0.66 ± 0.10 in good agreement with the value of ~ 0.59 predicted for 54350 MJD (for the energy range 50 MeV - 3 GeV). Unfortunately, our P2/P1 value is similar -within the errors- to the *EGRET* determination (~ 0.5): then an unambiguous assessment of the origin of this possible phenomenology will require measurements close to the epoch (56150 MJD) corresponding to the predicted maximum or the intensity ratio P2/P1 (~ 1.4). Variability should also be invoked to explain the possible detection of P3, which was never seen in the *EGRET* database in spite of an overall exposure comparable to that reached by *AGILE* up to April 2008. We note that the main peak intensity ratios computed for Vela ($P2/P1 = 0.91 \pm 0.07$) and Geminga ($P2/P1 = 0.8 \pm 0.1$) do not yield evidence of significant variations with respect to past observations [183].

3.4.1 Gamma-Ray Flares Coming from the Crab Region

The discovery by the *AGILE* satellite of a strong gamma-ray flare above 100 MeV from the Crab Nebula in September 2010 [210, 209] and the confirmation by the *Fermi-LAT* [41, 4] started a new era of investigation of the Crab Nebula and of the particle acceleration processes in general [224]. Three substantial gamma-ray flaring episodes from the Crab Nebula have been reported until March 2011 [209, 4]. The flaring activity was detected only in the gamma-ray energy range 100 MeV - a few GeV, and has been attributed to transient emission in the inner Nebula due to the lack of any variation in the pulsed (radio and high-energy) signal of the Crab pulsar or of any detectable alternative counterpart (e.g., [95, 54]). While a more detailed discussion on these episodes is presented in Chapter 6, here a brief description is provided of possible remote connections of this behavior with activity from the pulsar itself.

A Connection to the Timing Noise?

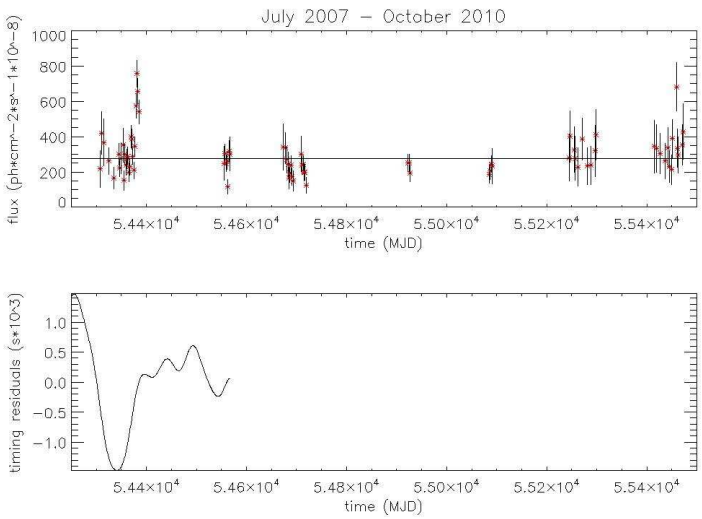

Figure 3.5 In the upper panel it is shown the flux of the *AGILE* observations of the Crab region from July 2007 to October 2010. In the bottom panel we show the corresponding residuals (see Section 2.2.2) of the pulsar timing which show considerable timing noise.

The origin of the flares does not seem to be in the pulsar itself. Still, the energy of the Nebula has its origin in the pulsar and so may the flaring episodes. No variability was observed in the radio domain, or at other wavelengths, coming from the pulsar. We analyzed the general behavior of the pulsar during this episode and in a longer time span.

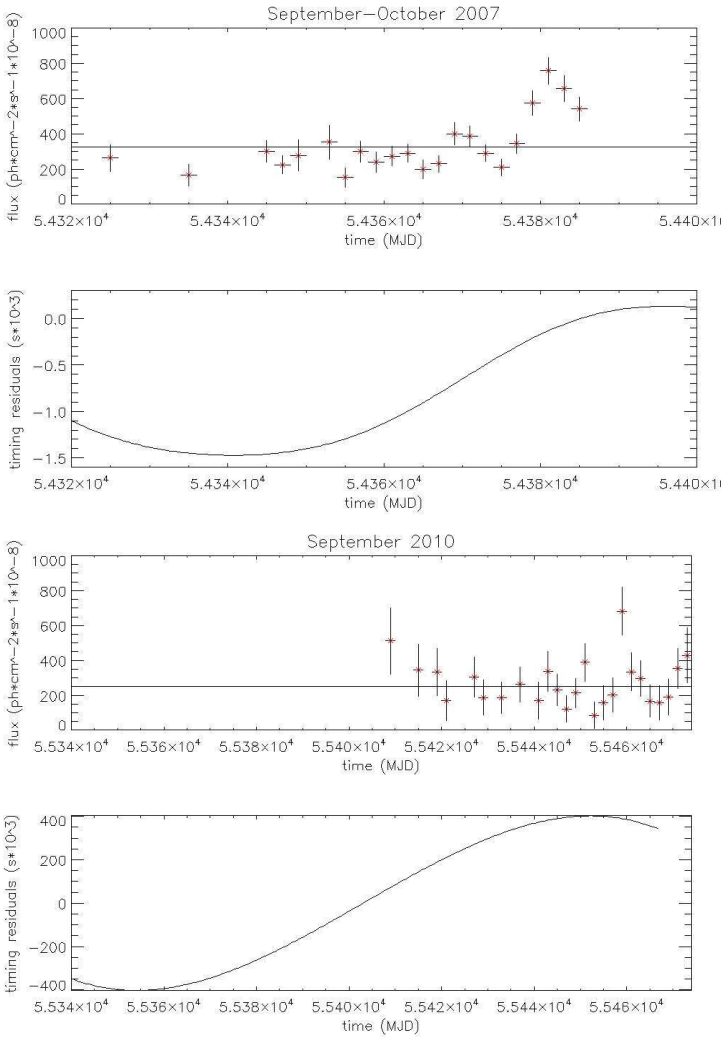

Figure 3.6 Same as the Figure 3.5, but with a close-up on the epochs of the flares, showing that the timing noise at both the times presents a growing trend.

The Crab pulsar is known to present strong timing noise (see Figure 3.5). The timing noise (see Section 2.2.3) is not an uncommon feature in young pulsars, but its origin is still debated and generally not understood. In the framework that flares as those recently observed by *AGILE* and *Fermi*-LAT are, too, not uncommon, we put together the long time timing noise information that we have collected for the Crab in three years of *AGILE* observations, and confronted them with the episodes of flaring variability observed up to now.

Figures 3.5 and 3.6 show the general trend in the timing noise and the corresponding gamma-ray behavior of the source. It can be noted that both times, when gamma-ray activity exploded, the timing noise showed an upwards trend. This association cannot be conclusive, but it makes it worth to continue following this line of investigation in the future efforts to explain the flaring activity of the Crab.

3.5 *MAGIC* observations of the Crab Pulsar

The first pulsar ever to be observed at energies above some tens of GeVs, the Crab confirms its peculiar nature after having been observed by the Cherenkov telescopes: *MAGIC* [18] and *Veritas* [223].

In spite of several attempts, no pulsar had ever been observed at energies $E > 60$ GeV, where the Earth-based Cherenkov telescopes are the most sensitive instruments. This suggested a spectral cutoff; that is, that the pulsars emission drops off sharply, between a few GeVs and a few tens of GeVs. The Crab pulsar is one of the best candidates for studying such a cutoff. Its spectrum had been measured by *EGRET* [216] up to $E \approx 5$ GeV without a clear cutoff being seen. Earlier observations from *MAGIC* [17] revealed a hint of pulsed emission at the 2.9 σ level above 60 GeV . In order to verify this result, a new trigger system was developed and installed, that lowered the threshold of *MAGIC* from ~ 50 GeV to 25 GeV [188].

The Crab pulsar was observed between October 2007 and February 2008: 22.3 hours of quality data where obtained and pulsed emission was detected above 25 GeV. The pulsed signal had an overall significance of 6.4σ with 8500 ± 1330 signal events. The $E > 25$ GeV profile (see Figure 3.7) showed two pronounced peaks at phases (with respect to the radio peak assumed to be at phase 0) $\phi = 0$ (P1) and $\phi = 0.3 - 0.4$ (P2). These peaks are coincident with those measured by the gamma-ray satellites (*EGRET, AGILE* and *Fermi*-LAT) at $E > 100$ MeV, but in the *MAGIC* light curve they have similar amplitudes at $E > 25$ GeV, while P1 is dominant at

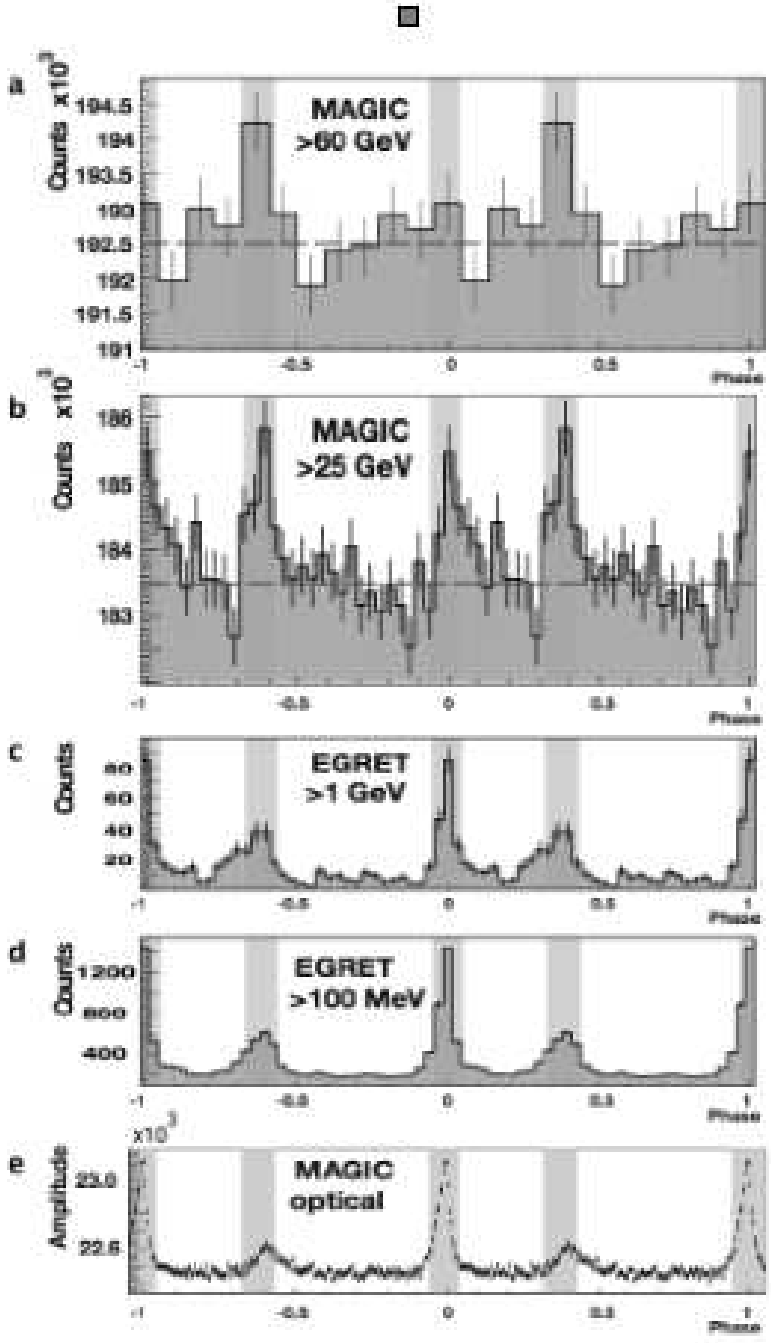

Figure 3.7 Crab pulsar pulsed emission in different energy bands, from [18]. The shaded areas show the signal regions for P1 and P2. (A) Evidence of an emission (3.4 s) greater than 60 GeV for P2, measured by *MAGIC*. (B) Emission $\geq$ 25 GeV, measured by *MAGIC*. In the lower panels are the multi-wavelength light curves from *AGILE* as appeared in [173].

lower energies. The progressive "growth" of P2 with respect to P1 as the energy increases can be also observed in the *AGILE* multi-wavelength light curves (Figure 3.4). Using these same data, a small excess (3.4σ) could be observed above 60 GeV, consistent with previous observations (ref).

3.5.1 Spectral Constraints from *MAGIC* observations

For the Crab pulsar, in the energy range $E = 0.1 - 5$ GeV, *EGRET* had measured a power-law spectrum of the kind $F(E) \propto E^{\alpha}$ with spectral index $\alpha = 2.022 \pm 0.014$. The flux observed by *MAGIC* at $E = 25$ GeV was several times lower than a straightforward extrapolation of the *EGRET* spectrum. Pulsar emission scenarios predict a generalized exponential shape for the cutoff , that can be described as $F(E) = AE^{-\alpha}\exp[-(E/E_0)^{\beta}]$, where A is a normalized constant, E_0 the cutoff energy and β measures the steepness of the cutoff. For the conventional cases of $\beta = 1$ (exponential cutoff) and $\beta = 2$ (super-exponential cutoff), the data yielded $E_0 = 17.7 \pm 2.8_{stat} \pm 5.0_{syst}$ GeV (where *stat* represents the *statistical* error and *syst* is the systematic error) and $E_0 = 23.2 \pm 2.9_{stat} \pm 6.6_{syst}$ GeV, respectively. Leaving β as a free parameter, the best fit yields $E_0 = 20.4 \pm 3.9_{stat} \pm 7.4_{syst}$ GeV and $\beta = 1.2$.

From a theoretical point of view, the spectral cutoff is explained as a combination of the maximum energies that electrons (e) can reach (because of the balance between acceleration and radiation losses) and the absorption of the emitted gamma-rays in the magnetosphere. Absorption is controlled by two mechanisms: (i) magnetic $e^+ - e^-$ pair production in the extremely strong magnetic field close to the pulsar surface and (ii) photon-photon $e^+ - e^-$ pair production in dense photon fields. If, for a young pulsar like the Crab with a magnetic field $B \sim 10^{12} - 10^{13}$ G, emission occurs close to the neutron star surface (as in classical polar-cap models), then magnetic pair- production attenuation provides a characteristic super-exponential cutoff at relatively low energies; that is, a few GeVs at most (see Section 1.3.1). If, on the other hand, emission occurs farther out in the magnetosphere, at several stellar radii or close to the light cylinder (as in slot-gap and outer-gap models, see Section 1.3) , then absorption mainly arising from photon- photon collisions sets in at higher energies and produces a shallower cutoff (roughly exponential in shape). In either case, however, the measured E_0 could be intrinsic to the emitted spectrum and hence would only provide an upper limit to the absorption strength.

Equation 3.2 from [31] (a largely model-independent relation derived from simulations of gamma-ray absorption by magnetic-pair production in rotating magnetic dipoles) relates the pair-creation cutoff energy, E_{max}, with the location of the emission region r/R_0 (R_0 is the pulsar radius; r is the distance of the emission region from the center of the pulsar) for a pulsar with surface magnetic field B_0 and period P:

$$E_{max} \approx 0.4\sqrt{P\frac{r}{R_0}}\max\{1, \frac{0.1B_{crit}}{B_0}(\frac{r}{R_0)^3}\}\text{GeV} \tag{3.2}$$

The appropriate values for the Crab pulsar are $B_0 = 8 \times 10^{12}$ G, natural constant $B_{crit} = 4.4 \times 10^{13}$ G, and $P = 0.033$ s (where B_{crit} is the critical field that marks the onset of quantum effects in a magnetized plasma, see also Chapter 5). Using for E_{max} the super-exponential cutoff energy $E_0 = 23.2 \pm 2.9_{stat} \pm 6.6_{syst}$ GeV, derived above for $\beta = 2$ as appropriate for the polar-cap scenario, one obtains $r/R_0 > 6.2 \pm 0.2_{stat} \pm 0.4_{syst}$; that is, the emitting region is located well above the pulsar surface. This result, however, contradicts the basic tenet of the polar-cap scenario that particle acceleration and radiation emission occur very close to the pulsar surface. This inconsistency would rule out the polar-cap scenario for the Crab pulsar.

MAGIC results therefore favor an outer-gap or slot-gap scenario for the Crab pulsar. For example, using in Equation 3.2 the value of E_0 that corresponds to $\beta = 1$ (approximately consistent with the outer-gap picture), a high-altitude emitting region is inferred, which is fully consistent with the assumed scenario. Specific recent outer-gap and slot-gap predictions are compared with *MAGIC* data in Figure 3.8. Although the former can provide emission of photons of energies as high as 25 GeV and hence explain the VHE gamma-ray data, the latter cannot. Thus, current outer-gap models seem preferred in explaining *MAGIC* measurement. Lastly, these present measurements reveal a trend of $P2/P1$ increasing with energy: it is < 0.5 at 100 MeV, ≈ 1 at 25 GeV, and > 1 at 60 GeV (Figure 3.7). This trend provides valuable information for theoretical studies that will further constrain the location of the emission region in the Crab pulsars magnetosphere.

3.5.2 New Results from *MAGIC*

The first *MAGIC* observations of the Crab pulsar only comprised data up to February 2008. In winter 2008/09, the Crab pulsar was observed again with *MAGIC* using the sum trigger. In August 2008, *Fermi*-LAT became operational and measured the spectra of gamma-ray pulsars up to a few tens of GeVs [7]. All the

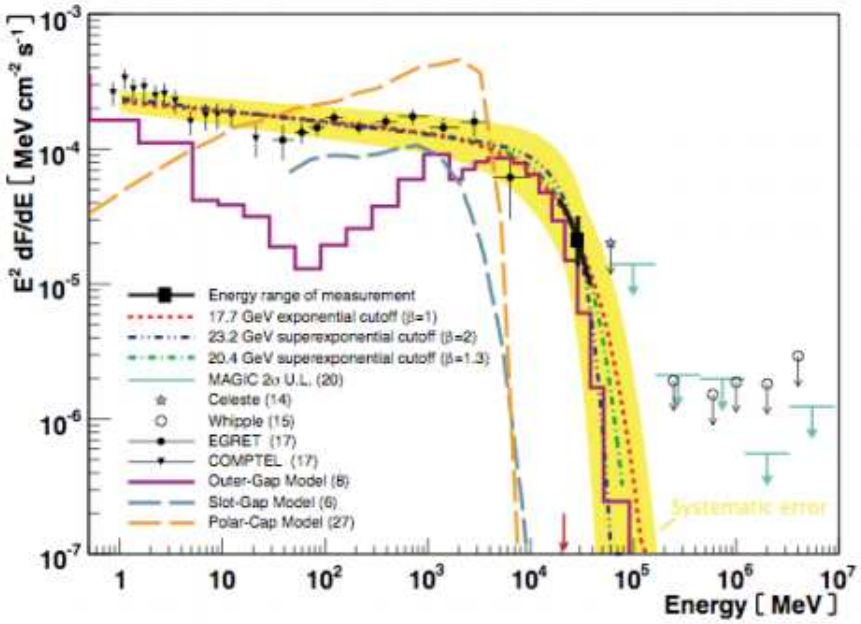

Figure 3.8 Crab pulsar spectral cutoff, from [18]. The black points and triangles on the left represent flux measurements from *EGRET* and *COMPTEL*. The arrows on the right denote upper limits from various previous experiments. A joint fit was performed of a function $[F(E) = AE^{-\alpha}\exp(-(E/E_0)^{\beta})]$ to the *MAGIC*, *EGRET* and *COMPTEL* data. The figure shows all three fitted functions for $\beta = 1$ (red line) and $\beta = 2$ (blue line) and the best fit $\beta = 1.2$ (green line). The black line indicates the energy range, the flux and the statistical error of *MAGIC* measurement. The yellow band illustrates the joint systematic error of all three solutions. The measurement is compared with three current pulsar models, a polar cap model, a slot-gap model and an outer gap model.

energy spectra are consistent with a power law with an exponential cutoff, though statistical uncertainties above 10 GeV are rather large: for some of the pulsars, the phase averaged spectrum deviates from the exponential cutoff but phase-resolved analyses revealed that the spectrum of each small pulse-phase interval is still consistent with the exponential cutoff. The cutoff energies are typically between 1 GeV and 4 GeV. These *Fermi*-LAT measurements also disfavor the polar cap model and support the outer gap and the slot gap models [7].

However, the cutoff energy of the Crab pulsar determined with *Fermi*-LAT under the exponential cutoff assumption is $\sim$ 6 GeV, an unlikely value for the signal above 25 GeV detected by *MAGIC*. In order to verify the exponential cutoff spectrum, a precise comparison of the energy spectra measured by the two instruments is needed. The recent detection of the Crab pulsar above 100 GeV by the *VERITAS* Collaboration [223] has shown that indeed the energy spectrum above the break is not consistent with an exponential cutoff but that it is better described by a broken power law [223]. It is, however, not clear whether the spectrum continues as a power law after the break or there is another component above 100 GeV in addition to the exponential cutoff spectrum because of missing flux measurements in the intermediate energy range from 25 GeV to 100 GeV.

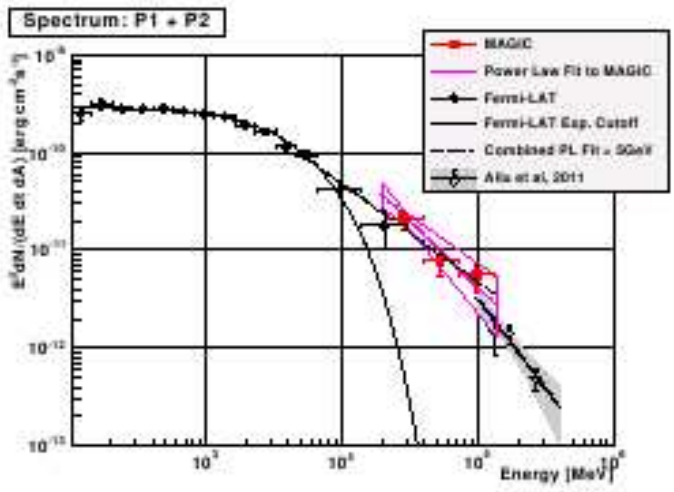

Figure 3.9 Energy spectrum of the Crab pulsar for P1+ P2 from [146]. The black solid line and the dots are obtained from the public *Fermi*-LAT-LAT, while the red points denote the *MAGIC* measurements. The pink line and the butterfly shape indicate the power law fit to the *MAGIC* data and its statistical uncertainty. The gray shade with a black line and open diamonds show the *VERITAS* measurements [223]. The dotted lines show the result of the combined fit above 5 GeV.

The energy spectra of the Crab pulsar were computed based on the detected

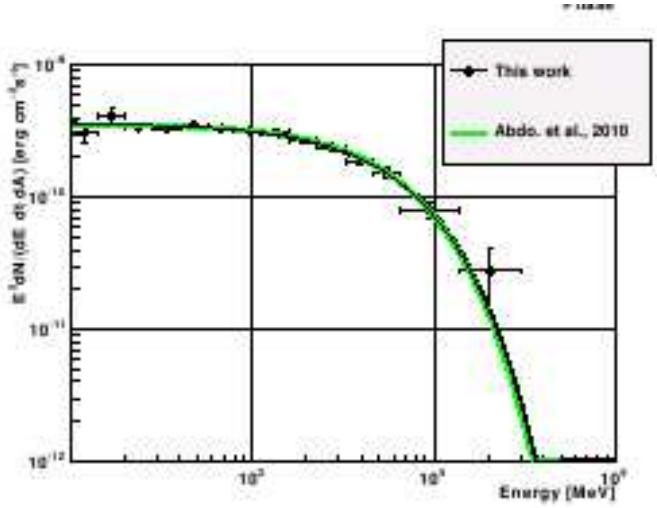

Figure 3.10 Energy spectrum of the Crab pulsar (total pulse) from [146]. The black line and dots are obtained from a likelihood analysis of the public *Fermi*-LATdata, while the green line represents the spectrum reported in [8]

excess events found in P1 and P2, using the standard *MAGIC* software. The combined spectrum of P1 + P2 is consistent with a power law, which can be described using the following formula:

$$\frac{d^3F(E)}{dE\,dA\,dt} = F_{30}(E/30GeV)^{-\Gamma_2} \tag{3.3}$$

where $F_{30} = (14.9 \pm 2.9_{stat} \pm 9.6_{syst}) \times 10^{-9}$ cm^{-2} s^{-1} TeV^{-1} and $\Gamma_2 = 3.4 \pm 0.5_{stat} \pm 0.3_{syst}$ were obtained as best fit parameters. This spectrum would also smoothly connect to the *VERITAS* measurements above 100 GeV. Results are shown in Figure 3.9. Figure 3.9 clearly shows the deviation of the *MAGIC* spectra with respect to the extrapolation of the exponential cutoff spectra determined by *Fermi*-LAT, which is consistent with our statistical analysis.

To get a better estimate of the power law index for the higher energies, *Fermi*-LAT data points above 5 GeV and *MAGIC* data points are combined and fitted by a power law

$$\frac{d^3F(E)}{dE\,dA\,dt} = F_{10}(E/10GeV)^{-\Gamma}. \tag{3.4}$$

The *Fermi*-LAT points were obtained using two methods: the likelihood analysis for each energy interval assuming a power law, and the pulsed counts divided by the exposure which gives the pulsed flux. Even in this case, as Figure 3.10 shows, the exponential cutoff at $E \sim 6$ GeV, suggested by *Fermi*-LAT observations alone, seems to be hardly applicable: best fit parameters being $F_{10} = (3.0 \pm 0.2) \times 10^{-7}$

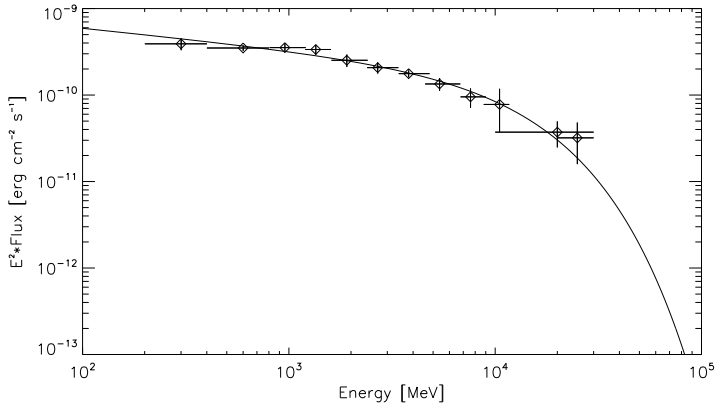

Figure 3.11 Energy spectrum of the Crab pulsar (total pulse). The dots are obtained from a pulsed analysis of the public *Fermi*-LAT data, and the last point represents the *MAGIC* spectral point from [18]

$\mathrm{cm}^{-2}\ \mathrm{s}^{-1}\ \mathrm{TeV}^{-1}$ and $\Gamma = 3.0 \pm 0.1$. The second method, that I applied, was the calculation of the pulsed flux, as explained in Section 2.5. The results are visible in Figure 3.11 and the resulting cutoff obtained was $E_c = 11.74 \pm 2.7$ GeV, still compatible with the *Fermi*-LAT results at 2σ, but more considerate of the *MAGIC* observations.

3.5.3 *MAGIC* Stereo Observations

Most recently, 73 h of stereoscopic data taken with both *MAGIC* telescopes were used to investigate the very high energy (VHE) gamma-ray emission of the Crab pulsar [147]. These Stereo data show a pulsed signal at pulse-shape-independent confidence levels of $6.4 - 8.6\sigma$. Emission is found in the energy range from 50 to 400 GeV and in both the main pulse (P1) and interpulse (P2) phase regions. We provide the widest spectra to date of the VHE components of both peaks, extending down to the energy range of satellite-borne observatories. The improved precision and background rejection of the stereoscopic technique leads to relatively low systematic uncertainties and allows the cross-check of the correctness of each spectral point of the pulsar by comparison with the corresponding (strong and well-known) Crab Nebula flux.

Our findings are in agreement with the detection above 100 GeV recently reported by *VERITAS*, including the P1+P2 flux, photon index, and pulse shape parameters. The spectra of both P1 and P2 are compatible with power laws of photon indices 4.0 ± 0.8 (P1) and 3.42 ± 0.26 (P2), respectively. The difference

in the indices is reflected in the observed P1/P2 ratio of 0.54 ± 0.12. The VHE emission, still under careful investigation and revision of the classical models, can be tentatively understood within a framework where this component is produced by inverse Compton scattering of secondary and tertiary $e^{\pm}$ pairs on IR-UV photons. But this new energy range for pulsar astronomy is still processing its first steps.

3.6 The Other EGRET Pulsars

3.6.1 Geminga

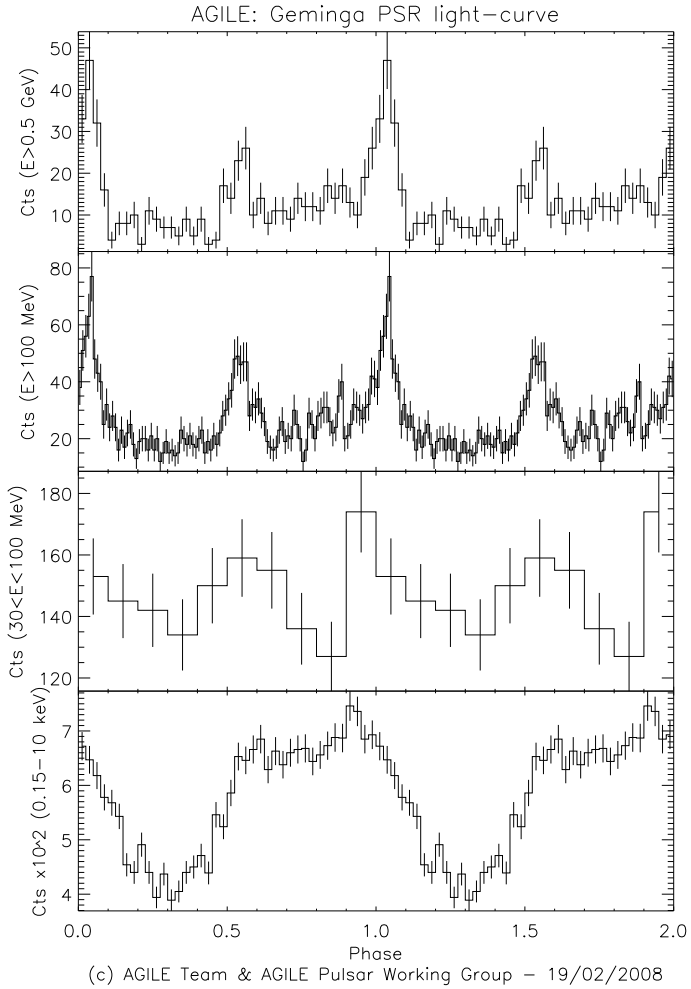

Figure 3.12 Geminga light curves ($P \sim 237.1$ ms) for different energy bands ($E < 100$ MeV, 20 bins, resolution: ~ 11.8 ms; $E > 100$ MeV, 100 bins, resolution: ~ 2.4 ms; $E > 1$ GeV, 20 bins, resolution: ~ 11.8 ms; G class events). The X-ray ephemeris and the 18 keV 40 bins light curve (bottom panel) are obtained by the analysis of *XMM-Newton* data (observation interval 52369 – 54534 MJD).

The Geminga pulsar is the second brightest non-variable GeV gamma-ray

source in the sky and the first representative of a population of radio-quiet gamma-ray pulsars. Since its discovery as a gamma-ray source by SAS-2, more than thirty years ago [75], Geminga has been alternatively considered as a unique object or as the prototype of a population of hidden dead stars. *Fermi*-LAT has now settled this question with the discovery [6] of a substantial population of potentially radio-quiet pulsars, of which Geminga was indeed the first, and for long time the only, example.

Geminga shows an $E > 100$ MeV light curve (Figure 3.12) with properties similar to those of Vela. Apart form the major peaks P1 ($\phi = 0.999 \pm 0.002$, FWHM 0.062 ± 0.008) and P2 (with apex $\phi = 0.507 \pm 0.004$, FWHM 0.08 ± 0.01), secondary peaks are seen trailing P1 and leading P2: the main peak's P2 leading trail ($\phi = 0.8 - 1$) could possibly be associated to unresolved multiple peaks while P1 displays a "bump" at $\phi \sim 0.55 - 0.6$. P1 seems to be characterized by a double structure: a fit with a simple Gaussian yields $\chi^2_r \sim 1.2$, to be compared with a double Gaussian model providing $\chi^2_r < 1$. This feature seems still present even considering different observation blocks separately. The main-peak separation ($\Delta\phi = 0.508 \pm 0.007$ at $E > 100$ MeV) is greater than the value obtained for Vela and it decreases slightly with energy. The 210 keV X-ray light-curve shows a peak (P3) in correspondence with a possible excess in the hard gamma-ray band and a broad top-hat shaped feature partially overlapping in phase with P1.

3.6.2 B1706–44

The *AGILE* light curves of PSR B 1706–44 are shown in Figure 3.13. The broad-band light-curve ($E > 30$ MeV) clearly shows two peaks ($\phi_{P1} = 0.211 \pm 0.007$, $\phi_{P2} = 0.448 \pm 0.005$) bracketing considerable bridge emission (contributing to $> 50\%$ of the pulsed counts) while in the 0.11 GeV range the peaks cannot be discerned from the bridge emission and the pulsar profile presents an unresolved broad ($\Delta\phi = 0.3 - 0.4$) single peak. The same distinction into two peaks was later on adopted also in the *Fermi*-LAT modeling of PSR B 1706–44 light curves [10]. PSR B 1706–44 is a young ($\sim 2 \times 10^4$ yr) and energetic (3.4×10^{36} erg s^{-1}) 102.5 ms pulsar [109] with emission properties similar to Vela [34]. Double peaked PSR B 1706–44 is then in fact Vela-like not only energetically, but also with respect to the offset between the maxima of the high energy and the radio profiles, with neither of the two gamma-ray narrow pulses aligned to the radio peak.

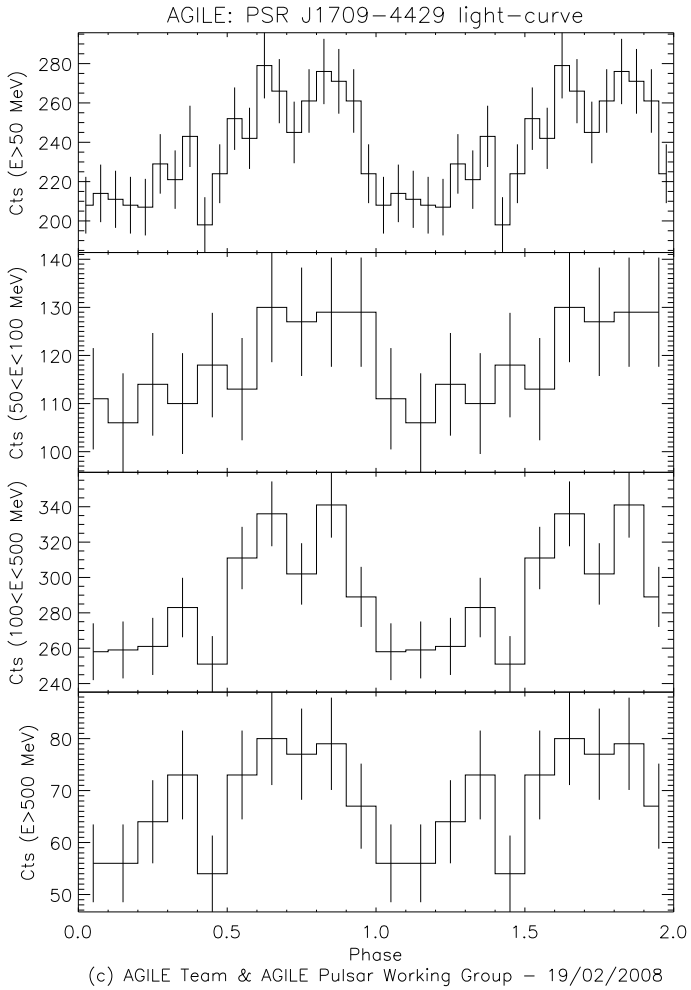

Figure 3.13 PSR B1706–44 light-curves ($P \sim 102.5$ ms) for different energy bands ($E > 30$ MeV, G class events, 40 bins, resolution: ~ 2.6 ms; $0.1 < E < 1$ GeV, G+L class events, 20 bins, resolution: ~ 5.1 ms; $E > 1$ GeV, G+L class events, 10 bins, resolution: ~ 10.2 ms) obtained by integrating all available data. The radio ephemeris and the 1024 bins light curve (bottom panel) are obtained by the analysis of 20 ToAs observed by Parkes radio telescope (observation interval 54220-54562 MJD).

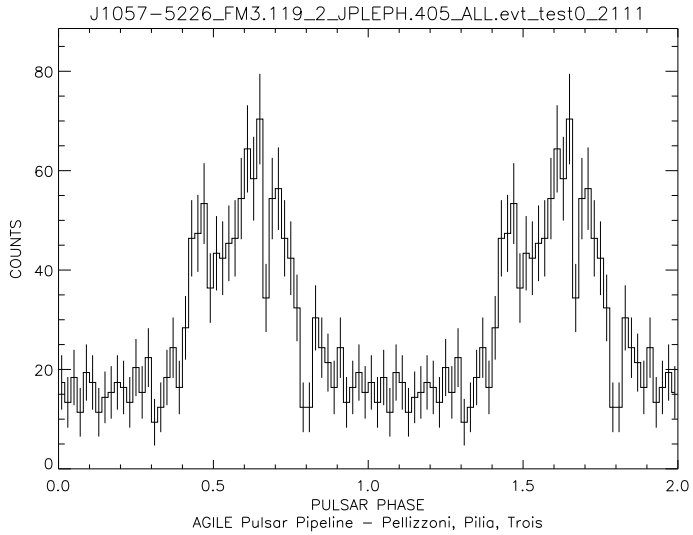

Figure 3.14 PSR B1055-52 light curves ($P \sim 197$ ms) for $E > 100$ MeV, G class events, 50 bins, resolution: ms obtained by integrating all available data until . The radio ephemeris are obtained by the analysis of 51 ToAs observed by Parkes radio telescope (observation interval 54,22055,363 MJD).

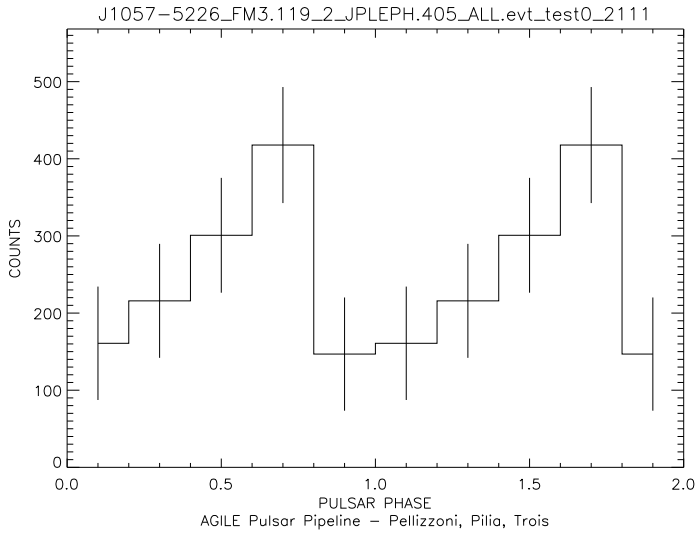

Figure 3.15 PSR B1055-52 light curve ($P \sim 197$ ms) for $E < 100$ MeV, G class events, 50 bins, resolution: ms obtained by integrating all available data until . The radio ephemeris are obtained by the analysis of 51 ToAs observed by Parkes radio telescope (observation interval 54,22055,363 MJD).

3.6.3 PSR B1055–52

PSR B1055–52 is a middle-aged (0.5 Myr) energetic ($\dot{E} = 3 \times 10^{34}$ erg s^{-1}) pulsar which has been detected as a source of pulsed gamma-rays. In their study of energetic pulsars, [230] singled out PSR B1055–52 for comment since it is exceptional in having both an interpulse and wide radio components, with the interpulse (IP) well separated from the main pulse (MP). In general the presence of an IP is a strong clue to a pulsars geometry, and suggests that a study of the radio emission of PSR B1055–52 may give insight into the structure of the magnetosphere and the origin of its gamma-rays.

EGRET revealed that PSR B1055-52 is a pulsed gamma-ray source [217]. Unlike most gamma-ray profiles (but in common with PSR B1706–44), that of PSR B1055–52 does not show two narrow peaks separated by 0.4–0.5 in phase, but has a broad gamma-ray profile with possible sub-peaks at the leading and trailing edge of the profile which peak 0.25 and 0.05 in phase before the radio MP [217]. The leading side of the profile has also been seen with the *COMPTEL* detector (0.7530 MeV), while only the trailing side of the profile is seen above 2 GeV by *EGRET*, suggesting a longitude dependent spectral index. *Fermi*-LAT observations [10] privilege the possibility of a structured profile, with a non-canonical two-peaked structure and notable bridge emission (a strong third peak) between the two, all merged together.

Another feature which makes PSR B1055–52 an interesting source at high energies is its spin-down age of 0.5 Myr, making PSR B1055–52 one of the oldest of the known gamma-ray pulsars (see next Chapter). Its period of 0.197 seconds makes it also the slowest (excluding Geminga). This status as being both an old young pulsar and, at the same time a young old pulsar (most radio pulsars are over 1 Myr old) suggests that it may possess characteristics of both and give insight into the link between high-energy production in the outer magnetosphere and radio emission above the polar cap.

AGILE observations (Figures 3.14 and 3.15) confirm the presence of the broad gamma-ray profile. Just as PSR B1706–44, this pulsar is an outlier in the usual classification of gamma-ray pulsed profiles. A larger gap, compared to the typical sizes for gamma-ray pulsars, could explain this emission and it is indeed expected for very efficient old gamma-ray pulsars [189]. The outer gap model further predicts that two caustics are formed at the edges of the gamma-ray beam, which could account for the sub-structure visible in our data.

3.6.4 PSR B1951+32

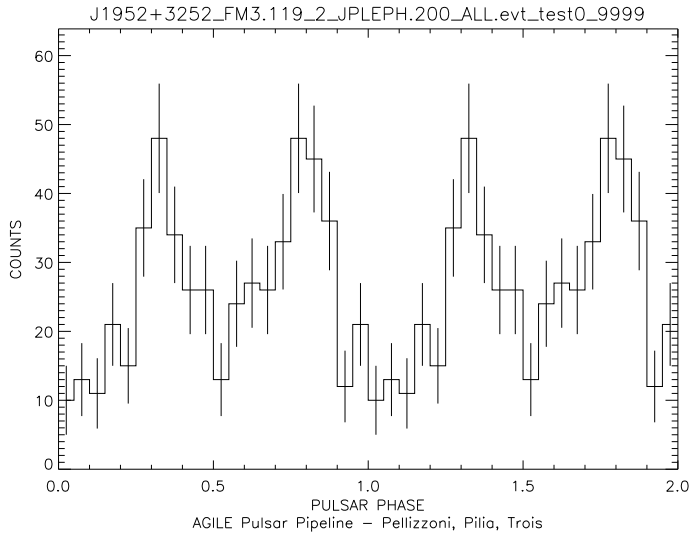

Figure 3.16 PSR B1951+32 light curves ($P \sim 102.5$ ms) for different energy bands ($E > 30$ MeV, G class events, 40 bins, resolution: ~ 2.6 ms; $0.1 < E < 1$ GeV, G+L class events, 20 bins, resolution: ~ 5.1 ms; $E > 1$ GeV, G+L class events, 10 bins, resolution: ~ 10.2 ms) obtained by integrating all available data presented in Table 1. The radio ephemeris and the 1024 bins light curve (bottom panel) are obtained by the analysis of 20 ToAs observed by the Jodrell Bank and Nançay radio telescopes (observation interval 54,22054,562 MJD).

Because of the high timing activity of this pulsar, it was quite difficult to find a new timing solution for this pulsar when starting from a solution with an epoch just before the start of our data span. This pulsar presents frequent glitch activity, that also showed up during *AGILE* observations. The glitches are not so strong that any gamma-ray emission is expected to be detected from them.

The profile observed by *AGILE* is more similar to the *EGRET* one [216] than with *Fermi*-LAT > 100 MeV profile [10]. Given the high noise level of this pulsar, it is possible that the amplitude of the peaks that we observe (see Figure 3.16) is partly due to timing noise and micro-glitches, such as are experienced by the pulsar during the long time span of our observations. It is worth noticing that the multi-wavelength *Fermi*-LAT light curves show a sharpening of the peaks widths from low energies ($100 < E < 300$ MeV) up to $E > 1$ GeV. *AGILE* observations might then be probing regions of the magnetosphere different from those that give the most of the emission at *Fermi*-LAT energies where the beam width is smaller.

3.7 Conclusions

AGILE observations of the known gamma-ray pulsars already produced a step forward in the pulsar studies. *AGILE* new potential relies on the combined pointing strategy plus sky survey observations. To this is added the capability of analyzing very long data spans without incurring into smearing effects, due to the application of the timing noise removal to the gamma-ray analysis. In this way, a very high resolution is obtained but no smearing in the light curves is produced as an effect of the long data span, as every rotation is taken into account by the contemporaneous radio ephemeris.

The gamma-ray light curves appear in all cases more complex than a simple two peaked profile, which led us to the hypothesis that the emission model is not simple, as well. More than one region of the magnetosphere can be responsible for the emission of the different peaks, an indication of which is also the different hardness of the peaks. It is observed, particularly in the Crab pulsar, that the ratio between the two peaks heights is inverted as the energy grows and in fact the second peak is dominant in the VHE band. Models are forced to be revisited, due to the emission above 100 GeV, which seems to exclude the curvature radiation (see Section 3.5), but may come from a different process than the standard gamma-ray emission.

Chapter 4

The First New Pulsars

The results presented in this chapter mainly pertain to three different works. On the first one, [172], at the beginning of the *AGILE* mission, we presented the results of the discovery of new gamma-ray pulsars with *AGILE*, concentrating only on the isolated pulsars and leaving the binary system to subsequent in-depth coverage (Iacolina et al. in prep.). The closer examination of PSR J2229+6114, the brightest new pulsar, is specific to this Thesis and is not present in [172].

The analysis of PSR J2022+3842 using *Fermi*-LAT data was conducted in the framework of our monitoring activity of new possible candidate gamma-ray pulsars and in the context of the campaign in search for new pulsar candidates for the approaching *MAGIC* observations. We published our first findings as an Astronomer's Telegram in Atel 3466 and are now preparing a more diffuse work, also including *AGILE* data, where the emission of this very energetic pulsar is dealt with in more detail.

Finally, now that a statistically relevant sample of gamma-ray pulsars is present, thanks to the observations of *Fermi*-LAT and *AGILE*, and since the modeling of magnetospheric emission models can now make significant advances, we cautioned the future attempts against the problems on which some models incur at a fundamental physics theory level [219].

4.1 Where to Look for New Gamma-Ray Pulsars

Although the bulk of the electromagnetic energy output of spin-powered pulsars is typically expected above 10 MeV, only $\sim 0.5\%$ of the radio pulsar population had clearly been identified in the gamma-ray domain before the advent of *AGILE* and *Fermi*-LAT [216, 173, 86]. Such meager harvest was to be ascribed to the relatively low sensitivity of gamma-ray instruments with respect to radio and X-ray

telescopes. Poor gamma-ray pulsar statistics was a major difficulty in assessing the dominant mechanism which channels pulsar rotational energy into high-energy emission as well as understanding the sites where charged particles are accelerated.

The dominant mechanisms and sites of the emission most probably depend on the rotational period P and magnetic field B of the neutron stars, with the millisecond pulsars (e.g., [92]) behaving differently from the classical, higher magnetic field ones. Population synthesis simulations, featuring comprehensive statistical analysis of diverse models of emission geometry and beaming, yielded very different numbers of radio-loud and radio-quiet pulsars potentially detectable as gamma-ray emitters (see e.g., [82]). However, such simulations were poorly constrained by the source sample available and only a much larger sample of gamma-ray pulsars could help discriminating different emission models.

The large field of view of *AGILE* allowed long uninterrupted observations and simultaneous monitoring of tens of nearby radio pulsars belonging to the gamma-ray pulsar region of the $P - \dot{P}$- diagram characterized by $B > 2 \times 10^{11}$ G and spin-down energy $\dot{E}_{rot} > 1.3 \times 10^{33}$ erg s^{-1} [170]. At variance with the behavior at soft X-ray energies, where the emission is proportional to the rotational energy loss over the squared distance factor ($F_X \propto \dot{E} d^{-2}$, where d is pulsar distance; e.g., [181]), the expected gamma-ray flux of radio pulsars is directly correlated to the Goldreich-Julian current/ open field line voltage [46, 89]. It can be estimated according to the law $F_\gamma \propto \sqrt{\dot{E}} d^{-2}$ [24, 111], which was known to reasonably fit *EGRET* pulsars. The large dispersion of such fit (probably due to different beaming fractions) provides the minimum/maximum normalization values, allowing a worst/best case approach for the gamma-ray flux estimates. Following such an approach, we built a sample of ~ 100 radio-loud pulsars which were likely to be above the *AGILE* sensitivity threshold ($F_{min} > 2 \times 10^{-8}$ ph cm^{-2} s^{-1} at $E > 100$ MeV). The actual number of detections will of course still depend upon the emission model geometry and efficiency.

4.2 The Initial Sample

Top-ranking targets with poor *AGILE* exposure, well-known pulsars already deeply investigated at the epoch of *EGRET* observations, and sources reserved to the *AGILE* Guest Observer Program were excluded from our list which encompasses 35 gamma-ray pulsar candidates. In ranking order: J0737–3039*, J1833–1034, J1744–1134, J1740+1000, J1747–2958, J2043+2740, J1730–2304,

J1513–5908, J1524–5625, J1909–3744*, J1357–6429, J1531–5610, J1809–1917, J1617–5055, J1803–2137, J1801–2451, J0940–5428, J1549–4848, J1718–3825, J1824–2452, J1730–3350, J0900–3144*, J1420–6048, J1739–3023, J1751–2857*, J1804–2717*, J2229+6114, J1105–6107, J1721–2457, J1124–5916, J1722–3712, J1740–3015, J1823–3106, J1745–3040, J1016–5857 (the asterisk indicates binary systems). See http://agile.asdc.asi.it for details about *AGILE* Data Policy and *AGILE* Team Targets List. A new wealth of candidate gamma-ray pulsars are awaiting a more detailed analysis and will be collectively published into the *AGILE* Catalog of Gamma-Ray Pulsars.

Here only published results about isolated pulsars are presented. Since gamma-ray pulsar detection must start from an at least approximate knowledge of recent pulsar ephemeris (see Section 2.5.1), a dedicated pulsar radio monitoring campaign was undertaken on all these targets. Conservatively, we present here timing analysis results and detection claims only for pulsars having simultaneous radio ephemeris for the whole relevant *AGILE* observing epochs. Our campaign continues throughout the *AGILE* mission for most of the targets (accordingly to their visibility), using two telescopes (Jodrell Bank and Nançay) of the European Pulsar Timing Array (EPTA), as well as the Parkes radio telescope of The Australia Telescope National Facility (ATNF).

Pulsar data were collected since the early phases of the mission. Timing observations suitable for pulsed signal analysis started in 2007 July (at orbit 1146) after engineering tests on the payload. Here observations are reported of data collected up to 2008 June 30.

4.3 New Gamma-Ray Pulsars

4.3.1 PSR J2021+3651

The first new pulsar of the post-*EGRET* era has been detected in the framework of the *AGILE* Guest Observer Program. PSR J2021+3651 [87] was discovered after the end of the *CGRO* mission as a radio pulsar and it was long considered a likely counterpart of the high-energy gamma-ray source 2CG 075+00 = 3EG J2021+3716 = GeV J2020+3658, but it could not be confirmed due to the lack of a contemporaneous radio pulsar ephemeris to fold the sparse, archival gamma-ray photons from *EGRET*. Gamma-ray pulsations from PSR J2021+3651 was detected in the 100–1500 MeV range using data from the *AGILE* satellite gathered over 8

months, folded on a densely sampled, contemporaneous radio ephemeris obtained for this purpose at the Green Bank Telescope (GBT).

Pulse-phase-resolved images showed that there was only one dominant source, AGL J2020.5+3653 = PSR J2021+3651, in the region previously containing confused sources 3EG J2021+3716 and 3EG J2016+3657. The single radio pulse leads the first gamma-ray peak by 0.165 ± 0.010 cycles. The gamma-ray pulse consists of two sharp peaks separated by 0.47 ± 0.01 cycles. Its pulse shape is similar to other gamma-ray pulsars, with two sharp peaks separated by slightly less than 0.5 cycles. This morphology, as well as the lag between the radio and first gamma-ray peak, are in accord with simulations of outer-gap accelerators viewed at large angles from the pulsar rotation axis, which may help to explain its high gamma-ray efficiency, with respect to pulsars with similar $\dot{E}$: $\eta_\gamma = F d^2/\dot{E} \approx 0.18 d_{12}^2$, where F is the flux in the 100 MeV - 10 GeV range and d_{12} is the distance in units of 12 kpc, as calculated from the electron-density model by [52].

4.3.2 *AGILE* Team Observations and Results

Table 4.1 lists the emission parameters of the seven pulsars that were first presented as new gamma-ray detections by *AGILE*. The resulting radio-aligned light curves are plotted in Figure 4.1 where for each pulsar the actual bin size and energy range have been adjusted according to the available statistics and light curve structure. We note that in all cases radio and gamma-ray timing results are compatible, with the highest significance frequency detected in gamma rays within the errors of the radio ephemeris value, considering also the period search resolution. Examples of the exploration of much larger frequency search grids are shown in Figures 4.2 and 4.4, respectively for PSR J2229+6114, for which the best gamma signal is within 1σ from the radio peak, and for PSR J1824–2452, for which the radio-gamma frequency discrepancy is comparable with the gamma-ray period search resolution.

Both χ^2 statistics and Z_n^2/H-test provide comparable detection significances, except for PSR J2229+6114. The Z_n^2 test applied to this pulsar provides slightly better results than the other statistics ($Z_1^2 = 39.5, Z_2^2 = 45.9$ corresponding to a $\sim 6\sigma$ detection). Furthermore, we verified that our analysis procedure (potentially affected by instrument-related systematic errors and biases in events extraction criteria) does not produce fake detections at a significance level above 3σ when the radio-ephemeris are applied to randomly extracted *AGILE* data.

Four targets were also firmly detected by the likelihood spatial analysis. It

Table 4.1. Emission parameters of the seven pulsars discussed in text for which timing analysis yielded a $>4\sigma$ detection. Four targets (upper part of the table) are firmly detected also in spatial analysis.

PSR Name	G.Lon. deg	G.Lat. deg	P ms	τ[a] yr	D[a] kpc	$\log \dot{E}$ erg s^{-1}	$\chi^2_{red}(N_{st})$[b]	σ_{time}[c]	σ_{space}[d]	F_γ[d]	$\log L_\gamma$[e] erg s^{-1}	$L_\gamma/\dot{E}$
J2229+6114	106.65	2.95	51.6	1.0×10^4	12.0	37.35	6.0(36)	5.0	7.5	26±4	35.36	0.01
J1513–5908	320.32	-1.16	150.7	1.6×10^3	5.8	37.25	4.2(3)	4.0	6.4	34±6[f]	35.04	0.006
J1016–5857	284.08	-1.88	107.4	2.1×10^4	9.3	36.41	6.0(69)	4.8	12.3	62±6[f]	35.71	0.2
J1824–2452	7.80	-5.58	3.0	3.0×10^7	4.9	36.35	4.2(1)	4.2	3.6	18±5	34.62	0.02
J1357–6429	309.92	-2.51	166.1	7.3×10^3	4.1	36.49	5.2(7)	4.7	1.8	<14	<34.35	<0.007
J2043+2740	70.61	-9.15	96.1	1.2×10^6	1.1	34.75	4.1(1)	4.2	0.6	<6	<32.84	<0.01
J1524–5625	323.00	0.35	78.2	3.2×10^4	3.8	36.51	4.6(4)	4.3	1.0	<16	<34.34	<0.007

[a]Pulsar distance and characteristic age obtained from ATNF Pulsar Catalog (http://www.atnf.csiro.au/research/pulsar/psrcat/; [148]).

[b]Pearson's χ^2 statistics applied to the 10-bin, $E > 50$ MeV folded pulse profiles (N_{st} is the number of steps over period search grid).

[c]Pulsed emission detection significance (weighted accounting for N_{st}).

[d]Likelihood analysis detection significance and flux (or 2σ upper limit) in units of 10^{-8} ph cm^{-2} s^{-1} ($E > 100$ MeV).

[e]$E > 100$ MeV luminosity assuming 1 sr beam emission and photon index 2.0 (for J2229+6114 the measured photon index of 2.2 has been used).

[f]Possibly multiple sources. Source confusion may affect flux and significance.

is not surprising that spatial detection be missing for weaker targets at the initial *AGILE* exposure level. In high-background regions of the Galactic plane, our pulsed emission search sensitivity can be better than our spatial analysis sensitivity. Furthermore, timing analysis can be applied to the full *AGILE* event list (i.e., G+L event classes extending up to 60° from the center of the field of view), while, at first, spatial analysis was only fully calibrated for the G class events detected within 40° from the center of the field of view. However, some of the non-detections in spatial analysis are, indeed, puzzling. According to Figure 4.1, PSR J2043+2740 has a pulsed flux and light curve very similar to PSR J1513–5908 (note that both are based on G+L events). Moreover, J2043+2740 is out of the Galactic plane, in a region well exposed and with low diffuse emission. Thus, it should have been detected by the image analysis more easily than J1513–5908, which sits in a higher background region, unless, of course, they have very different spectra.

4.3.3 General Characteristics of the New Pulsars

Pulsars in Table 4.1 are ranked according to their overall detection significance. Pulsars firmly detected both through timing and spatial analyses are placed above the line. Pulsars detected through timing analysis alone await longer simultaneous gamma-ray and radio observations for confirmation and reliable luminosity estimation. In Table 4.1, the most significant detection is PSR J2229+6114, which is discussed in more detail in the following Section. PSR J1513–5908 (B1509–58) was detected by *COMPTEL* in the 1–10 MeV range, while *EGRET* reported [76] only marginal evidence for a weak $< 4\sigma$ source at $\sim 1^\circ$ from the radio position, with a pulsed emission upper limit of $< 58 \times 10^{-8}$ ph cm^{-2} s^{-1}. A more complete analysis of this pulsar is presented in the next Chapter. PSR B1821–24 was the first millisecond pulsar to be clearly identified at gamma-ray energies, after the tentative 3.5σ detection of PSR J0218+4232 with *EGRET*[97], now confirmed by *Fermi*-LAT observations [7]; it is discussed in Section 4.5.

PSR J1016–5857 stands out in Table 4.1 for its very high efficiency in converting rotational energy loss into high-energy gamma rays. This may be ascribed to distance uncertainties, as happened to be the case for the previously discovered PSR J2021+3651 [87] for which the distance derived from the dispersion measure is certainly overestimated. Furthermore, we note that the position ($l = 284^\circ.47$, $b = -0^\circ.94$) and flux of the *AGILE* gamma-ray source is only marginally compatible with 3EG 1013–5915, from the unidentified sources of the Third

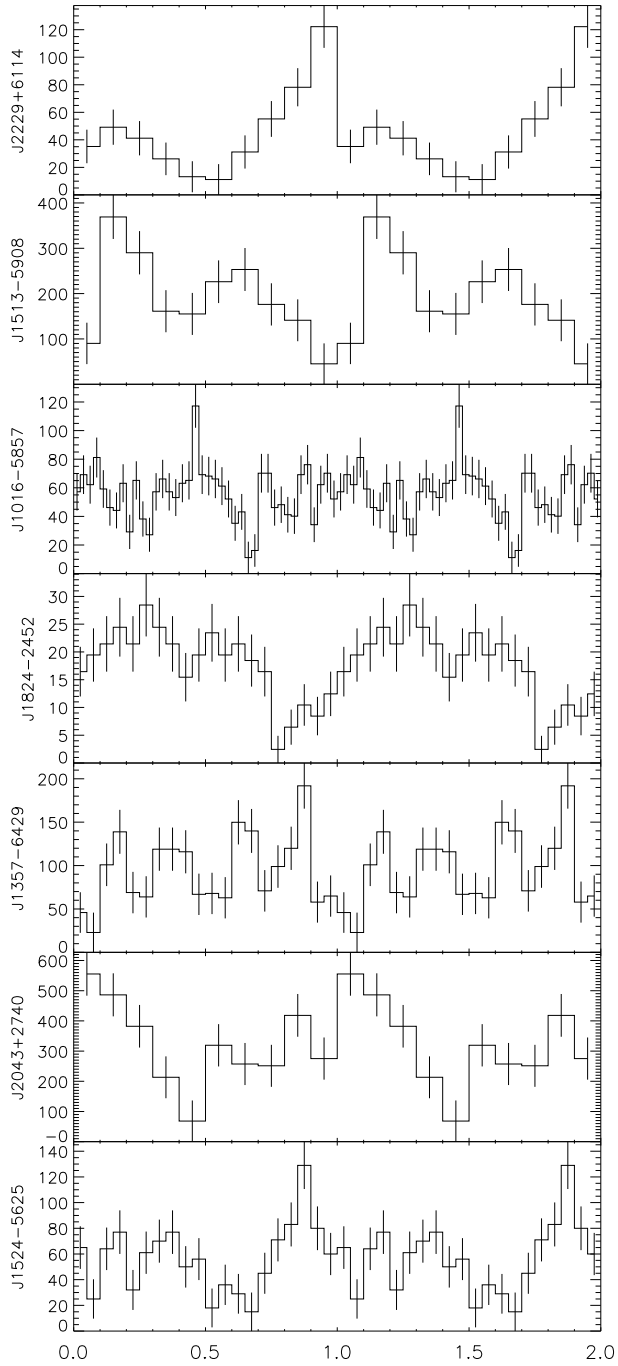

Figure 4.1 Background-subtracted $E > 100$ MeV folded pulse profiles (except for the $E > 50$ MeV J1357–6429 light curve) of the pulsars shown in Table 4.1. Events extraction radius is optimized as a function of energy (see the text). All pulse profiles are obtained using G event class only except for PSR J1513+5908 and PSR J2043+2740 that have higher counts statistics because detections are obtained including G+L event class. For PSR J2229+6114 the histogram of the ~ 75 (G+L) events with $E > 1$ GeV is also shown. Absolute timing is performed for each target: the main radio peak (1.4 GHz) corresponds to phase 0. Possible fluctuations of the dispersion measure over the considered time interval are not expected to significantly affect phasing results, given the time resolution of the available gamma-ray light curves.

EGRET Catalog, for which multiple associations were proposed [94]. The region, originally covered by the gamma-ray source 2CG 284–00, discovered by *COS-B* [206], is very complex. Other nearby sources, and in particular pulsar PSR J1016–5819 (not belonging to our sample), could significantly contribute to the high flux observed by *AGILE* in this region.

Of the remaining three pulsars, detected only through timing analysis, the most notable is certainly PSR J2043+2740 which, with an age in excess of one million years, would be the oldest ordinary (non-recycled) pulsar seen in the gamma-ray domain. The precise measurements of its flux will yield its luminosity and thus its efficiency, a parameter of paramount importance for the understanding of gamma-ray emission as a function of the pulsar age. All pulsars from Table 4.1 have, at different times, been confirmed as gamma-ray emitters by subsequent *Fermi*-LAT observations [7] but PSR B1821–24 which was only detected by *AGILE* in a restricted interval of time (Section 4.5). PSR J2229+6114 was among the first to be discovered by *Fermi*-LAT, while it took a longer time to observe the soft PSR B1509–58 (see Chapter 5) and also PSR J2043+2740.

4.4 PSR J2229+6114

PSR J2229+6114 was discovered as a radio pulsar in 2001 [85]. A gamma ray source positionally coincident with PSR J2229+6114 ($(l,b) = (106.^\circ 6, 2.^\circ 9)$) was possibly detected by *COS-B* [232]. Later, the *CGRO* mission observed gamma-ray emission from this source with both *COMPTEL* [107] and *EGRET* [94]. *EGRET*'s unidentified source 3EG J2227+6122 has been hypothesized to be a pulsar since the beginning by many authors (e.g. Halpern & Ruderman 1993; Kaaret & Cottam 1996; Yadigaroglu & Romani 1997). In 2001 Halpern et al. first presented an X-ray, optical and radio study of the error box of the *EGRET* source proposing that only one plausible candidate was to be associated with 3EG J2227+6122: a highly polarized, flat spectrum, radio shell superposed on a compact non-thermal X-ray source. Its most likely interpretation, a young pulsar with an associated wind nebula, was confirmed by subsequent follow-up observations. *AGILE* was able to firmly identify PSR J2229+6114 with 3EG J2227+6122.

PSR J2229+6114 has $P = 51.6$ ms and $\dot{P} = 7.8 \cdot 10^{-14}$ s s^{-1}, which imply, in the standard dipole assumption, estimated spin-down power $\dot{E} = 2.2 \cdot 10^{37}$ erg s^{-1}, magnetic field $B = 2.0 \cdot 10^{12}$ G and characteristic age $\tau = 10^4$ yr. PSR J2229+6114's position in the Cygnus region made it one of the most observed targets during AO

1, and allowed an intense monitoring during the AO 2 phase which concentrated on the Cygnus region. A specific optimization on the events' extraction parameters is performed in order to maximize the signal to noise ratio for the pulsed signal (see also Section 2.5). The optimal event extraction radius varies as a function of the photon energy (and thus it is related to the pulsar spectrum) according to the PSF and the background level of *AGILE*. For PSR J2229+6114 the extraction radius used to optimize the signal to noise ratio is $\sim 2^{\circ}$, which is well below *AGILE*'s PSF for $E > 50$ MeV ($\sim 5^{\circ}$).

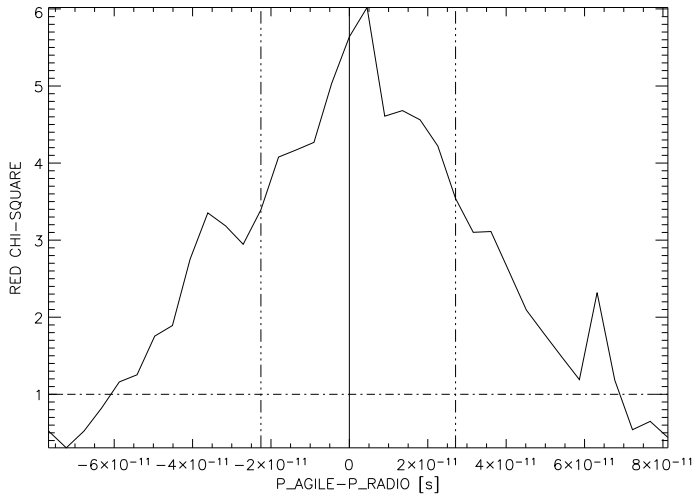

Figure 4.2 PSR J2229+6114: gamma-ray period search result (period trials vs. χ^2 Pearson statistics). The radio period (vertical line at $P_{AGILE} - P_{RADIO} = 0$) is 51.64101208(3) ms (PEPOCH = 54575.5856 MJD). The most significant gamma-ray pulse profile is obtained for $P_{AGILE}^{Best} = 51.641012085(2)$, a value within the 1σ error on the radio period (vertical dashed lines).

For PSR J2229+6114 *AGILE* detected pulsed emission (radio/gamma-ray periods discrepancy $\leq 10^{-11}$ s, Figure 4.2) The gamma-ray light curve of this pulsar (detected up to over 1 GeV), featuring just one prominent peak shifted $\sim 180^{\circ}$ in phase from the radio main peak, is shown in Figure 4.1 and in more detail in Figure 4.3. It is worth noting that assuming a distance of ~ 3 kpc inferred by X-ray observations [85] and isotropic emission, the pulsar gamma-ray efficiency would be ~ 0.5, a factor of 20 higher than that quoted in Table 4.1. In modern pulsar beaming models (in particular high-altitude models) the assumption of isotropy in luminosity calculation could be a better approximation in most cases (see Section 4.7), implying that efficiencies should be increased by roughly an order of magnitude from those based on the commonly assumed 1 sr beam [227].

Anyway, precise efficiency measurements await for a better assessment of pulsar distance, flux, and beam geometry.

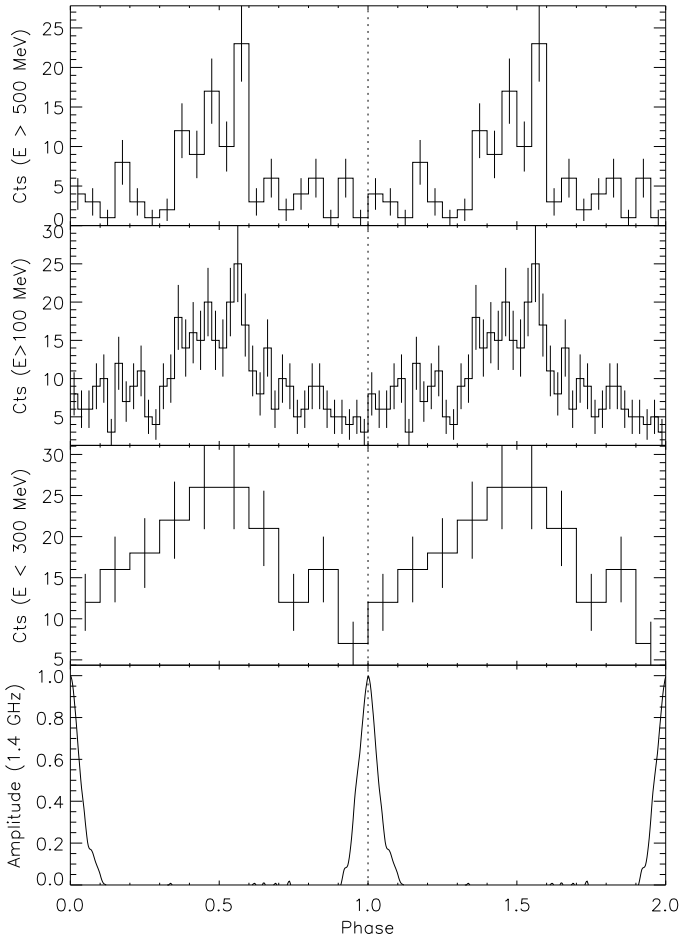

Figure 4.3 PSR J2229+6114 light curves ($P \sim 51.6$ ms) for different energy bands ; G+L class events obtained by integrating all available data up to june 2009. The radio ephemeris and the radio light curve (bottom panel) are obtained by the analysis of ~ 4100 ToAs observed at Jodrell Bank in the UK (radio observation interval $54270-54981$ MJD).

In Figure 4.3 are shown the multi-wavelength light curves for PSR J2229+6114, in phase with the radio peak which is assumed to be at phase 0. The reduced χ^2 value according to the Pearson's statistics for the phase histogram relative to the overall emission above 100 MeV is 4.35, corresponding to a weighed significance of the detection of $> 8\sigma$. The Z and H tests respectively give a detection significance of $> 8\sigma$ and 5.5σ so that the chance of a fake detection, of non-pulsed emission results 4×10^{-8}, ruling out the null hypothesis. Peculiarly, this pulsar appears to have only one emission peak, which is in anti-phase relative to the radio peak. A single peak in the gamma-ray

profile of a pulsar is not usual, but it can be explained in the framework of all the emission models, as a function of the viewing geometry.

4.5 PSR J1824–2452 (B1821–24)

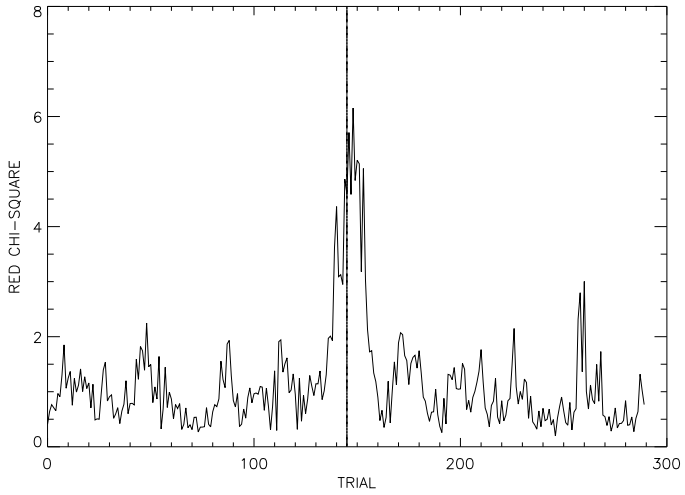

Figure 4.4 PSR J1824–2452: gamma-ray period search result. The radio period is 3.0543151208713(1) ms (PEPOCH = 51468 MJD). The most significant gamma-ray pulse profile is obtained for $P^{Best}_{AGILE} = 3.05431511(1)$ ms. The corresponding radio-gamma periods discrepancy $\lesssim 10^{-11}$ s is comparable to the period search resolution in the considered data span (54339-54344 MJD).

At variance with all the other targets, the millisecond pulsar J1824–2452 in the Globular Cluster M28 was detected by *AGILE*, with good significance (greater than 4σ) and perfect radio-gamma periods match, only in the time interval 54339–54344 MJD (Figure 4.4). The main radio peak at 1.4 GHz is coincident with the broad single peak seen in gamma rays. Only marginal detection was obtained integrating other observations with comparable exposure or the whole data span. Noise fluctuations could possibly explain the apparent variability.

Alternatively, although its gamma-ray efficiency and high stability of spin parameters are compatible with rotation-powered emission, some additional mechanism disturbing the neutron star magnetosphere in the dense cluster environment could be invoked to explain the variable gamma-ray phenomenology of this peculiar pulsar. *AGILE* timing failures at sub-millisecond level in some observations (mimicking source variability) cannot be excluded. However, this seems unlikely, since we verified both timing accuracy and stability at ~ 200 μs

level with Vela pulsar observations. Confirmation of this tantalizing result about physical variability will rest on longer monitoring campaigns. An encouraging finding in this direction is the detection of gamma-ray emission coming from the globular cluster M28, to which J1824–2452 belongs, in the spatial analysis of *Fermi*-LAT data [9]. While no pulsation is found, a diffuse gamma-ray emission is observed in this and in other globular clusters, reasonably assumed, also based on its spectral properties, to come from an unresolved population of pulsars.

4.5.1 Variability in Pulsars

While it is not typical of millisecond pulsars (see Section 1.1.4) to show timing noise, PSR J1824–2452 is an exception, where timing noise has been observed, of smaller amplitude than what is typically found in young pulsars, and even a small glitch [48]. However, no direct connection can be drawn between these expressions of radio impulse variability and the fact that the emission in the gamma-rays appears variable.

With *AGILE*, we addressed from the gamma-ray point of view, most of the variability aspects of pulsars, such as timing noise (see Section 2.5.3), glitches (see Section 3.3.1) and finally, variable emission of pulsed gamma-rays (see Section 4.5). Up to now only one episode of ”temporary” gamma-ray pulsar has been observed, also because it is hard to find this kind of emission using a long data span as it is typically necessary to detect significant gamma-ray emission. A careful KS (see Section 3.2) investigation of all our candidates will be performed in the context of the *AGILE* Pulsar Catalog, where light curve variability on different time scales or nulling emission could be analyzed.

In general, it is not clear that there should be a direct link between phenomena happening at the extremes of the electromagnetic spectrum. As highlighted in Section 4.7, the radio emission does not carry away a significant fraction of the rotational energy and it is, therefore, subject to different constraints than the gamma-ray emission. It seems that the timing noise, while influencing the gamma-ray timing, as well as the radio timing, does not show any specific feature in the gamma-rays. Glitches, on the other hand, could be observed in gamma-rays as a very fast and temporary enhancement on the gamma-ray flux (Section 3.3.1), but more observations are needed to support this theory.

We have also investigated the possibility of gamma-ray emission from Giant Pulses (GPs). GPs are relatively rare episodes of intense radio outbursts that are

clearly a special form of pulsar radio emission (e.g. [130, 145]). They are of short duration: from several microseconds down to few nanoseconds, typically limited to a part of the profile. Their peak flux densities can exceed thousands (and, in the case of the Crab pulsar, nearly a million) of times the peak flux density of regular pulses (the Crab pulsar was actually discovered by observations of its GPs [203]). GPs are only observed in 11 pulsars and, in fact, they do not seem to strongly correlate with any particular pulsar property or parameters. They do not seem to dissipate rotational energy and no correlation has been observed up to now with the emission in the optical or X-rays. No information was present about the possibility of gamma-ray emission.

As the Crab pulsar is one of the pulsars that show the GP phenomenon, we investigated the connection between the presence of the small and not constant third peak in its gamma-ray light curve (see Section 3.4) and the phase at which typically GPs are observed in the radio profile of the Crab. It is hard to define a similar connection unless a specific simultaneous monitoring is done that permits to tag the GPs and fold the gamma-ray emission in correspondence to these events. Such a monitoring program is ongoing for *AGILE* in collaboration with the Medicina radio telescope in Italy, but a lot of simultaneous data need to be collected to obtain enough statistics in the gamma-rays. A similar program has been promoted for the *MAGIC* telescope using radio observations from the Effelsberg telescope in Germany. Even in this case, the observations are still in progress.

4.6 Going Further, New Pulsars

The new *AGILE* and *Fermi*-LAT discoveries have brought up the number of known gamma-ray pulsars of one order of magnitude. Despite the fact that a big enough sample as that of radio pulsars is still far from reach, yet 100 pulsars consent to say something statistically relevant in order to constrain the models of gamma-ray emission. Taking advantage of the simultaneous presence of two satellites for gamma-ray astronomy at present times, our purpose is to be alert whenever new candidates are discovered at other wavelengths and search for them in gamma-rays. The latest pulsar discovered in X-rays and radio that seemed a good candidate for gamma-ray emission, was thus immediately analyzed [178] and also proposed for *MAGIC* observations.

4.6.1 PSR J2022+3842

PSR J2022+3842 is a 24 ms radio and X-ray pulsar in the supernova remnant G76.9+1.0, most recently discovered by [26] in observations performed with the *Chandra* X-ray telescope, the GBT, and the *Rossi X-ray Timing Explorer* (*RXTE*). The pulsar spin-down rate implies a rotation-powered luminosity $\dot{E} = 1.2 \times 10^{38}$ erg s^{-1}, a surface dipole magnetic field strength $B_s = 1.0 \times 10^{12}$ G, and a characteristic age of 8.9 kyr. PSR J2022+3842 is thus the second-most energetic Galactic pulsar known, after the Crab, as well as the most rapidly-rotating young, radio-bright pulsar known.

Motivated by the *Chandra* discovery of the point source and possible PWN at the heart of SNR G76.9+1.0, [26] searched for radio pulsations with the GBT. A candidate 24 ms periodicity was detected on two days with formal significances of 7σ on MJD 54397 and 12σ on MJD 54400. Confirmation observations were carried out on 2009 May 6 (MJD 54957). The difference in the pulse periods derived at these epochs gave the first indication of the pulsar spin-down rate and thence its canonical age, magnetic field strength, and spin-down power.

Additional radio observations were carried out at roughly 3-month intervals to constrain the pulsar long-term timing behavior. Notably, the pulse periods measured during and after the confirmation observation differed substantially from those detected during the two discovery observations made 1.5 years earlier, implying that a spin glitch of magnitude $\Delta P/P \simeq 1.9 \times 10^{-6}$ had occurred at an unknown epoch in this interval. The spacing of the radio timing observations together with apparent timing noise instability in the pulsar rotation on similar timescales precluded derivation of a phase-connected timing solution. The long-term average spin-down rate was determined through a least-squares fit to the multi-epoch period measurements as $4.3192(27) \times 10^{-14}$. This result was consistent with the short-term X-ray ephemeris derived from an *RXTE* observation for a total of 99 ks over the 8-day span 2010 January 27 - February 4 UT: $43064(93) \times 10^{-14}$.

We looked for pulsation for this new, very energetic gamma-ray pulsar candidate in the public *Fermi*-LAT data. No pulsation was found using the radio ephemeris valid on a 512 days time interval (MJD 54957 - 55469), corresponding to the validity of the radio ephemeris. This can be explained by the fact that the pulsar timing behavior is irregular during the radio observations, with glitch like activity, scattering and timing noise which cannot be accounted for by sparse long time ephemeris [26].

We thus also tried to fold a smaller interval of *Fermi*-LAT observations, around the time of the X-ray observations, which provided a solution that can be more accurate to describe the timing parameters in a short interval of time close to their validity interval. With this analysis, we reported a tentative detection of pulsed gamma-ray emission [178]. The gamma-ray emission was observed in *Fermi*-LATdata using the X-ray ephemeris provided by *RXTE* in the 8-days time interval (MJD 55223 - MJD 55231). Gamma-ray observations were folded in the interval MJD 55213 - MJD 55241. 5σ emission was detected at $E > 100$ MeV with a total of 660 ± 130 pulsed counts (event extraction radius ROI=2°) at frequency $\nu = 41.1730092(4)$ Hz, and frequency derivative $\dot{\nu} = -7.30(4) \times 10^{-11}$, referred to epoch MJD 55227, within the RXTE ephemeris error. The corresponding pulsed flux above 100 MeV is $2.7(5) \times 10^{-7}$ ph cm^{-2} s^{-1} and the luminosity is $3.6(6) \times 10^{35}$ erg s^{-1} ($= 0.03 \times \dot{E}_{rot}$) assuming a distance $d = 10$ kpc and a beaming factor $f = 1$ corresponding to 4π sr emission. Extending the interval, the significance of the detection decreases, as expected due to the fact that the ephemeris in such a noisy pulsar can only account for the timing behavior in a restricted time interval.

While a stronger detection, in a longer time span, is expected with a more complete radio coverage, this pulsar seems to present a hard spectrum, representing also a promising candidate for VHE observations.

4.7 Constraints to the Models

Since the seminal paper of [205], the emission mechanism of pulsars is associated to spark gaps, regions where the parallel component of the electric field is so large that pair production may be copious.

A key issue treated frequently in the literature is the location of the gaps, with two favored classes of models: a gap close to the star surface (*polar cap gap*, see Section 1.3.1), a gap in the vicinity of the speed of light radius $r_c = c/\omega$ (*outer gap*, see Section 1.3.3). The advantage of the former possibility is that close to the neutron star the magnetic and electric fields are expected to be orders of magnitude larger than at r_c. On the other hand, as shown originally by [50] and by [105], photon release at the polar cap does not preserve the energy and angular momentum budget. This strongly favors models with the gap located at r_c (e.g. [47], [189]). However the double (or more complex) structure of pulsar pulses has generated new interest for models where both gaps are active (see e.g. [173, 172]). This is

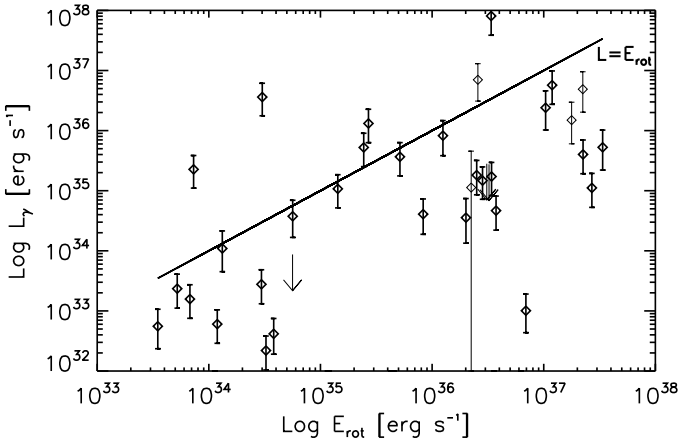

Figure 4.5 Distribution of the gamma-ray luminosity of the gamma-ray pulsars observed by *AGILE* and *Fermi*-LAT as a function of the spin down energy loss. The line indicates the condition of efficiency=1 for the conversion of the spin down energy into gamma-ray luminosity. The fact that the efficiency can be larger than 1 is also discussed in [7] and it is due to the fact that a beaming fraction of 4π sr is considered. However, new pulsar modeling (see e.g. [227]) predicts a very large beaming fraction for the gamma-ray pulsars.

consistent with the observation that the various pulse components in general have different spectral shape ([2], [177]).

All previous considerations are essentially of little relevance for radio pulsars, since the fraction of the neutron star rotational energy released in the radio band is extremely small. The problem of the location of the emission regions becomes of renewed interest after the observation with the *AGILE* and *Fermi* satellites of tens of pulsars in the gamma-ray band (see [173, 172], [7]), since in this band one observes a sizeable fraction of the spin-down energy (10-100 %, [7], see Figure 4.5). Most of the models for the gamma-ray emission indeed exclude the polar cap location, on the basis of considerations of gamma-ray absorption (see e.g. [18] and Section 4.7). Still in some cases a polar cap model is proposed (e.g. [173], [229], [177]), and in general the region of overall emission is located at $r < r_c$ (e.g. slot gap models: [69], [164], annular gap models: [67]). On the other hand, the wind models (see e.g. [119]) and new force-free models of the magnetosphere (see [30]) propose that the emission should come from the external magnetosphere, beyond the r_c. From their simulations, [30] propose that the high-energy radiation should come from a current sheet outside the light cylinder, asymptotically approaching the split monopole solution outlined by [38]. Geometrically, based on the light curve modeling, the current sheet inside the light cylinder would not seem to play a

significant role for high-energy radiation.

Here the Cohen, Treves, Holloway (CTH) argument on the energy - angular momentum (L/E) budget is recalled and then we explore some consequences of assuming emission within the r_c.

4.7.1 The CTH Argument

Let $\dot{N}(r)$ be the number of photons of frequency ν released at a cylindrical coordinate r in the unit of time. The energy loss of the system would be

$$\frac{dE}{dt} = \dot{N} h\nu \tag{4.1}$$

The angular momentum loss is

$$\frac{dL}{dt} \leq \dot{N} r \frac{h\nu}{c} \tag{4.2}$$

with the equal sign only if the photons are emitted in an equatorial plane perpendicularly to the radius. Therefore

$$\frac{dL}{dt} / \frac{dE}{dt} \leq \frac{r}{c}. \tag{4.3}$$

The energy and angular momentum of a rotating sphere are $E = \frac{1}{2} I\omega^2$ and $L = I\omega$, where I is the moment of inertia which is supposedly constant. Therefore

$$\frac{dL}{dt} / \frac{dE}{dt} = \frac{1}{\omega}. \tag{4.4}$$

Combining with (3) one obtains

$$r > \frac{c}{\omega}. \tag{4.5}$$

This says that in order to satisfy the balance of angular momentum and energy loss a single photon has to be released at $r > c/\omega$. The same argument applies to relativistic particles. Note that in the classical dipole wave solution, as shown explicitly by [64] the angular and energy loss balance is satisfied.

It is obvious that a model of pulsar emission which prescribes all energy release at the polar cap is unacceptable, as well as models where the spark gap is located at $r < r_c$. The same problem does not apply to pulsars in binary systems, pulsar wind nebulae or blazars, as the jet there is responsible for the dissipation of the excess angular momentum of the photons.

4.8 Consequences of the Activation of a Polar-Cap Spark Gap

Models could consider two spark gaps, one at the polar cap and one at the outer gap, and the E/L balance could be globally preserved. This may occur also in the case of a continuous emission region (e.g. *slot gaps*). For consistency, such models should clarify which is the physical mechanism that warrants that the luminosity distribution does preserve the E/L balance.

Qualitatively one can make the following argument. If part of the energy is released at $r < r_c$, there is a local excess of angular momentum which one has to dispose of. The only solution we can think of is that the excess angular momentum is transferred to the magnetosphere, which expands to the periphery. The particle component may generate a relativistic wind, which finally accounts for the angular momentum excess. The stretching of the magnetic field lines, may be a way of enhancing the radiation from an external gap, again favoring the global E/L balance. The appearance of a sizable polar cap emission could rather induce some sort of global instability, which, one can argue, will quench the polar cap gap.

In conclusion we expect that the activation of a polar cap gap, if it ever occurs, should be followed by a) a modification of the relativistic wind, b) enhanced power from the outer gap, c) a global instability. The three effects may coexist or one or two may prevail. The alternative, which is simpler and we favor, is that there is no internal polar gap. The next Chapter presents a scenario where the emission mechanism seems to originate close to the polar caps but, as it is shown, this can only constitute an exception to the standard pulsar behavior.

Chapter 5

High Magnetic Field Pulsars

Despite its lower sensitivity in the GeV band, the *GRID* on board *AGILE* has an effective area below 200 MeV ($\sim$200 cm^2 at 50 MeV) comparable with that of *Fermi*-LAT. For this reason, after the advent of *Fermi*-LAT, we chose to concentrate the *AGILE* observations on "soft" targets. We found a correlation between some high-magnetic-field pulsars and a cutoff at low energies on their spectral properties. We investigated this connection in the two pulsars that we have observed with the lowest high-energy cutoff: PSR B1509–58 (J1513-5908) and PSR J1846–0258. Of both these works, the first published [177] and the second submitted to ApJ, I have been the principal investigator.

5.1 PSR B1509–58

PSR B1509–58 was discovered as an X-ray pulsar with the *Einstein* satellite during an observation of the supernova remnant (SNR) MSH 15-52 [198]. The source was soon also detected at radio frequencies by [150], with a derived distance supporting the association with the SNR ($d \sim 5.2$ kpc, as calculated from HI measurements from [79] and in agreement with the most recent distance derived using the dispersion measure [1]). With a period $P \simeq 150$ ms and a period derivative $\dot{P} \simeq 1.53 \times 10^{-12}$ s s^{-1}, assuming the standard dipole vacuum model, the estimated spin-down age for this pulsar is 1570 years (among the shortest for radio pulsars) and its inferred surface magnetic field is one of the highest observed for an ordinary radio pulsar: $B = 3.1 \times 10^{13}$ G, as calculated at the pole [2]. Its rotational energy loss rate is $\dot{E} = 1.8 \times 10^{37}$ erg/s.

[1] see the ATNF Pulsar Catalogue (http://www.atnf.csiro.au/research/pulsar/psrcat/) for the updated distance measurement derived from the dispersion measure.

[2] The magnetic field strength at the pole is twice the value quoted in the ATNF Pulsar Catalogue.

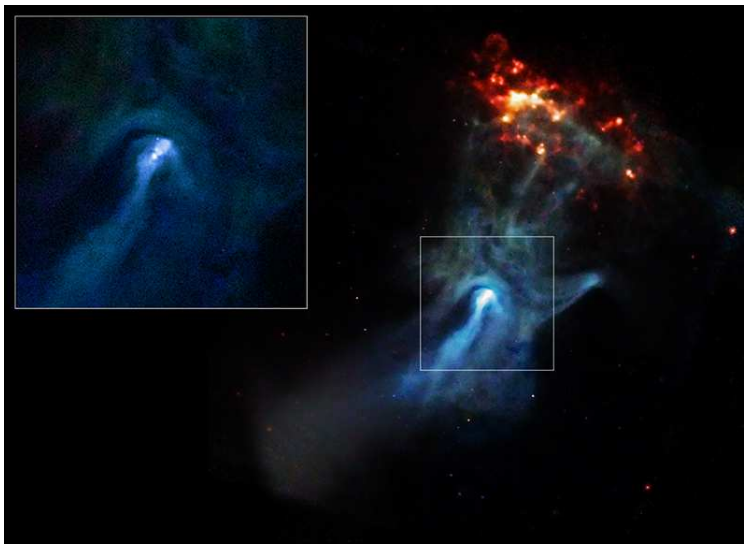

Figure 5.1 An image of the pulsar and its nebula as observed in X-rays by Chandra.

PSR B1509–58 and its nebula have been extensively observed in the X-rays since the Eighties with the *Einstein* and *EXOSAT* satellites. The detection of pulsed emission in the hard X-rays dates back to the early Nineties [116] with *Ginga* in the 2–60 keV energy range. During a 20 yrs-long radio monitoring [136], PSR B1509–58 has not shown any glitch activity, at variance with the general behavior of young radio pulsars. The analysis of Livingstone et al. [136], using radio and X-rays (collected with *RossiXTE*), yielded a very accurate measurement of the braking index of $n = 2.839 \pm 0.003$, close to the canonical value $n = 3$ for braking by magnetic dipole radiation in vacuum alone. Observations with the *ROSAT* [220], *ASCA* [207] and *BeppoSAX* [160] satellites were performed in the Nineties, characterizing the spectrum of the pulsed emission and the morphology of the remnant as possibly due to the presence of several components, interacting via collimated outflows from the pulsar. The nebula has been extensively observed with the *Chandra* satellite [78] and its emission has been found up to the TeV energies, with *CANGAROO* first [195] and more recently by *H.E.S.S.* [13].

The young age and the high rotational energy loss rate made this pulsar a promising target for the first generation of gamma-ray satellites. In fact, the instruments on board *CGRO* observed its pulsation at low gamma-ray energies: up to $E \sim 700$ keV with *BATSE* [233] and *OSSE* ([221], [155]), and in the 0.75 - 30 MeV band with *COMPTEL* [126], but it was not detected with high significance by *EGRET*, the instrument operating at the energies from 30 MeV to 30 GeV. This was remarkable, since all other known gamma-ray pulsars show spectral turnovers

well above 100 MeV [216]. Harding et al [90] suggested that the break in the spectrum could be interpreted as due to inhibition of the pair-production caused by the photon-splitting phenomenon [12]. The photon splitting appears, in the frame of the polar cap models, in relation with a very high magnetic field. An alternative explanation is proposed [235] using a three dimensional outer gap model. Zhang & Cheng propose that the gamma-ray emission is produced by synchrotron-self Compton radiation above the outer gap.

Ten years after the *CGRO*, the observation in the gamma-ray band are possible again with the advent of *AGILE* and *Fermi*-LAT. In particular, despite its lower sensitivity in the GeV band, the *GRID* on board *AGILE* has an effective area below 100 MeV ($\sim$200 cm^2 at 50 MeV) comparable with that of *Fermi*-LAT. *AGILE* obtained the first detection of PSR B1509–58 in the *EGRET* band [172] confirming the occurrence of a spectral break, although no precise flux measurements were possible due to low counts statistics. Soon afterwards, *Fermi*-LAT also reported its detection of PSR B1509–58 [1]. Later on we presented the results of a ~ 2.5 yr monitoring campaign of PSR B1509–58 with *AGILE*[177], that improved counts statistics, and therefore light curve characterization, with respect to earlier *AGILE* observations. With these observations the spectral energy distribution (SED) at energies $E < 300$ MeV, where the remarkable spectral turnover is observed, can be assessed.

5.1.1 Gamma-Ray Observations of PSR B1509–58

PSR B1509–58 is within the same region of the sky as the Vela pulsar, an area to which *AGILE* devoted a large amount of observing time Gamma-ray photons for this pulsar were collected and analyzed since July 2007, up to late October 2009 when *AGILE* started observing in spinning mode. The large *AGILE* effective area and long observing time ($\sim$ 260 days on target) provided a total exposure of 3.8×10^9 cm^2 s ($E > 100$ MeV) during this 2.5 yr period which gave our observations a good photon harvest from this pulsar.

Simultaneous radio observations of PSR B1509–58 with the 64 m Parkes radio telescope in Australia are ongoing since the epoch of *AGILE*'s launch (MJD 54220; 2007 April 30), as part of a timing project for the gamma-ray satellites [231], and cover all of *AGILE*'s observations. A total of 47 pulsar time of arrivals (ToAs) were collected between April 2007 (MJD 54220) and February 2010 (MJD 55233), leading to a r.m.s. of the residuals of 900 μs, showing the goodness of the

timing model that allowed accurate pulse phase tagging of the gamma-ray photons. No glitch was detected in the radio analysis. Strong timing noise was present, as expected from a young pulsar, and it was accounted for using the *fitwaves* technique developed in the framework of the TEMPO2 radio pulsar timing software [103, 104]. Using the radio ephemeris provided by the Parkes telescope, we performed the folding of the gamma-ray light curve including the wave terms (see [173]). An optimized analysis followed, aimed at cross-checking and maximization of the significance of the detection, including an energy-dependent event extraction angle around the source position based on the instrument PSF. Only high confidence gamma-ray photons (G) were used for the timing analysis of this pulsar. The chi-squared (χ^2)-test applied to the 10 bin light curve at $E > 30$ MeV gave a detection significance of $\sigma = 4.8$. The unbinned Z_n^2-test applied to the photons' arrival times gave a significance of $\sigma = 5.0$ with $n = 2$ harmonics. The difference between the radio and gamma-ray ephemerides was $\Delta P_{radio,\gamma} \leq 10^{-9}$ s, well within the error in the parameters, showing perfect agreement among radio and gamma-ray ephemerides as expected, further supporting our detection and *AGILE* timing calibration.

We observed PSR B1509–58 in three energy bands. We obtained 1210 ± 400 pulsed counts ($\sim 5\%$ of the total source, diffuse gamma-ray emission and residual particle background counts) at energies $30 < E < 100$ MeV, 820 ± 360 pulsed counts ($\sim 7\%$ of the total counts) at energies $100 < E < 500$ MeV. The pulsed flux was computed considering all the counts above the minimum of the light curve (see [173]) We did not detect pulsed emission at a significance $\sigma \geq 2$ for $E > 500$ MeV and thus we can only give an upper limit at 1σ of < 270 pulsed counts. This is consistent with the fact that only a 1.4σ detection is reported at $0.3 < E < 1$ GeV with the *Fermi*-LAT data [1].

5.1.2 Light Curve and Spectrum of PSR B1509–58

Light Curve Characterization The gamma-ray light curves of PSR B1509–58 for different energy bands are shown in Figure 5.2. The *AGILE* light curve above 30 MeV shows two peaks at phases $\phi_1 = 0.39 \pm 0.02$ and $\phi_2 = 0.94 \pm 0.03$ with respect to the single radio peak, here put at phase 0, as obtained from the Parkes ephemeris. The peak positions and widths in term of phase are calculated using a Gaussian fit, yielding a FWHM of $0.29(6)$ for the first peak and of $0.13(7)$ for the second peak, where we quote in parentheses (here and throughout this Chapter) the

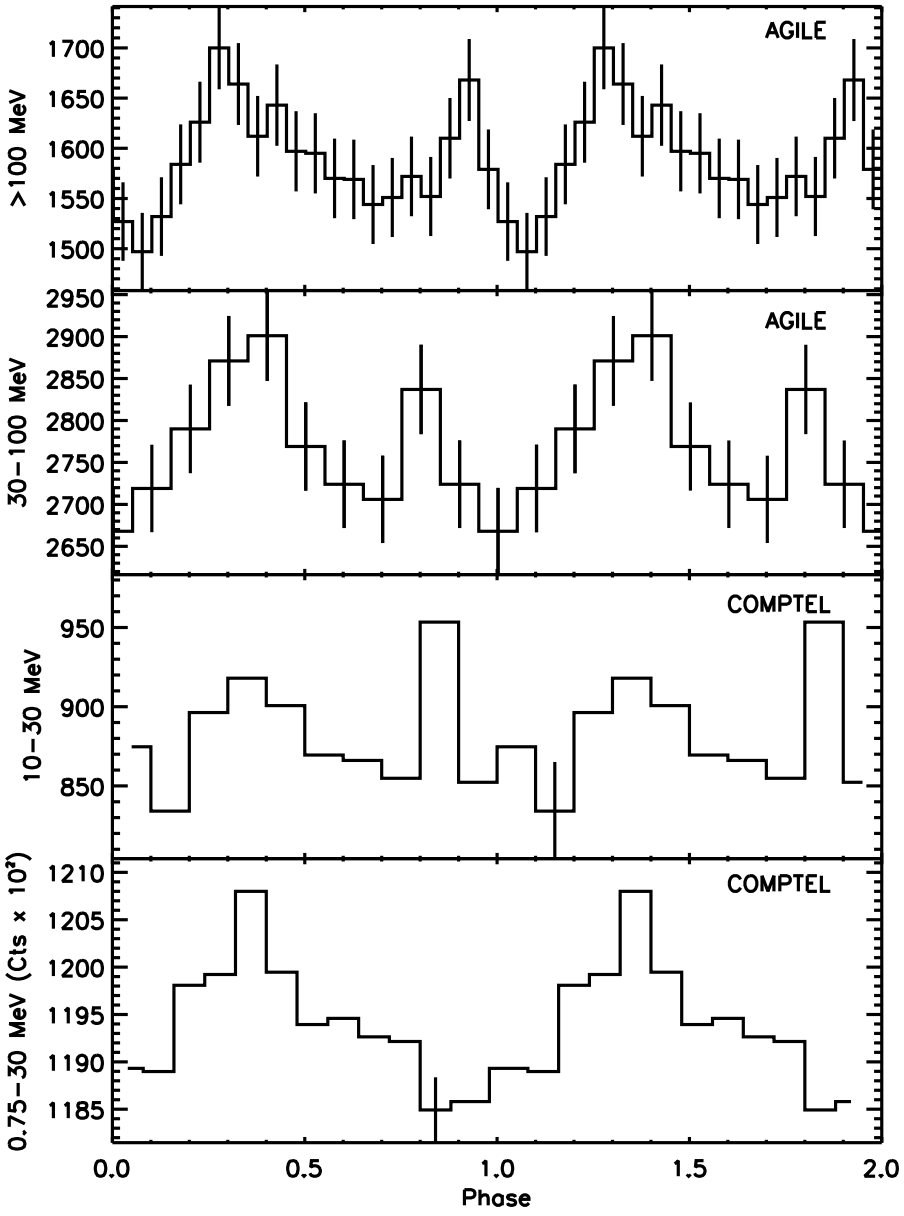

Figure 5.2 Phase-aligned gamma-ray light-curves of PSR B1509–58. Radio main peak is at phase 0. The start of the y-axis coincides with the minimum of the pulsed fraction and, consequently, with the background level. From top to bottom: *AGILE* high energy band ($>$ 100 MeV), 20 bins, 7.5 ms resolution; *AGILE* "soft" energy band ($<$ 100 MeV), 10 bins, 15 ms resolution; *COMPTEL* high energy band (10–30 MeV) and *COMPTEL* whole bandwidth (0.75–30 MeV) (from [126]).

1σ error on the last digit. The errors considered are statistical, as the systematic errors do not affect the measurements of the pulsed counts. The first peak is coincident in phase with the X-ray single broad peak and with *COMPTEL* peak (see [126] and references therein). In its highest energy band (10–30 MeV) *COMPTEL* showed the hint of a second peak (even though the modulation had low significance, 2.1σ), which is also visible in the light curve derived from *EGRET* observations (30–100 MeV), despite the fact that *EGRET* did not have a significant detection of the pulsar above 100 MeV [76]. This second peak is coincident in phase with *AGILE*'s second peak (Figure 5.2) in its lower energy band while it appears slightly shifted at energies above 100 MeV. A possible explanation for this shift is discussed in Section 5.1.3. *AGILE* thus confirms the previously marginal detection of a second peak, statistically significant at 5σ, calculated using a chi squared statistics test.

***Fermi*-LAT Analysis** Using data from the beginning of the mission up to January 2011, and an updated ephemeris from Parkes data, we analyzed *Fermi*-LAT observations of PSR B1509–58. As shown in Figure 5.3, *Fermi*-LATlight curve in this longer time span analysis, with respect to the one from [1], presents high enough statistics to allow the characterization at low energies (< 150 MeV), where the second peak can be observed. The peak disappears when higher energies are considered. Again we refer to Section 5.1.3 for a possible explanation if this trend.

Spectral Analysis Based on our exposure, calculated by the *GRID* scientific analysis task AG_ExmapGen, we derived the gamma-ray flux from the number of pulsed counts. This method, though typically giving higher statistical errors than the likelihood analysis, is more accurate and sensitive to evaluate the flux of this pulsar, given its soft spectrum (and the correspondingly large PSF) and the contribution from other nearby and brighter sources and possibly from the pulsar wind nebula (PWN), that all affect the spatial analysis. With this method, we do not incur in the problem of modeling the background, which affects the likelihood analysis. In fact, the counts below the pulsed threshold, which constitute the background, are discarded, so that the observed pulsed counts do belong to the pulsar. We divided *AGILE* bandwidth into three energy intervals: 30–100 MeV, 100–500 MeV and above 500 MeV. The pulsed fluxes thus obtained were $F_\gamma = 10(3) \times 10^{-7}$ ph cm^{-2} s^{-1} in the 30–100 MeV band, $F_\gamma = 1.8(8) \times 10^{-7}$ ph cm^{-2} s^{-1} in the 100–500 MeV band and a 1σ upper limit $F_\gamma < 8 \times 10^{-8}$ ph cm^{-2} s^{-1} for $E > 500$ MeV. Finally, from the total number of pulsed

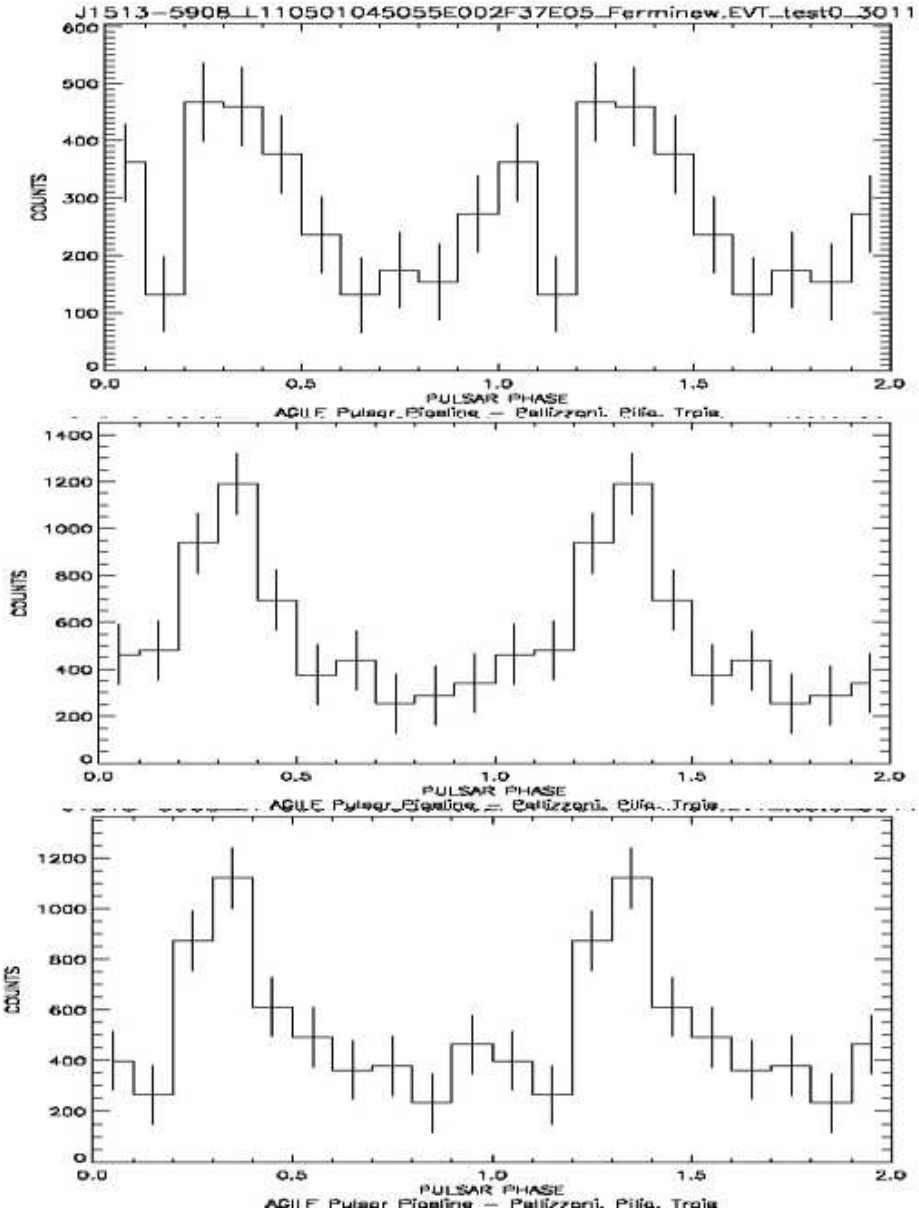

Figure 5.3 *Fermi*-LAT light curves for different energy bands: upper panel for $E < 150$ MeV, middle panel for $E < 300$ MeV, bottom panel for $E < 500$ MeV.

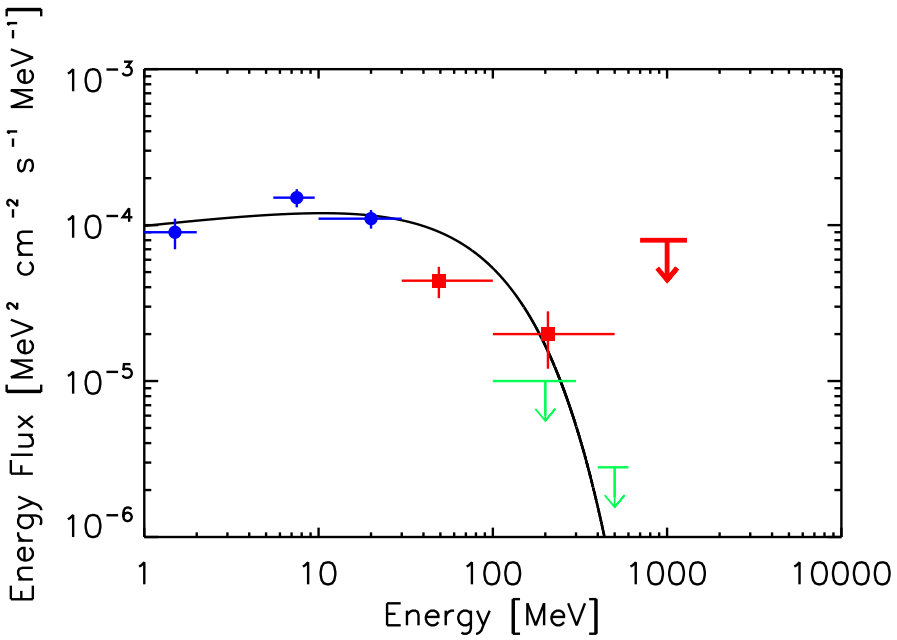

Figure 5.4 Spectral energy distribution of PSR B1509–58 (solid line) obtained from a fit of pulsed fluxes from soft to hard gamma rays. The three round points represent *COMPTEL* observations [126]. The two square points represent *AGILE* pulsed flux in two bands ($30 < E < 100$ MeV and $100 < E < 500$ MeV). The red horizontal bar and arrow emerging from it represent *AGILE* upper limit above 500 MeV. The two green arrows represent *Fermi*-LAT upper limits [1].

counts we obtained a pulsed flux at $E > 30$ MeV $F_\gamma = 12(2) \times 10^{-7}$ ph cm^{-2} s^{-1} for $E > 30$ MeV.

Figure 5.4 shows the SED of PSR B1509–58 based on *AGILE*'s and *COMPTEL*'s observed fluxes. *Fermi*-LAT upper limits are also shown, which are consistent with our measurements at a 2σ confidence level. *COMPTEL* observed this pulsar in three energy bands: 0.75–3 MeV, 3–10 MeV, 10–30 MeV, suggesting a spectral break between 10 and 30 MeV. *AGILE* pulsed flux confirms the presence of a soft spectral break. As shown in Figure 5.4, we modeled the observed *COMPTEL* and *AGILE* fluxes with a power-law plus cutoff fit using the Minuit minimization package [108]: $F(E) = k \times E^{-\alpha} \exp[-(E/E_c)^\beta]$, with three free parameters: the normalization k, the spectral index α, the cutoff energy E_c and allowing β to assume values of 1 and 2 (indicating either an exponential or a super-exponential cutoff). No acceptable χ^2 values were obtained for a super-exponential cutoff, the presence of which can be excluded at a 3.5σ confidence level, while for an exponential cutoff we found $\chi^2_\nu = 3.2$ for $\nu = 2$ degrees of freedom, corresponding to a null hypothesis probability of 0.05. The best values thus obtained for the parameters of the fit were: $k = 1.0(2) \times 10^{-4}$ s^{-1} cm^{-2}, $\alpha = 1.87(9)$, $E_c = 81(20)$ MeV.

We performed an analysis of the ratio between the two peak heights. The second peak appears in the *COMPTEL* band 10–30 MeV and is observed with *AGILE* up to $E \leq 500$ MeV: it is harder than the first peak in the *COMPTEL* energy band, and it is present at all energies in the *AGILE* energy band, so that it might possibly be harder even at *AGILE*'s energies but the low statistics at high energies do not allow us to discriminate.

As a consistency check for the pulsed fluxes reported above, a maximum likelihood analysis in a region of 10 degrees around the source position was performed to assess possible unpulsed contribution from the PWN, although no detection was reported in the First Catalog of High-Confidence Gamma-ray Sources detected by the *AGILE* satellite [179]. The likelihood analysis (see [154] and for Agile in particular, details will be provided in Chen et al. in preparation) took into account the numerous sources present in this crowded region (including the extremely bright nearby gamma-ray pulsar J1509-5850, [229]). The upper limit found in the *AGILE* energy range by likelihood analysis ($F_\gamma < 40 \times 10^{-8}$ ph cm^{-2} s^{-1} above 100 MeV) is above the corresponding pulsed flux above 100 MeV ($F_\gamma = 21(6) \times 10^{-8}$ ph cm^{-2} s^{-1}). This is compatible with the fact that the timing analysis is expected to have for this target a better sensitivity (with

respect to the likelihood analysis). It is worth noting that PSR B1509–58 is also not detected by likelihood analysis by *Fermi*-LAT [1] apart from the > 1 GeV energy band where the emission could be related to the PWN seen by *H.E.S.S.* ([13]).

5.1.3 Possible Explanations for the Soft Spectrum

Pulsar magnetosphere models are usually divided into two categories, depending on the sites for the high-energy emission (see Section 1.3). In *polar cap* models the emission comes from the regions near the neutron star surface, while *outer gap* models predict that the emission be originated in the regions close to the light cylinder. Alternative models predict an emission zone encompassing the whole magnetosphere, which departs from the external rim of the polar cap region: these are the *slot gap* models [163]. Different models predict different spectral and geometrical properties. The bulk of the spin-powered pulsar flux is usually emitted in the MeV-GeV energy band with spectral breaks at ≤ 10 GeV (see [7] or e.g. [18]). PSR B1509–58 has the softest spectrum observed among gamma-ray pulsars, with a sub-GeV cutoff at $E = 0.08(2)$ GeV. In the following we discuss how the new *AGILE* observations can constrain the models for emission from the pulsar magnetosphere.

Polar Cap + Photon Splitting

When PSR B1509–58 was detected in soft gamma-rays but not significantly at $E > 30$ MeV, it was proposed that the mechanism responsible for this low-energy spectral break might be photon splitting [90]. The photon splitting [12] is an exotic third-order quantum electro-dynamics (QED) process expected when the magnetic field approaches or exceeds the *critical* value defined as $B_{cr} = m_e^2 c^3/(e\hbar) = 4.413 \times 10^{13}$ G, above which quantum effects become relevant. Most current theories for the generation of coherent radio emission in pulsar magnetospheres require formation of an electron-positron pair plasma developing via electromagnetic cascades. In very high magnetic fields the formation of pair cascades can be altered by the process of photon splitting: $\gamma \rightarrow \gamma\gamma$, which will operate as an attenuation mechanism in the high-field regions near pulsar polar caps. Since it has no energy threshold, photon splitting can attenuate photons below the threshold for pair production, thus determining a spectral cutoff at lower energies. This process cannot operate in the low fields of outer gap models because it only has appreciable reaction rates when the magnetic field is at least a significant fraction of the quantum critical field B_{cr}

(the attenuation coefficient T_{sp} scaling as $T_{sp} \propto (B/B_{cr})^6 = B'^6$), and magnetic fields strong enough are not present in the outer magnetosphere as $B \sim r^{-3}$.

In the case of PSR B1509–58 a polar cap model with photon splitting would be able to explain the soft gamma-ray emission and the low energy spectral cutoff, now quantified by *AGILE* observations. Since the mechanism of photon splitting is, as stated, strongly dependent on the magnetic field strength, if the field strength at the emitting region is $B' \geq 0.3$ (i.e. at heights below 1.3 neutron star radii, R_{NS}), the photon splitting is the dominant means of attenuation that inhibits efficient pair cascade production [90] and then gamma-ray emission. Based on the observed cutoffs, which are related to the photons' saturation escape energy, we can derive constraints on the magnetic field strength at emission, in the framework of photon splitting:

$$\varepsilon_{esc}^{sat} \simeq 0.077 (B' \sin\theta_{kB,0})^{-6/5} \tag{5.1}$$

where ε_{esc}^{sat} is the photon saturation escape energy and $\theta_{kB,0}$ is the angle between the photon momentum and the magnetic field vectors at the surface and is here assumed to be very small: $\theta_{kB,0} \leq 0.57^\circ$ (see [90]). Using the observed energy cutoff ($\varepsilon_{esc}^{sat} \simeq E = 80$ MeV) we find that $B' \geq 0.3$, which implies an emission altitude $\leq 1.3 R_{NS}$, which is the height where possibly also pair production could ensue. This altitude of emission agrees with the polar cap models (see e.g. [56]). A smaller energy cutoff, as in [90], would have implied even lower emission altitude and a sharper break, possibly caused by the total absence of pair production. It is apparent that small differences in the emission position will cause strong differences in spectral shape. This is possibly the reason for the different emission properties of the two peaks as observed in the total (*AGILE* plus *COMPTEL*) gamma-ray energy band and in the low-energy *Fermi*-LAT band. Also, a trend can be observed, from lower to higher energies (see the X-ray light curve for the trend in the first peak, as in Fig. 3 of [126]), of the peaks slightly drifting away from the radio peak. This we assume to be another signature of the fact that small variations in emission height can be responsible for sensible changes in the light curves in such a high magnetic field.

A soft cutoff (below 1 GeV) is in principle possible for polar cap scenarios even without invoking photon splitting attenuation. In polar cap models the strong magnetic field permits one-photon pair creation that attenuates super-GeV photons in Crab-like (e.g. PSR B1509–58, based on the parameter B/P^2) and Vela-like

pulsars (e.g. PSR B0656+14, see Section 5.1.4), whereas pair creation in outer gap models is mediated through the two-photon process involving surface thermal X-rays as targets. According to the calculations in [56], emission from the regions close to the polar caps is possible when $\alpha \sim \theta_b$, where α is the angle between the rotation and the magnetic axis and θ_b is the half-angle of the gamma-beam emerging from the polar cap. Furthermore, with emission from the polar caps, or some (≥ 2) polar cap radii, the pulse profile at high energies can have either one (as in the case of PSR B0656+14) or two peaks, with a peak-to-peak phase separation as large as 0.4–0.5 (albeit slightly smaller than what is observed for PSR B1509–58 at the highest energies).

Problems with the Polar Cap Model

The polar cap model as an emission mechanism is nowadays debated. On one hand theoretical objections arise from the fact that the angular momentum is not conserved in polar cap emission (see [50], [105], [219] and see Section 4.7). At the same time, mounting evidence of a preferential explanation of the observed gamma-ray light curves with high altitude cascades is also coming from the recent results by the *Fermi*-LAT satellite (see e.g. [7]). In the case of PSR B1509–58, the derived gamma-ray luminosity from the flux at $E > 1$ MeV, considering a 1 sr beam sweep is $L_\gamma = 4.2^{+0.5}_{-0.2} d^2_{5.2} \times 10^{35}$ erg/s, where $d_{5.2}$ indicates the distance in units of 5.2 kpc. While traditionally the beaming fraction (f_Ω) was considered to be the equivalent of a 1 sr sweep, nowadays (see e.g. [227]) the tendency is to consider a larger beaming fraction ($f_\Omega \approx 1$), close to a 4π sr beam. Using $f_\Omega = 1$ in our calculations, we would have obtained $L_\gamma = 5.8^{+0.1}_{-0.8} d^2_{5.2} \times 10^{36}$ erg s^{-1}. Thus the maximum conversion efficiency of the rotational energy loss ($\dot{E} \approx 1.8 \times 10^{37}$ erg s^{-1}, see Section 5.1) into gamma-ray luminosity is 0.3. Our result is not comparable with the typical gamma-ray luminosities above 100 MeV, because, for PSR B1509–58, this energy band is beyond the spectral break. Using *AGILE* data alone we obtained a luminosity above 30 MeV $L_\gamma = 5.2(6) d^2_{5.2} \times 10^{35}$ erg/s, again for a 1 sr beam. If the gamma-ray luminosity cannot account for a large fraction of the rotational energy loss, then the angular momentum conservation objection from [50] becomes less cogent for this pulsar, exactly as it happens for the radio emission.

Alternative Scenarios

If such an efficiency as that of PSR B1509–58 were incompatible with this conservation law, an interpretation of PSR B1509–58 emission should be sought in the frame of the three dimensional outer magnetosphere gap model, as was done by Zhang & Cheng [235]. According to this model, hard X-rays and low energy gamma-rays have the same origin: they are produced by synchrotron self-Compton radiation of secondary electron-positron pairs of the outer gap. Therefore, as observed, the phase offset of hard X-rays and low energy gamma-rays with respect to the radio pulse is the same, with the possibility of a small lag due to the thickness of the emission region. According to their estimates, a magnetic inclination angle $\alpha \approx 60^o$ and a viewing angle $\zeta \approx 75^o$ are required to reproduce the observed light curve. Similarly, for PSR B0656+14, it is argued [229] that large α and ζ angles are required to reproduce the observed light curve in the framework of outer gap models. Finally, using the simulations of [227], who produced a map of pulse profiles for different combinations of angles α and ζ in the different emission models, the observed light curve from *AGILE* is best reproduced if $\alpha \approx 35^\circ$ and $\zeta \approx 90^\circ$, in the framework of the two pole caustic model [69].

Since the parameters used for the application of the outer gap model to PSR B1509–58 were based on its former observations by *COMPTEL*, *AGILE* spectrum does not precisely fit the spectrum predicted by the model in [235]. Furthermore, the values of α and ζ required by this model are not in good agreement with the corresponding values obtained with radio measurements. In fact, Crawford et al. [53] observe that α must be $< 60^\circ$ at the 3σ confidence level. The prediction obtained by the simulations of [227] for slot gap emission is in better agreement with the radio polarization observations than what predicted in the outer gap framework. Furthermore, in the framework of the rotating vector model (RVM, see e.g. [140] and references therein), Crawford et al. [53] propose that, if the restriction is imposed that $\zeta > 70^\circ$ [158] then α must be $> 30^\circ$ at the 3σ level. For these values, however, the Melatos model for the spin down of an oblique rotator predicts a braking index $n > 2.86$, which is slightly inconsistent with the observed value ($n = 2.839(3)$, see Section 5.1).

5.1.4 Analogous Cases

The second softest spectrum and lowest energy cutoff (0.7(5) GeV) is that of PSR B0656+14, recently observed by *Fermi*-LAT [229]. The observed light curve

of PSR B1509–58 shows two peaks lagging the radio peak by, respectively, $\phi_1 = 0.39 \pm 0.02$ and $\phi_2 = 0.94 \pm 0.03$.

The scenario proposed by [90] is strengthened by its prediction that PSR B0656+14 should have a cutoff with an intermediate value between PSR B1509–58 and the other gamma-ray pulsars. The main reason for the parallel between the two pulsars was at the time the fact that they had, respectively, the highest and second highest inferred magnetic fields. At present, however, there are a handful of gamma-ray pulsars with higher magnetic field than PSR B0656+14 in the *Fermi*-LAT First Year Pulsar Catalog [7] which do not show a low energy cutoff. Nonetheless, PSR B1509–58 (see [126, 53]) and PSR B0656+14 [62, 229] both show evidence of being aligned rotators, which could imply polar cap emission, as is also hinted by [30].

For PSR B0656+14 no outer magnetosphere emission model seemed to satisfy the observed features and a lower magnetosphere model, with an aligned geometry between the rotational and magnetic axes, has been proposed and seems plausible from polarization studies. Its efficiency in the conversion of the rotational energy loss into gamma-ray luminosity is one of the lowest observed for the gamma-ray pulsars (see [172], [7]): $\eta = 0.01$, not violating the constraints imposed by the conservation of angular momentum. Also in the case of PSR B0656+14 (see previous Section), [229] conclude that the large values of α and ζ are somewhat at odds with the constraints from the modeling of the radio data and the thermal X-rays which seem to imply a more aligned geometry. A recent work on sub-luminous pulsars (ref) underlines the peculiar properties of the gamma-ray emission of this pulsar, which is significantly inefficient in the conversion of its rotational energy into gamma-ray luminosity: $L_{\gamma,B0656} = \frac{1}{20} L_{\gamma,heu}$ where $L_{\gamma,heu}$ is a heuristic luminosity defined as $L_{\gamma,heu} \approx (\dot{E} \times 10^{33}\mathrm{erg/s})^{1/2}$. Geometrical and energetic arguments show PSR B0656+14 incompatibility with outer gap emission.

Conclusions Improved radio polarization measurements would help placing better constraints on the pulsar geometry and therefore on the possibility of a gap in the extended or outer magnetosphere, but the quality of the polarization measurements from [53] is already excellent, the problem being that PSR B1509–58, like most pulsars, only shows emission over a limited pule phase range and therefore the RVM models are highly degenerate. At present the geometry privileged by the state of the art measurements is best compatible with polar cap models. Higher statistics in the

number of observed gamma-ray pulsars could help characterize a class of "outliers" having gamma-ray emission from the polar caps, which potentially constitute a privileged target for *AGILE*.

5.2 Kes 75

Kes 75 (G29.7–0.3; [117, 33, 162, 165, 156]) is a young shell-type supernova remnant (SNR) resembling the Crab Nebula, with small-scale features and a central compact synchrotron wind nebula. Its long-sought pulsar, PSR J1846–0258, was discovered in X-rays thanks to timing analysis of *RXTE* and *ASCA* data [83], but it remains undetected at radio frequencies [22].

PSR J1846–0258 is a relatively slow pulsar ($P \sim 324$ ms) with a high slow-down rate ($\dot{P} \sim 7 \times 10^{-12}$ ss^{-1}). If standard dipole magnetic braking is assumed, its spin-down age, $\tau_{sd} \simeq 723$ yr, in agreement with the SNR association, makes it the youngest pulsar known. For a neutron star with radius of 10 km and moment of inertia of 10^{45} g cm^2, the derived spin-down power is $\dot{E} = 8 \times 10^{36}$ erg s^{-1}, while the inferred dipole magnetic field intensity on the surface (at the magnetic equator) is $B \sim 4.9 \times 10^{13}$ G, exceeding the quantum critical value ($B_{\rm QED} = m_e c^3/e\bar{h} = 4.413 \times 10^{13}$ G). Only few "ordinary" pulsars have magnetic fields this strong (see e.g. [113]) and interestingly PSR J1846–0258, long-considered to be exclusively rotation powered, has displayed behaviors formerly associated only with magnetars (i.e. pulsars whose emission is mainly powered by magnetic field decay), including large flux and spectral variations and the emission of magnetar-like short bursts and even an outburst episode [81, 129, 135, 138].

Pulsed emission from PSR J1846–0258 was observed up to a few hundreds keV with *INTEGRAL* and *RXTE* [125], but the source is not among the *Fermi*-LAT gamma-ray pulsars [7]. Using 3 years of pointing data plus 1 year of sky-survey data, *AGILE* could detect from this pulsar gamma-ray emission above 30 MeV. This is the second source, after PSR B1509–58 (J1513–5908, [177]), showing a very soft gamma-ray spectrum with a low-energy cutoff, possibly related to a close to quantum critical magnetic field.

5.2.1 Gamma-Ray Observations of Kes 75

Gamma-ray photons for PSR J1846–0258 were collected and analyzed starting in July 2007, up to late October 2009 in pointing mode and then from November 2009 till November 2010 in spinning mode. The large *AGILE* effective area and long

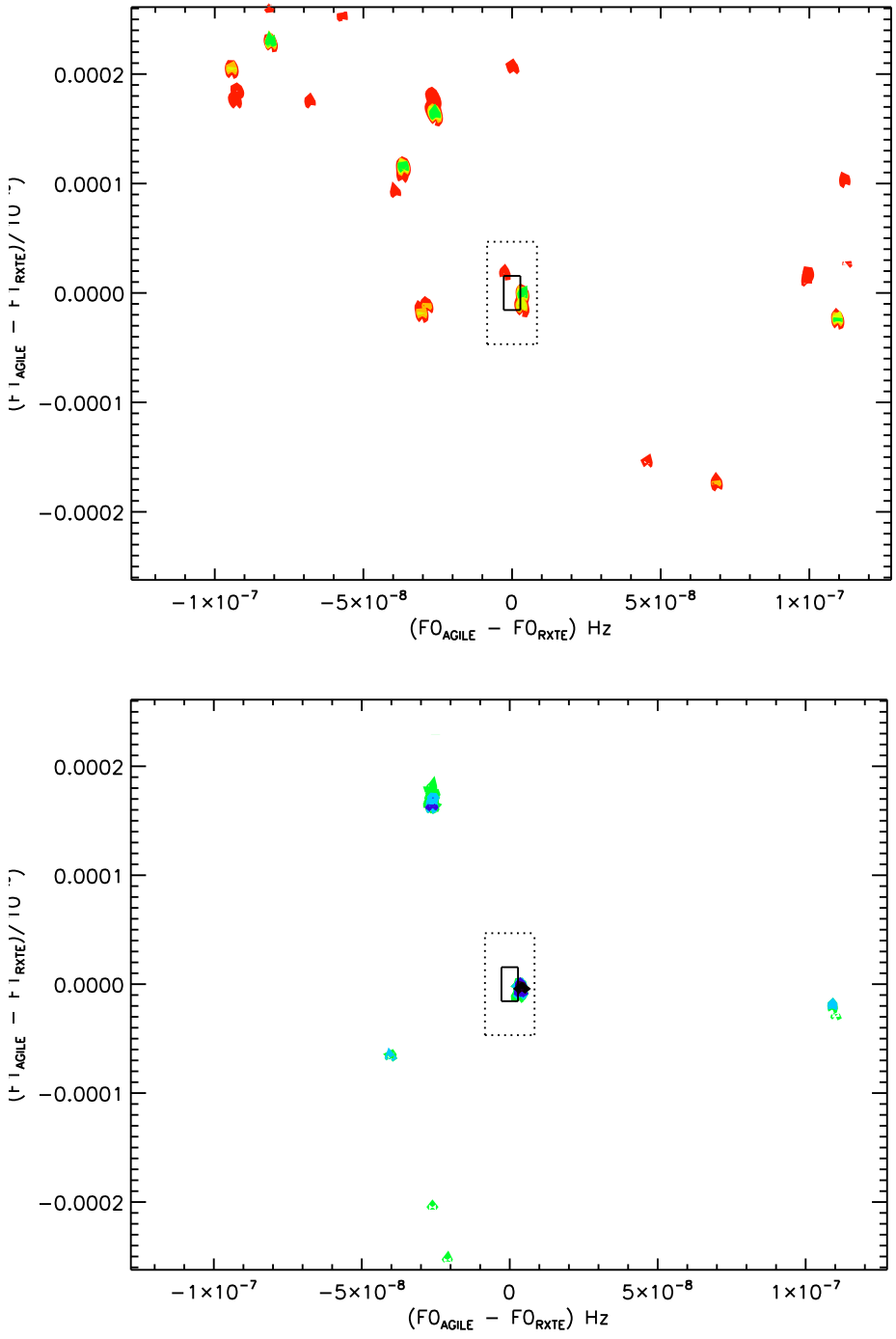

Figure 5.5 $\nu - \dot{\nu}$ (F0–F1) contour plots centered on the values obtained from the *RXTE* ephemeris and extended over $> 40\sigma$ around *RXTE* frequency and over $> 15\sigma$ around *RXTE* frequency derivative. The central boxes represent 1σ (internal continuous line) and 3σ (external dotted line) errors around the *RXTE* ephemeris values. The upper panel represents the results of the Z^2–test, the lower panel represents the results of the χ^2–test. The colors represent significance levels of the detection, with the following color coding: red 3σ, orange 3σ, yellow 3σ, green 4σ, light blue 4.2σ, blue 4.5σ, purple 5σ, black $> 8\sigma$. The significance excess outside the 3σ region are perfectly compatible with what is statistically expected for this number of trials (see text).

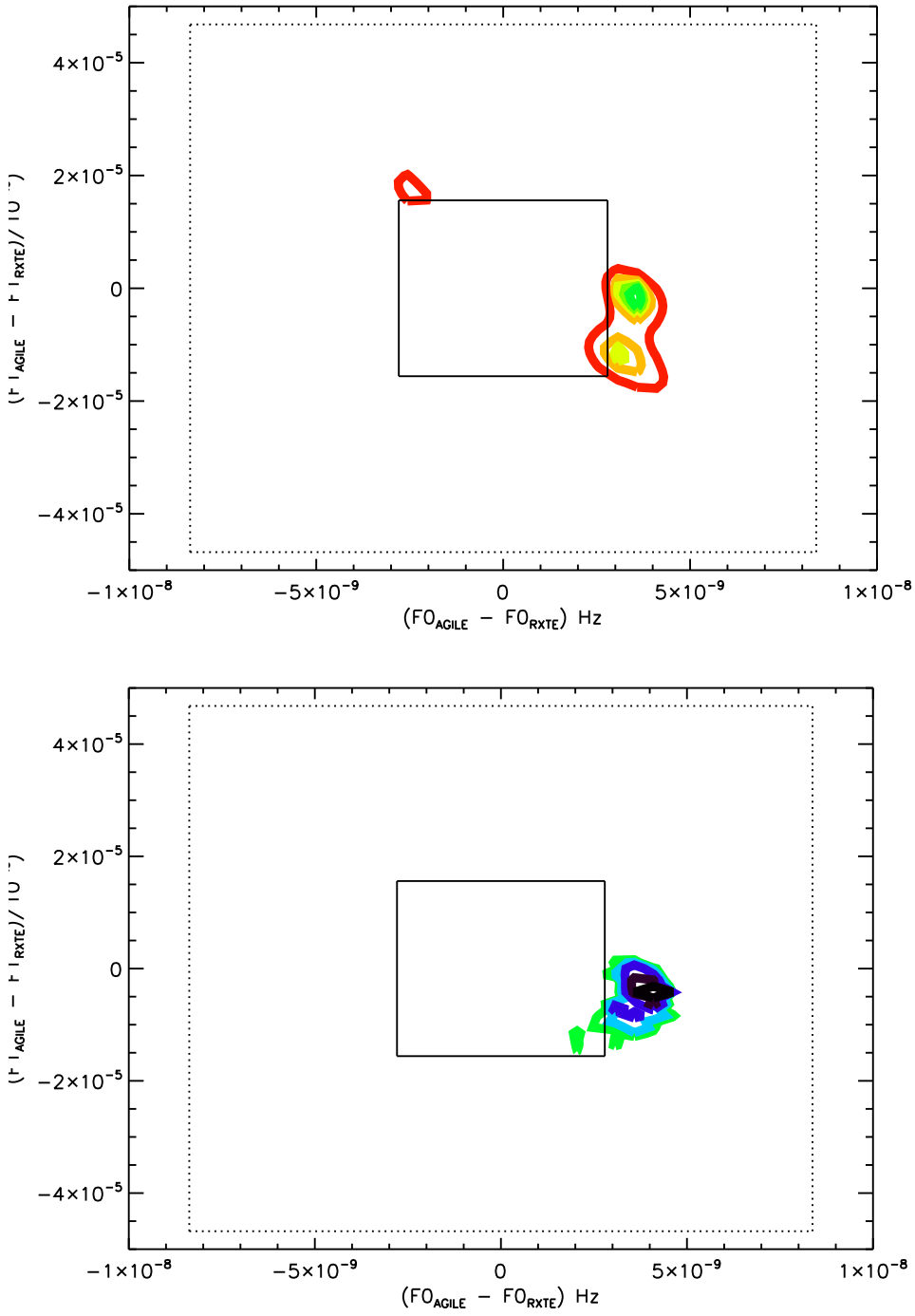

Figure 5.6 Close up on the 1σ to 3σ region of the $\nu - \dot{\nu}$ contour plots. As expected, the maximum significance is coincident in both tests and it represents the strongest excess for each plot.

observing time ($\sim$ 500 days on target) provide a total exposure of 3.7×10^9 cm^2 s ($E > 30$ MeV) during this over 3 yr period, which gives our observations a good photon harvest from this pulsar.

Simultaneous X-ray observations using *RXTE* were made using the Proportional Counter Array (PCA). The *RXTE* data on PSR J1846–0258 are unevenly spaced over 11 years from 1999 April 18 through 2010 April 22 (MJD 51286 – 55308). Observations taken between 1999 April 18 and 21 (MJD 51286 – 51289) are excluded because they cannot be unambiguously phase connected with the rest of the data. Data from 2000 January 31 to 2008 December 10 (MJD 51574 54810) were reduced and analyzed previously and details can be found in [137] and [135]. Data taken between 2009 January 27 and 2010 April 22 (MJD 54858 55308) are described in citelivingstone11.

Using the X-ray ephemeris provided by the *RXTE* observatory, we folded the gamma-ray photons, in correspondence to the X-ray values, including the *wave* terms (see [173] for details on *AGILE* pulsar timing analysis, and Sections 2.2.3 and 2.5.3 for the *FITWAVES* technique). High confidence (G) and low confidence (L) gamma-ray photons were used for the timing analysis of this pulsar. An optimized analysis was performed, aimed at cross-checking and maximization of the significance of the detection, including an energy-dependent event extraction angle around the source position based on the instrument point-spread-function (PSF). The chi-squared (χ^2)-test applied to the 10 bin light curve at $E > 30$ MeV gave a detection significance of $\sigma = 3.0$. The unbinned Z_n^2-test applied to the photons' arrival times gave a significance of $\sigma = 4.0$ with $n = 2$ harmonics.

We then performed a search around the *RXTE* ephemeris values. Weighting the corresponding detection probabilities with the number of independent ν and $\dot{\nu}$ trials ($n_{trials} \sim 220$), the weighted gamma-ray pulse significance is 5σ. We verified that our analysis procedure does not produce fake detections even considering much larger ν and $\dot{\nu}$ ranges ($n_{trials} > 10^4$) than those compatible with the X-ray ephemeris. To produce our timing solution, the position of the source was held at the *RXTE* coordinates reported above. We have checked that the positional uncertainty does not significantly affect barycentric corrections and thus the rotational parameters resulting from our timing analysis.

The present sensitivity did not allow a higher significance. While longer data-spans would help increase it, we did some side checks to support the robustness of the detection. Figures 5.5 and 5.6 show the $\nu - \dot{\nu}$ contour plot related to the gamma-

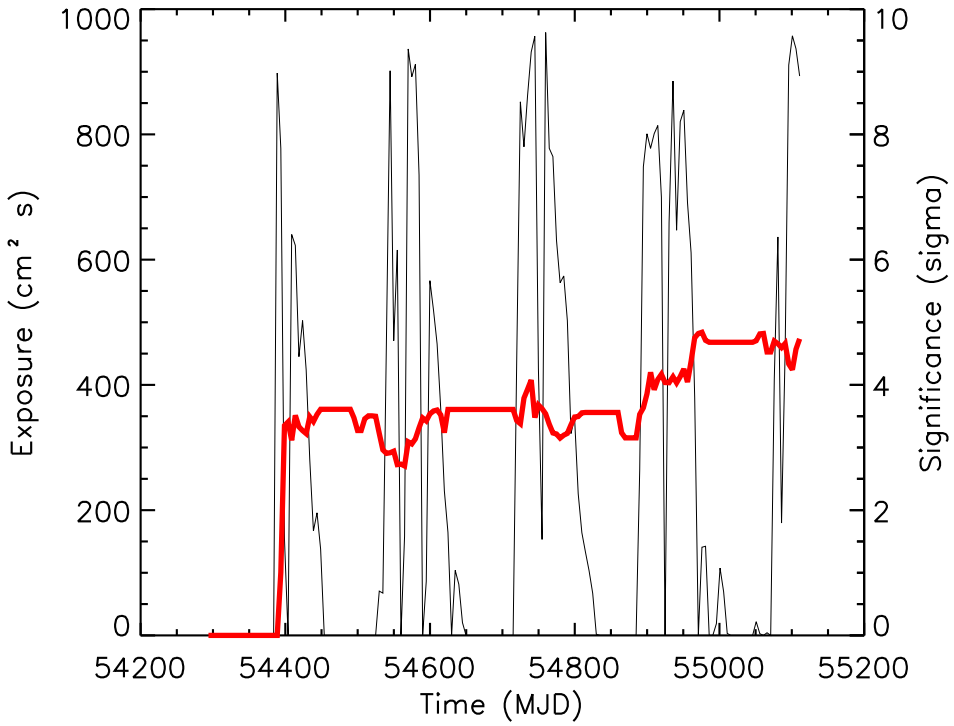

Figure 5.7 This figure illustrates the trend of the detection significance as a function of the exposure time for PSR J1846–0258. The exposure is indicated by the thinner black line, the significance by the thicker red line. As observed, the exposure is discontinuous, mainly due to the pointing mode of *AGILE* initial observing strategy. As expected, the significance follows the trend of the exposure and it slightly decreases when the time span considered grows but no exposure time is devoted to the source.

ray timing solutions with Z-test significance $> 4\sigma$. The inset shows the central region, comprising a 3σ uncertainty around the nominal values obtained from the *RXTE* ephemeris for ν and $\dot{\nu}$. As expected, the significance is here the highest while no other $> 4\sigma$ detection is observed outside this range, as is statistically predicted. Figure 5.7 shows how the detection significance increases with the exposure, a further confirmation of the reliability of the detection.

*F*ermi-LAT data were analyzed for the same interval of time as covered by the *R*XTE observations. The resulting light curve is not per se significant but it shows a trend not dissimilar from the one observed in the light curves from *AGILE*.

5.2.2 Light Curve and Spectral Behavior of Kes 75

The multi-wavelength light curves obtained using the three instruments are shown in Figure 2. The light curves show two peaks, that we modeled using a Gaussian fit: P1

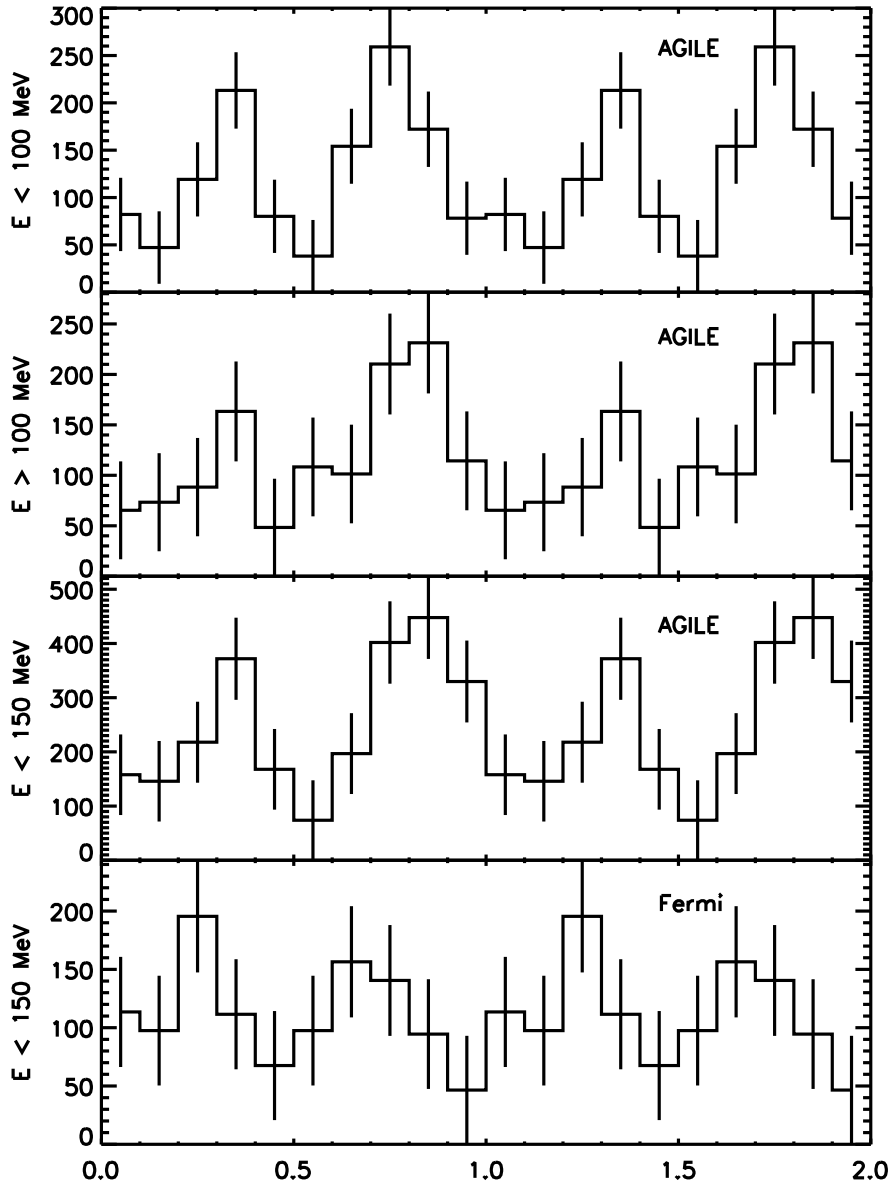

Figure 5.8 Background subtracted *AGILE* and *Fermi*-LAT light curves of PSR B1509–58are shown. From top to bottom: the *AGILE* light curves below and above 100 MeV and in the whole energy range and the *Fermi*-LAT light curve in the whole energy range.

at $\phi_1 = 0.33 \pm 0.03$ and P2 at $\phi_1 = 0.83 \pm 0.02$, with respect to the X-ray ephemeris. No significant gamma-ray emission is observed at energies above 150 MeV, and we indeed obtained the highest detection significance both in *AGILE* and *Fermi*-LAT using only photons up to this energy. The total number of pulsed photons observed by *AGILE* in the energy band between 30 and 150 MeV was 5100 ± 980. The pulsed gamma-ray flux obtained in this energy band is $F_\gamma = 1.8 \pm 3 \times 10^{-6}$ ph cm^{-2} s^{-1}.

We calculated the gamma-ray luminosity of PSR J1846–0258 in the energy range $30 - 150$ MeV. We used a distance estimate $d = 6$ kpc from [133], but keep it as a parameter, as well as the value of f_Ω, which takes into account the amplitude of the beam sweep and ranges from the typical $1/4\pi$ used for lower magnetospheric models, to a maximum of $\sim 4\pi$ for outer magnetospheric models. We found $L_\gamma = 6 \pm 1 \times 10^{36} d_6 f_\Omega$ erg s^{-1} which would correspond to a conversion efficiency of the rotational energy $\eta = 0.2$ given $\dot{E} = 8 \times 10^{36}$ erg s^{-1}. Such an efficiency is not easily comparable to the usual gamma-ray efficiencies that are applied to the emission at $E > 100$ MeV. It is as well difficult to compare them with the upper limits obtained by [168] for the *Fermi*-LAT observations ($L_\gamma \leq 26 \pm 19 \times 10^{34} f_\Omega$ erg s^{-1}, using a distance of 7.9 ± 2.8 kpc), as the $E > 100$ MeV analysis is not statistically significant per se for this pulsar and in this case L_γ is considered in the standard $E > 100$ MeV band.

5.2.3 The Peculiar Behavior of Kes 75

Originally interpreted as an ordinary rotation-powered pulsar, PSR J1846–0258 showed in recent years the presence of magnetically induced burst activity (see e.g. [138] for a review). Such activity and its very high surface magnetic field place PSR J1846–0258 in an intermediate region between the high-magnetic-field pulsars and magnetars. *AGILE* observations show the presence of high-energy emission, but only up to 150 MeV, suggesting a cutoff far below 1 GeV. Such a cut-off energy is smaller than that usually observed in rotation powered pulsars, but is similar to what has been observed in a restricted number of pulsars with a high magnetic field [229, 177, 168]. In the case of PSR B1509-58, [177] observed that the absence of high-energy emission above a certain threshold might be explained in the framework of the third-order quantum electrodynamics process of *photon splitting* [11, 90]. This process, in which a photon is split into two photons of lower energies, suppresses the emission at the highest energies. Photon splitting has no threshold and can therefore inhibit the pair production, unless the escape energy for

photons created by the photon splitting is reached at a height in the magnetosphere, depending on the magnetic field intensity, where the threshold for pair production is reached and it can ensue (see Discussion in [177]). This mechanism could explain the detection of radio emission of PSR B1509–58 and the non detection of PSR J1846–0258 which has an higher magnetic field and a lower energy cutoff with respect to PSR B1509–58.

The emission from photon splitting can only arise in regions where the magnetic field is a consistent fraction of the quantum critical field ($B \sim B_{cr} = m_e^2 c^3/(e\hbar) = 4.413 \times 10^{13}$ G), so it occur too far away from the polar caps of the pulsar, as the magnetic field scales as $B \sim r^{-3}$. The recent observations with *Fermi*-LAT and the IACTs *MAGIC* and *VERITAS* telescopes [7, 18, 146, 147, 223] seem to disfavor the polar cap model as a viable way to explain the gamma-ray emission from pulsars. Also, [168], in their work on *Fermi*-LAT observations of high magnetic field pulsars, found "standard" gamma-ray emission from PSR J1119–6127, with spectral behavior not in line with that of PSR J1846–0258. On the other hand, as is observed in [177], a few pulsars, such as B1509–58 [177], B0656+14 [229, 190], do not seem to fit in the constraints of the outer or extended magnetosphere models [47, 189, 163, 69]. In these cases, that are indeed rare among the known sample of 100 gamma-ray pulsars, the occurrence of two conditions may concur to allow emission from the polar caps, thus overcoming the theoretical limits of the model [219]. In [177] we proposed that the two conditions might be a high magnetic field and an aligned geometry. [190] also find that, though no firm conclusion can yet be drawn without more constraining geometry and distance measurements, all the sub-luminous pulsars of the *Fermi*-LAT sample seem present aligned geometries from the radio measurements. Unfortunately, no clear indication on the geometry of PSR J1846–0258 can be obtained in the absence of radio emission. The recent detection of gamma-ray emission from PSR J1119–6127 [168] seems to go in this same direction. They find that the geometry of this pulsar, as indicated by the radio observations, is not aligned and that the outer gap model best explains its emission: if the emission comes from the outer magnetosphere, then the magnetic field would have become much smaller. A further alternative explanation to the sub-luminosity of some pulsars has been proposed by [199], which again predict that polar cap emission, though modified [222]. This model can be invoked for pulsars with magnetic fields $B \sim 0.1 B_{cr}$ and periods $70 < P < 500$ ms.

5.2.4 From Pulsars to Magnetars?

It has been observed [134, 141, 122] that the link between rotation powered pulsars and magnetars may be evolutionary. Based on simple arguments of pulsars' theory [166, 193, 192], one can expect that a pulsar that has a braking index significantly smaller than the standard value for dipole only emission ($n = 3$) and experiences frequent glitch activity (that would alter its spin down in a partially permanent way), will be subject to an increase of its inferred magnetic field ($B = 3.2 \times 10^{19}\sqrt{P\dot{P}}$) and decrease of the inferred spin-down age ($\tau = \frac{1}{n-1}\frac{P}{\dot{P}}$). The characteristics of having a high inferred magnetic field and a very young spin-down age are typical of magnetars. PSR J1846–0258 may be at an advanced stage of this conversion, while PSR B1509-58, for example, could be at an earlier stage. According to [134], not all pulsars would follow this evolutionary path, but only those with high glitch activity. What differentiates among pulsars with different glitch activity may be for instance the configuration of the toroidal magnetic field which has recently been recognized to play a major role in the magnetic activity of a neutron star (see [186, 175] and the following). [175] believe that, since this behavior is regulated by the toroidal component, it should not be excluded, albeit rare, that outbursting episodes could be observed also in canonical pulsars, depending on their age and, consequently, glitch activity. [180] find that the pulsar- or magnetar-like behavior can be influenced by the toroidal magnetic field at birth and, in particular, that the toroidal field plays a relevant role in the magnetic activity if it exceeds the poloidal magnetic field. While they conclude that pulsars and magnetars can be simply considered as different versions of the same phenomenon, with a slight change in the initial parameters, it can also be argued that the evolution of the geometry of a pulsar (i.e. the progressive alignment of the spin and magnetic axes, [230]), causing changes to the toroidal field structure, can at the same time alter its magnetically-induced behavior. The recently measured $n = 0.9 \pm 0.2$ of pulsar J1734–3333 [72] seems to point towards this same direction.

[138] extensively discuss the decrease in the braking index, n, of PSR J1846–0258 following the glitch at the end of May 2006. The glitch was accompanied by a magnetar-like outburst, consisting of X-ray bursts and an increase in the source flux [81, 129] and it was followed by an increased level of timing noise and an $18 \pm 5\%$ decrease in the braking index (n). While the observed variation in n may be a result of the increased level of timing noise observed after the outburst, this issue should be resolved with ongoing timing observations of the source, as the level of timing noise

has been decreasing since the outburst, while the new value of n thus far appears to be stable. Thus, the two effects do not seem strongly correlated: timing noise typically depends on $\dot{\nu}$ and the braking index on the much larger variation in $\ddot{\nu}$, but both seem to confirm an increase in magnetic activity first suggested by the observed magnetar-like outburst. While no substantial increase ($\sim 0.3\%$) is observed in the poloidal magnetic field strength, these timing effects might be connected to changes in the magnetospheric currents (as discussed as length in [138]) and thus be a sign of an increase in the toroidal component of the magnetic field, which is the one that should be responsible for the magnetar-like activity [214, 215, 186].

5.3 Conclusions

No gamma-ray emission has been detected from magnetars so far [3]. It was thought [32] that the high magnetic field and photon splitting should be responsible for this absence, but, as gamma-ray emission has been detected in pulsars with high surface magnetic fields [7], the reason must be found elsewhere or be, at least, twofold. In [177] we tried to associate the high magnetic field to an aligned geometry in order to derive emission from the lower magnetosphere which should have a low energy cutoff. Here no geometry constraints are possible, due to the absence of radio emission [22], but an evolutionary scenario is proposed where the development of a toroidal field may progressively suppress the gamma-ray emission. *AGILE* observations, particularly well suited for this kind of ”soft” targets, will help to shed light on the mechanisms at play in high magnetic field pulsars.

Chapter 6

Pulsars and their Environments

Pulsars are known to power winds of relativistic particles that can produce bright nebulae by interacting with the surrounding medium. These Pulsar Wind Nebulae (PWNe) are observed by their radio, optical, and X-ray emissions, and in some cases also at TeV (tera-electron volt) energies, but the lack of information in the gamma-ray band has long precluded drawing a comprehensive multi-wavelength picture of their phenomenology and emission mechanisms. Using data from *AGILE*, we detected the Vela PWN in the energy range from 100 MeV to 3 GeV. We published this detection in Science [174] and I participated mainly to the pulsed analysis from which the subtraction started. This result gave constraints on the particle population responsible for the GeV emission and establishes a class of gamma-ray emitters that could account for a fraction of the unidentified galactic gamma-ray sources.

AGILE was also the first satellite to report on the abnormal flaring behavior coming from the region surrounding the Crab pulsar. We published the detection of the flare in [209] and put forward a tentative modeling of the flare in [224]. To both works I gave my contribution, plus the Pulsar Group analyzed possible causes deriving from the pulsar itself, as discussed in Section 3.4.1.

6.1 Pulsar Wind Nebulae

A Pulsar Wind Nebula (PWN) is a bubble of shocked relativistic particles, produced when a pulsars relativistic wind interacts with its environment. The central pulsar generates a magnetized particle wind, whose ultra-relativistic electrons and positrons radiate synchrotron emission across the electromagnetic spectrum [167, 187].

6.2 Emission from PWNe

Multi-wavelength observations of PWNe provide crucial information on the underlying particle spectrum and strongly constrain both the magnetic field strength and the stage of evolution. Of particular interest is the spectrum of low-energy particles contained in the PWN. These retain the history of early energy losses as well as possible signatures of features in the pulsar injection spectrum.

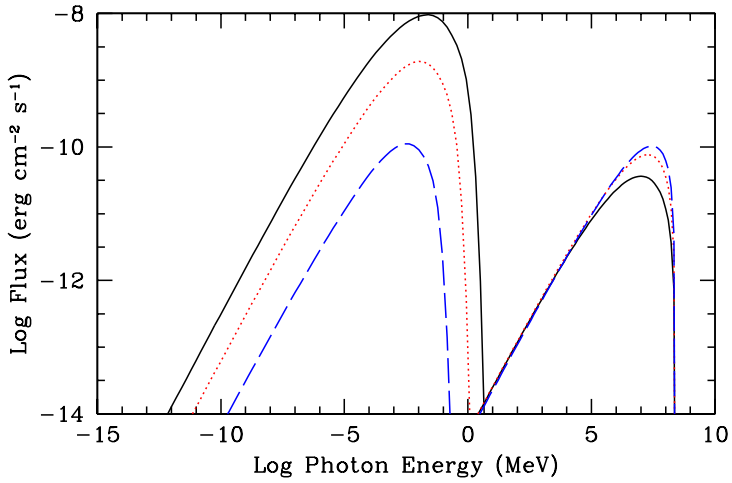

Figure 6.1 Synchrotron (left) and IC (right) emission (for scattering off of the CMB) from a PWN at ages of 1000 (solid), 2000 (dotted), and 5000 (dashed) years. Details in [200]

As particles are injected from a pulsar into its PWN, the resulting emission is determined by the evolved particle spectrum and magnetic field, as well as the energy density of the ambient photon field. The injected spectrum is often characterized as a power law: $Q(E_e,t) = Q_0(t)(E_e/E_0)^{-\alpha}$. The resulting emission spectrum is found by integrating the electron spectrum over the emissivity function for synchrotron and IC radiation using, respectively, the nebular magnetic field and spectral density of the ambient photon field. As illustrated in Figure 6.1 [201], the build-up of particles in the nebula results in an IC spectrum that increases with time. The synchrotron flux decreases with time due to the steadily decreasing magnetic eld strength associated with the adiabatic expansion of the PWN.

At the latest phases of evolution, when the nebula is very large and the magnetic field is low, the IC emission can provide the most easily detected signature. Such behavior is seen for a number of PWNe that have been identified based on their emission at TeV energies, and for which only faint synchrotron emission near the associated pulsars is seen in the X-ray band. The broadband spectrum of a PWN,

along with the associated dynamical information provided by measurements of the pulsar spin properties, and the size of the PWN and its SNR, place very strong constraints on its evolution and on the spectrum of the particles injected from the pulsar. Combined with estimates of the swept-up ejecta mass, this information can be used to probe the properties of the progenitor star and to predict the long-term fate of the energetic particles in the nebula. Recent multi-wavelength studies of PWNe, combined with modeling efforts of their evolution and spectra, have provided unique insights into several of these areas.

6.3 The Vela SNR and PWN

The Vela SuperNova Remnant (SNR) is the nearest SNR (distance $\approx$ 290 pc) containing a bright pulsar, PSR B0833–45, which has a characteristic age of 11,000 years and a spin-down luminosity of 7×10^{36} erg s^{-1} [211, 65]. This SNR extends over a diameter of $\sim 8^{\circ}$ and is known from early radio observations to embrace a number of regions of non-thermal emission including Vela X, a flat-spectrum radio component with a diameter of 100 arcmin near the center of the SNR.

6.3.1 The Region

Vela X, separated from the Vela pulsar by $\sim$ 40 arcmin, is generally interpreted as the pulsars radio synchrotron nebula [228, 68]. A diffuse emission feature ($\sim 1^{\circ}$ long) coincident with the center of Vela X was detected in X-rays (0.6 to 7.0 keV) by the *ROSAT* [152] and *ASCA* [152] satellites. It was first suggested that this feature, which is closely aligned with a filament detected at radio wavelengths, should correspond to the outflow jet from the pulsars pole [77, 96]. More recently, observations with Chandra [96] clearly unveiled the torus-like morphology of the compact X-ray nebula surrounding the pulsar and indicated that the center of Vela X lies along the extension of the pulsar equator, although bending to the southwest.

The detection of very-high-energy (VHE) gamma-rays from the Vela X region was claimed by *HESS* [14] and confirmed by *CANGAROO* [71]. The strong VHE source HESS J0835–455 (luminosity $\sim 10^{33}$ erg s^{-1} at energies above 0.55 TeV) coincides with the region of hard X-ray emission seen by the *ROSAT* satellite. The best-fit VHE emission centroid ($RA = 08^{h}35^{m}1^{s}$, $Dec = -45^{\circ}34'40''$) is $\sim 0.5^{\circ}$ from the pulsar position, and the VHE emission has an extension of $\sim$ 5 parsec $\times$4 parsec. The detection of Vela X at TeV energies demonstrated that this source emits non-thermal radiation, in agreement with the hypothesis that it corresponds to the

PWN, displaced to the south by the unequal pressure of the reverse shock from the SNR [37].

6.3.2 Relevance of High-Energy Observations for the Vela X PWN

The multi-wavelength spectrum of the center of Vela X can be modeled as synchrotron radiation from energetic electrons within the cocoon (radio and X-rays) and inverse-Compton (IC) emission from the scattering (by the same electron population) of the cosmic microwave background radiation (CMBR), the galactic far- infrared radiation (FIR) produced by re-radiation of dust grains, and the local starlight [57, 131, 61]. Alternatively, a hadronic model can be invoked for the gamma-ray emission from the Vela X cocoon, where the emission is the result of the decay of neutral pions produced in proton-proton collisions [106]. Observations in the high-energy (HE) MeV-GeV band are crucial to distinguish between leptonic and hadronic models as well as to identify specific particle populations and spectra.

Morphologically the Vela X PWN appears to consist of two emission regions: whereas X-ray ($\sim$ 1 keV) and VHE *HESS* gamma-ray observations appear to define a cocoon type shape south of the pulsar, radio observations reveal an extended area (including the cocoon area), also south of the Vela pulsar. Since no wide FoV observations of the synchrotron emission between radio and X-rays are available, it is not known how the lepton spectra of these two components connect and how the morphology changes with energy. [61] found that two distinct lepton spectra describe the respective radio and X-ray/VHE gamma-ray spectra, with a eld strength of 5 G self-consistently describing a radiation spectral break (or energy maximum) in the multi-TeV domain as observed by *HESS* (if interpreted as IC radiation), while predicting the total hard X-ray flux above 20 keV (measured by the wide FoV INTEGRAL instrument) within a factor of two. If this same field strength were also representative of the radio structure (including filaments), the implied IC component corresponding to the highest radio frequencies would reveal a relatively bright high energy gamma-ray structure at HE energies. A higher field strength in the filaments would imply fewer leptons in Vela X and hence a fainter HE signal.

6.4 *AGILE* Observations of the Vela X PWN

The Vela region was recently observed from 30 MeV to 50 GeV by *AGILE* and *Fermi*-LAT. *AGILE* observed the Vela pulsar for $\sim$ 180 days (within 60° from the center of instruments field of view) from July 2007 (54294.5 MJD) to September

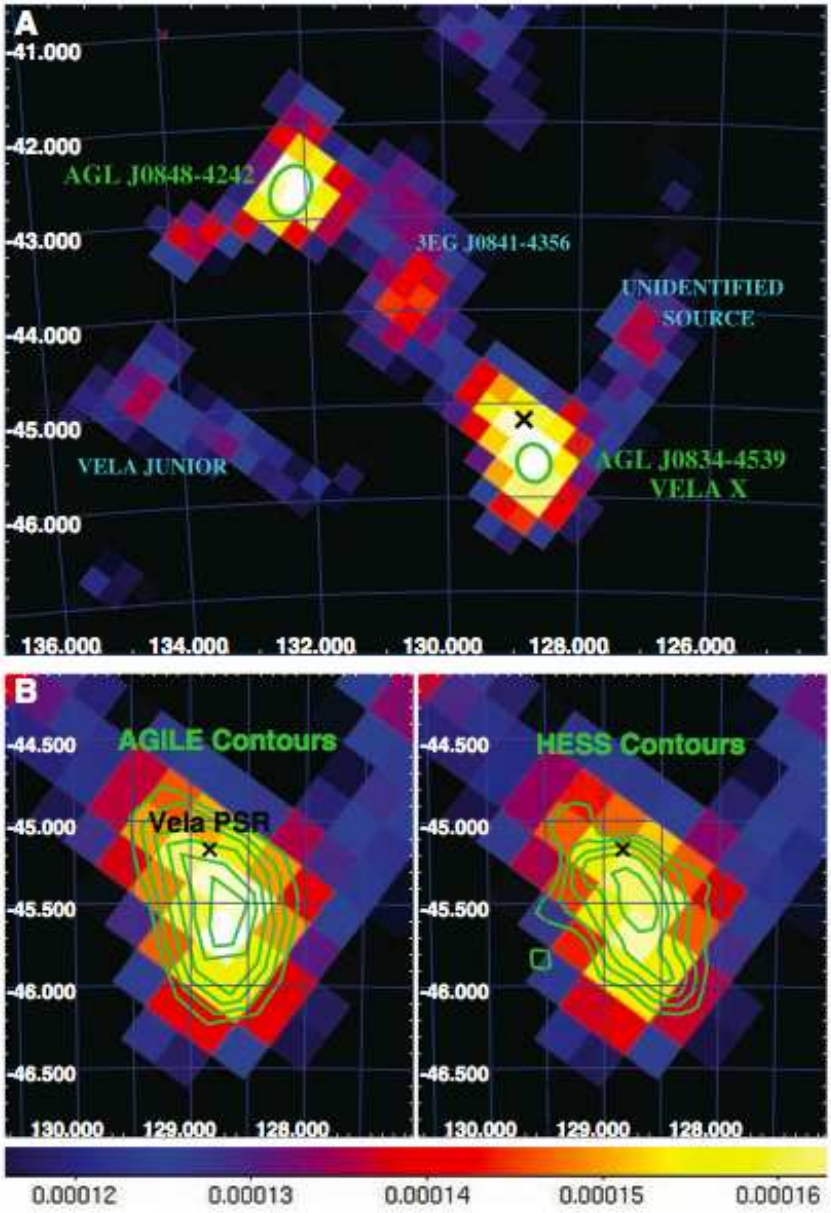

Figure 6.2 (**A**) Gaussian-smoothed *AGILE* intensity map (ph cm^{-2} s^{-1} sr^{-1} with pixel size $0.25^\circ \times 0.25^\circ$) at $E > 400$ around the Vela pulsar, including only off-pulse events (i.e., discarding events with phase corresponding to Vela pulsed emission). The neutron star position is marked with a black cross; green circles are the 68% confidence contours for the position of AGL J0848–4242 and AGL J0834–4539 (Vela X). The AGILE $E > 400$ MeV energy band is well suited for gamma-ray imaging and provides a good com- promise between the instrument-effective area (~ 400 cm^2; ~ 100 counts from AGL J0834–4539) and PSF ($\sim 1^\circ$, 68% containment radius), both parameters decreasing with energy. (**B**) The gamma-ray diffuse source AGL J0834–4539. *AGILE* contours (left) are in the range 1.4×10^{-4} to 1.6×10^{-4} ph cm^{-2} s^{-1} sr^{-1}, with step 4×10^{-6}. *HESS* contours (right) are from [14].

2009 (55077.7 MJD). To obtain precise radio ephemeris and to model the Vela pulsar timing noise for the entire *AGILE* data span, we made use of observations with the Mount Pleasant radio telescope (see Section 3.3). The Vela pulsar timing analysis provided a total of $\sim 40,000$ pulsed counts with energies between 30 MeV and 50 GeV; the difference between the radio and gamma-ray ephemeris was $< 10^{-11}$ s. Gamma-ray pulsed counts are concentrated within the phase interval 0.05 to 0.65 (where 0 is the phase corresponding to the main radio peak; see Section 3.3). We verified that no pulsed gamma-ray emission is detected outside this interval, consistent with reports of previous observations by *EGRET* [112], *AGILE* [173], and *Fermi*-LAT [2] .

With the aim of performing a sensitive search for close faint sources excluding the bright emission from the Vela pulsar, we discarded the time intervals corresponding to the phase interval 0.05 to 0.65. The analysis of the resulting off-pulse images (taking only events corresponding to the pulsar phase interval 0.65 to 1.05, for a total of $\sim 14,000$ events) unveiled few gamma-ray sources, none of which coincides with the Vela pulsar. A maximum likelihood analysis [208], performed on the $E > 100$ MeV data set within a region of 5° around the pulsar position,revealed two sources at better than 3σ confidence (Figure 6.2): AGL J0848–4242 (at galactic coordinates $l = 263^\circ.11$, $b = 0^\circ.65$, 68% confidence error circle radius $\sim 0^\circ.25$) and AGL J0834–4539 (at $l = 263^\circ.88$, $b = -3^\circ.17$, with confidence error circle radius $\sim 0^\circ.20$. A gamma-ray source coincident with the *EGRET* source 3EG J0841–4356 [94] was also detected with lower significance, and the Vela Junior SNR (RX J0852.0–4622) also possibly contributes to an excess of counts in the galactic plane around $l = 265^\circ.6$.

The brightest gamma-ray source in this complex scenery that lays hidden by the powerful Vela pulsar, is AGL J0834–4539. ~ 264 counts are detected by *AGILE* for this source, that is observed with a significance of $\sim 5.9\sigma$ and with a photon flux at $E > 100$ MeV is $F_\gamma = (35 \pm 7) \times 10^{-8}$ ph cm^{-2} s^{-1}. It is located $\sim 0^\circ.5$ southwest from the Vela pulsar position (outside the 95% source position confidence contour) and has a spatial extent of $\sim 1^\circ.5 \times 1^\circ$. Its shape is asymmetric and incompatible with the *AGILE* PSF. Therefore, possible residual emission from the pulsar (in principle associated to undetected weak peaks in the off-pulse interval of the light curve) cannot substantially contribute to this diffuse feature. No relevant systematic errors on positions, fluxes, and spectra (mostly due to uncertainties on the galactic gamma-ray diffuse emission model) affect *AGILE* sources detected around the 5σ

level. AGL J0834–4539 is positionally coincident with HESS J0835–455, the TeV source that is identified with the Vela X nebula, and has a similar brightness profile to it (Figure 6.2). This implies that AGL J0834–4539 is associated with the pulsars PWN.

6.4.1 Spectral Results

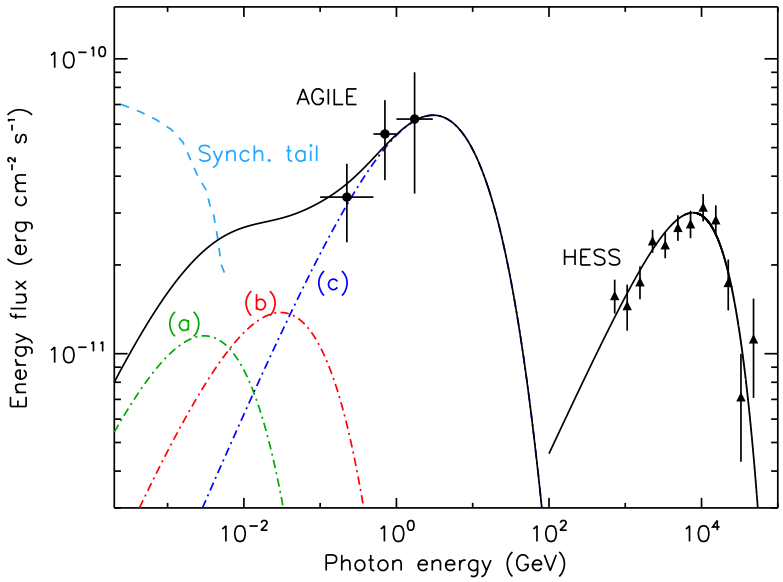

Figure 6.3 Gamma-ray high-energy and very-high-energy νF_ν spectrum of the Vela X PWN. *HESS* data fit an IC process (scattering on CMBR) related to electron power-law index 2.0 with a break at 67 TeV and a total energy content of 2.2×10^{45} erg [14]. *AGILE* data are compatible with IC emission from the additional electron component, well reproducing the observed total radio spectrum ($E_{tot} = 4 \times 10^{48}$ erg), assuming the same field strength (~ 5 μG) as required by the TeV spectral break. Unlike the TeV IC emission, GeV IC scattering is within the Thompson limit. Thus, in addition to the CMBR component (photon density $n_{ph} = 0.25$ eV cm^{-3}, photon energy $E_{ph} = 10^{-3}$ eV), also FIR ($n_{ph} = 0.3$ eV cm^{-3}, $E_{ph} = 10^{-2}$ eV) and starlight ($n_{ph} = 1.4$ eV cm^{-3}, $E_{ph} = 1$ eV) photon fields can significantly contribute to the high-energy IC counterpart of the radio spectrum fitting *AGILE* data [dot-dashed lines: CMBR (a), FIR (b), starlight (c); thick line: total IC spectrum].

On the basis of the available count statistics, we performed a first estimate of the spectrum by sampling the flux in the three energy bands (0.1 to 0.5 GeV, 0.5 to 1 GeV, and 1 to 3 GeV; Figure 6.3) where the source is clearly detected. A power-law fit yields a photon index $\alpha = -1.67 \pm 0.25$. The *AGILE* spectral points are a factor of ~ 2 below the previous *EGRET* upper limits [60] and well above the extrapolation of the *HESS* spectral energy distribution νF_ν to lower energies. The

PWN gamma-ray luminosity in the 0.1- to 10-GeV band, for a distance of ~ 290 pc [65, 44], is $4^{+4}_{-2} \times 10^{33}$ erg s^{-1}, corresponding to $\sim 10^{-3}\dot{E}_{rot}$ (where $\dot{E}_{rot}$ is the spin-down luminosity of the pulsar). Such a luminosity is slightly higher than at VHE energies (9.9×10^{32} erg s^{-1}).

6.4.2 The Origin of the Emission

In the frame of leptonic models, the *AGILE* measurements are not consistent with a simple multi-wavelength spectral energy distribution involving a single electron population. The *AGILE* spectral points are one order of magnitude above the fluxes expected from the electron population simultaneously fitting synchrotron X-ray emission (peaking at ~ 1 keV) and IC TeV emission [14, 131].

Additional electron populations should be invoked to explain the observed GeV fluxes. This is not surprising in view of the complex morphology of the PWN seen in radio and X-rays, where different sites and features of non-thermal emission are present: the anisotropic pulsar wind and non homogeneous SNR reverse shock pressure produce different particle populations within the shocked wind. In particular, assuming the same magnetic field (5μG) reproducing the TeV spectral break, the radio synchrotron emitting electrons observed in the Vela X structure [21] may be responsible for the IC bump in the GeV band arising from scattering on CMBR and galactic and starlight photon fields, as predicted by [61]. Indeed, the position where *AGILE* sees the maximum brightness ($RA = 08h35m$, $Dec = -45^{\circ}44'$) is also roughly where the 8.4-GHz radio emission is brightest (). *AGILE* data are compatible with the IC parameters modeled by [61] (electron spectral index 1.78 and maximum energy ~ 20 GeV), although our measurements could suggest a higher contribution from IC photon seeds. In particular, assuming a starlight energy density of 1.4 eV cm^{-3} and a mean temperature of ~ 2300 K (see http://www.iasf-milano.inaf.it/giuliani/public/thesis/node10.html), we obtain a good description of the *AGILE* data (Figure 6.3).

The *AGILE* measurements would be incompatible with the scenario of nucleonic gamma-ray production in the Vela TeV nebula in the frame of a single primary electron population. These models predict very faint GeV emission ($< 10^{30}$ erg s^{-1}) even when including synchrotron and IC emission from primary and secondary electrons produced by the inelastic nuclear scattering [106]. On the other hand, the proposed additional electron component scenario described above leaves room for uncorrelated GeV-TeV emission, although the comprehensive

multi-wavelength two-component leptonic model (providing strong IC emission on a relatively dense photon field) seems to disfavor dominant nucleonic gamma-ray production. In fact, it has been found that the thermal particle density at the head of the cocoon, where bright VHE gamma-ray emission was found, is lower than that required by hadronic models by a factor of 6 [131].

The radio-emitting region mentioned above appears to be larger ($\sim 2^\circ \times 3^\circ$) than the *AGILE* nebula, possibly indicating that IC cooling in the GeV domain is important. However, the actual physical size of the GeV nebula could be larger than what we are able to resolve with the available photon statistics, because of the strong galactic gamma-ray emission affecting MeV-GeV energy bands. Instead, the *AGILE* nebula is similar in shape to the *HESS* nebula, which may suggest that the core of HE and VHE emission is produced in the same projected region of Vela X, even if different electron populations are involved. Indeed, different spots of bright radio emission [84], possibly associated to electrons injected at different stages of pulsar evolution, are embedded within the poorly resolved HE and VHE emission regions.

Fermi-LAT Observations

A subsequent work from *Fermi*-LAT [5] confirmed the emission from Vela X at GeV energies. The gamma-ray emission detected by *Fermi*-LAT lies within the Vela SNR, in the $2^\circ \times 3^\circ$ area south of the pulsar known as Vela-X. The *Fermi*-LAT flux is significantly spatially extended with a best-fit radius of $0^\circ.88 \pm 0^\circ.12$ for an assumed radially symmetric uniform disk. The 200 MeV to 20 GeV *Fermi*-LAT spectrum of this source is well described by a power law with a spectral index of $2.41 \pm 0.09 \pm 0.15$ and integral flux above 100 MeV of $4.73 \pm 0.63 \pm 1.32 \times 10^{-7}$ cm^{-2} s^{-1}. The first errors represent the statistical error on the fit parameters, while the second ones are the systematic uncertainties.

The *Fermi*-LAT spectrum and the improved flux estimates for the radio and X-ray emission from the two components of their SED disfavors the hadronic scenario. They require a three-component injection (one hadron and two lepton) in this case, along with a quite high magnetic eld in the cocoon in order to suppress IC scattering of X-ray emitting electrons from providing the dominant source of VHE gamma rays. Their SED also strongly supports the two-component leptonic model as predicted by [61].

6.4.3 The PWNe as Unidentified Gamma-Ray Sources or Unresolved Gamma-Ray Background

High-energy PWN emissions are thought to be a common phenomenon associated with young and energetic pulsars [153] because the IC emission of these PWNe arises mostly from scattering on CMBR and starlight fields, with no special environmental requirements. On the other hand, PWN emissions are expected to be much weaker than pulsed emission from the associated neutron star, especially in the GeV domain where most of the pulsars spin-down energy is funneled. Indeed, despite a PWN gamma-ray yield of $L_{\gamma}^{PWN} \approx 10^{-3} \times \dot{E}_{rot}$, to be compared with the typical gamma-ray pulsed luminosity of $L_{\gamma}^{pulsed} \approx 10^{-2} - 10^{-1} \times \dot{E}_{rot}$, our *AGILE* observations shows that 10^4-year old PWNe can match the sensitivities of current GeV instruments.

Because the gamma-ray luminosity of the PWN is only a small fraction of the beamed emission from the neutron star, the PWN component is difficult to identify in weaker gamma-ray pulsars, although it could account for a substantial part of the observed off-pulse flux. However, if the beamed emission does not intersect the line of sight to the observer, the PWN component, unhindered by the stronger pulsed emission, could be detectable. Energetic pulsars (e.g., $\dot{E}_{rot} \approx 10^{37}$ erg s^{-1}) can power PWNe with gamma-ray luminosities matching the flux ($\sim 10^{-8}$ to 10^{-7} photons cm^{-2} s^{-1}; $E > 100$ MeV) of a class of unidentified *EGRET* sources [94], as well as a subset of those detected by *AGILE* and *Fermi*-LAT [179, 213], when placed within few kiloparsecs. The roughly isotropic emission from such undisturbed PWNe would not yield pulsations, and, as a class, they could contribute to the population of galactic unidentified sources still awaiting multi-wavelength association [171, 57].

6.5 A Flux Enhancement from the Crab Region

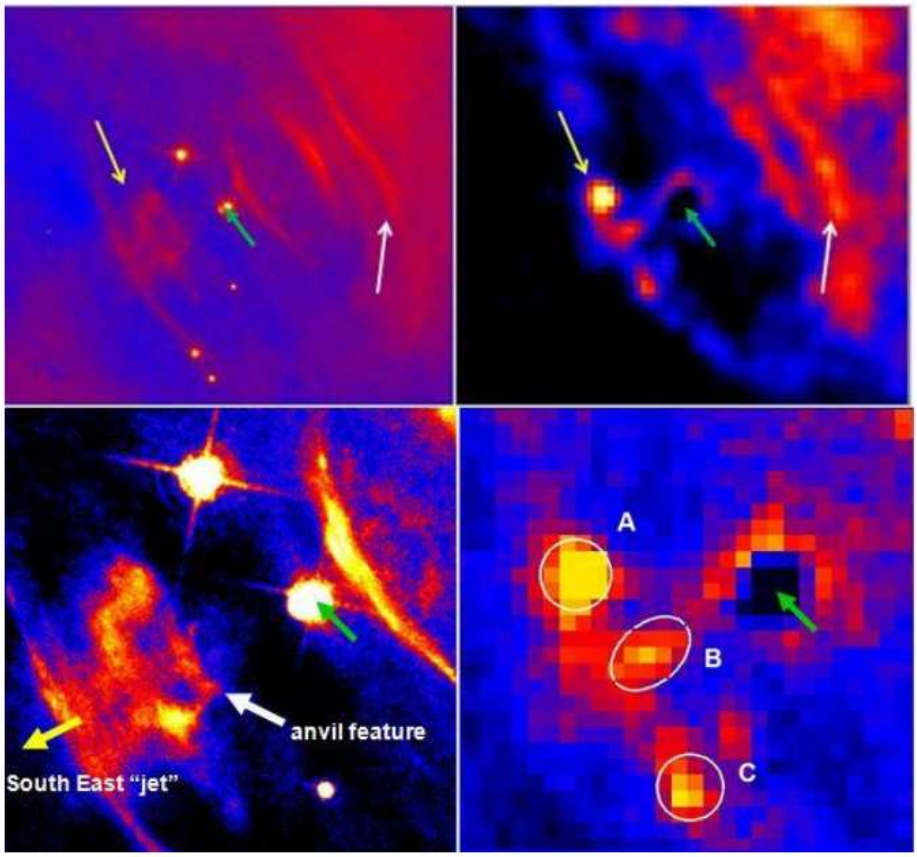

Figure 6.4 Hubble Space Telescope (HST) and Chandra imaging of the Crab Nebula following the September 2010 gamma-ray flare. (Top left panel:) optical image of the inner nebula region. The pulsar position is marked with a green arrow in all panels. White arrows in all panels mark interesting features compared to archival data. (Top right panel:) the same region imaged by the Chandra Observatory ACIS instrument on September 28, 2010 in the energy range 0.5-8 keV. The pulsar does not show in this map and below because of pileup. (Bottom left panel:) zoom of the HST image showing the nebular inner region, and the details of the anvil feature showing a ring-like structure at the base of the South-East jet off the pulsar. Knot 1 at $0''.6$ South-East from the pulsar is saturated at the pulsar position. Terminology is from [99]. (Bottom right panel:) zoom of the Chandra image, showing the X-ray brightening of the anvil region and the correspondence with the optical image.

The Crab Nebula is the relic of the stellar explosion recorded by Chinese astronomers in 1054 C.E.. It is located at a distance of 2 kpc from Earth, and is energized by the powerful Crab pulsar of spin-down luminosity $L_{PSR} = 5 \times 10^{38}$ erg s^{-1}. Optical and X-ray images of the inner nebula show features such as wisps (composing a torus-shaped structure), knots and the anvil (positioned along the South-East jet originating from the pulsar, and aligned with its rotation axis).

Wisps, some of the knots, and the anvil are known to brighten and fade over weeks or months. The Crab Nebula X-ray continuum and gamma-rays up to ~ 100 MeV energies are modeled by synchrotron radiation, and emission from GeV to TeV energies as inverse Compton radiation by accelerated electrons scattering the Cosmic Microwave Background (CMB) and nebular photons.

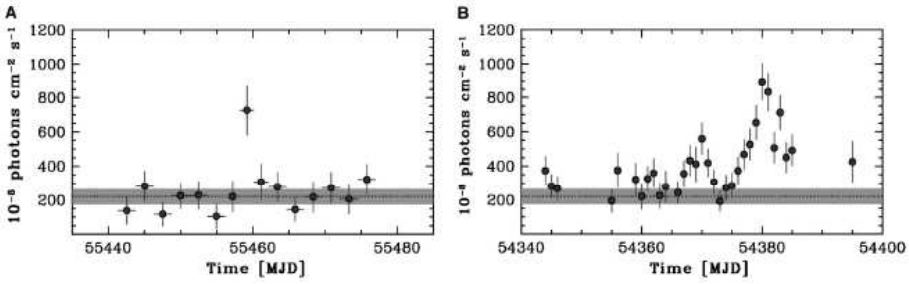

Figure 6.5 Crab Nebula light curves of the total flux detected by *AGILE* in the energy range 100 MeV - 5 GeV during the gamma-ray flaring periods in 2007 and 2010 (units of 10^{-8} ph cm^{-2} s^{-1}). (Top panel:) the spinning AGILE photon flux light curve during the period September 2 - October 8, 2010. Time bins are 2.5 days except near the flare peak (2-day binning). Errors are 1σ. The dotted line and band marked in grey color show the average Crab flux and the 3 σ uncertainty range. (Bottom panel:) The *AGILE* light curve during the period September 27 October 12, 2007 (1-day binning) with the satellite in pointing mode. Errors are 1σ. The dotted line and band marked in grey color show the average Crab flux and the 3σ uncertainty range.

AGILE observed the Crab Nebula several times both in pointing mode from mid-2007/mid-2009, and in spinning mode starting in November 2009. With the exception of a remarkable episode in October, 2007 (see below) we obtain, during standard non-active states, an average (pulsar +nebula) flux value of $F_\gamma = (2.2 \pm 0.1) \times 10^{-6}$ ph cm^{-2} s^{-1} in the range 100 MeV - 5 GeV, for an average photon index $\alpha = 2.13 \pm 0.07$. During routine monitoring in spinning mode in September 2010, a strong and unexpected gamma-ray flare from the direction of the Crab Nebula was discovered [210] by *AGILE* above 100 MeV. The flare reached its peak during 19-21 September 2010 with a 2-day flux of $F_{\gamma,p1} = (7.2 \pm 1.4) \times 10^{-6}$ ph cm^{-2} s^{-1} ($\alpha = 2.03 \pm 0.18$) for a 4.8σ detection above the average flux. It subsequently decayed within 2-3 days to normal average values (Figure 6.5, left panel). This flare was independently confirmed by *Fermi*-LAT [41], and different groups obtained multifrequency data in the following days (see next Section).

Recognizing the importance of this event was facilitated by a previous *AGILE* detection with similar characteristics (see Section 6.5.2).

6.5.1 The Flare Across the Electromagnetic Spectrum

Optical and X-ray imaging shows no additional source in the Crab region during and after the flare. We note that the flaring GeV spectrum is substantially harder than the standard nebular emission [59, 27, 159]. Figure 6.4 shows the high-resolution (arcsecond) optical and X-ray images of the nebula obtained 1-2 weeks after the flare by the Chandra Telescope and the Hubble Space Telescope (HST). A few nebular brightened features are noticeable in both images. The first one is the optical and X-ray anvil feature close to the base of the pulsar jet, a primary site of shocked particle acceleration in the inner nebula [100, 99]. Another brightened feature is at a larger distance from the pulsar, and appears as an elongated striation in both the HST and Chandra images.

6.5.2 Similar Episodes in the Past and Later On

AGILE detected indeed another remarkable flare from the Crab in October 2007. This flare has similar spectral characteristics to the September 2010 episode. It extended for ~ 2 weeks and showed an interesting time sub-structure (Figure 6.5, bottom panel). The peak flux was reached on 7 October 2007 and the 1-day integration value was $F_{\gamma,p2} = (8.9 \pm 1.1) \times 10^{-6}$ ph cm^{-2} s^{-1} ($\alpha = 2.05 \pm 0.13$) for a 6.2 σ detection above the standard flux.

A *Fermi*-LAT reanalysis of their all-time Crab data-set provided another detection of a flare in February 2009 [4], when *AGILE* was not pointing the Anti-Center region. The February flare had a duration of ~ 16 days. The average integral flux above 100 MeV was $F_\gamma = 23.2 \pm 2.9 \times 10^{-7}$ ph cm^{-2} s^{-1}, corresponding to an increase by a factor 3.8 ± 0.5 compared with the average value. This flare had a soft spectrum with a photon index of 4.3 ± 0.3. The spectral slope was still compatible with the average 25-month value within 2σ.

Finally, in April 2011, *Fermi*-LAT and *AGILE* detected an extremely intense and fast gamma-ray flare above 100 MeV from the Crab Nebula, the fourth of the sequence of major gamma-ray flaring events produced by the Crab Nebula in the period 2007/mid-2011. The April 13 - 18 event showed a very rapid flux and spectral evolution: it reached a flux of $F_\gamma = 30 \pm 6 \times 10^{-6}$ ph cm$^-2$ s^{-1} on a 12-hour timescale. Strong flux and spectral variations were detected on a timescale of a few hours during the pre- and post-flare period. Starting on April 11-12 2011 a new gamma-ray flaring episode with substantial emission above 100 MeV was detected by *Fermi*-LAT. The flare developed in the following days with substantial gamma-

ray emission 2-3 times the normal average value ($F_{\gamma,steady} = 2.2 \pm 0.1 \times 10^{-6}$ ph cm^{-2} s^{-1}) until it reached on April 16, 2011 the unprecedented high value of $F_\gamma = 20 \pm 4 \times 10^{-6}$ ph cm^{-2} s^{-1} on a 24-hour timescale.

6.5.3 The Possible Origins of the Flare

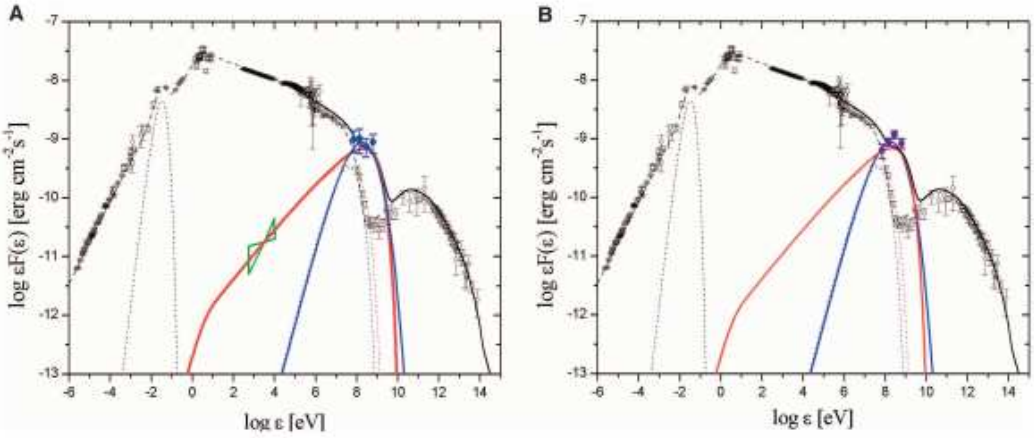

Figure 6.6 SED of the Crab Nebula and the flaring gamma-ray episodes (the pulsar signal has been subtracted). Open black symbols: Crab Nebula emission in the steady state. The dashed curve shows our modeling of the steady state. The solid black curve shows our flare modeling for energies above 105 eV. Dotted black curve: nebular IR emission [98]. (**A**) blue filled symbols: spectral *AGILE* gamma-ray flare data integrated over 2 days (September 19-21, 2010, MJD 55458.5-55460.5). Errors are 1σ. Solid red and blue curves show the 2-day averaged spectral models based on synchrotron radiation from relativistic $e^+ - e^-$ impulsively accelerated in a shock region of size $L \leq 10^{16}$ cm . Dotted curves show the spectra evolved by synchrotron cooling 3 days after the flare. (**B**) violet symbols: spectral *AGILE* gamma-ray data during the October 7-9, 2007 flare (MJD 54380.5-54382.5). Errors are 1σ. The black, blue and red curves are those of the September 2010 flare, and are shown here as a reference to compare the two spectra.

For both the October 2007 and September 2010 events there was no sign of variation of the pulsar gamma-ray signal during and after these flares, as independently confirmed for the September-2010 event by gamma-ray (22), radio (23), and X-ray analyses. Both flares thus seem to be attributable to unpulsed relativistic shock emission originating in the nebula. Important constraints can be derived from the gamma-ray flare luminosity and timescale. The peak isotropic gamma-ray luminosity $L_p \approx 5 \times 10^{35}$ erg s^{-1} implies for e.g. a (3-5)% radiation efficiency, that about (2-3)% of the total spin-down pulsar luminosity was dissipated at the flaring site. This large value suggests that the production region was close to the pulsar. Also the flare rise time ($\sim$ 1 day) favors a compact emission region of

size $L \leq 10^{16}$ cm. The anvil feature is an excellent flare site candidate, also because of its alignment with the relativistic pulsar jet [100, 99, 98] . This region is expected to be dominated by the leptonic current from the polar jets [202, 25].

Gamma-ray flaring from the Crab Nebula provides a unique opportunity to constrain particle acceleration and radiative processes in a nebular environment. Synchrotron emission from a fresh population of shock accelerated electrons/positrons along the pulsar polar jet can explain the flaring emission in the range $0.1 - 10$ GeV. Figure 6.6 shows our flare spectral data and two examples of modeling for different assumptions on the particle populations downstream of the shock (a pure electron-positron relativistic Maxwellian distribution, and a distribution modified by a power-law component). Maxwellian and power-law models predict similar synchrotron radiation fluxes in the GeV band as shown in Figure 6.6. However, if the emission from the anvil feature is related to the gamma-ray flaring, power-law models can explain also the X-ray emission from that region. Fast cooling of the highest energy particles drastically decreases the GeV flux within a few days, as observed in both the September 2010 and October 2007 flares.

These gamma-ray flares test and constrain theoretical models applicable to pure pair plasmas or to distributions modified by the presence of ions that resonantly accelerate pairs by magnetosonic waves [202, 25, 80]. The acceleration rate resulting from local wave absorption at the relativistic (electron or ion) cyclotron frequency and from hydrodynamical constraints is determined to be $R_{acc} \sim (\text{day})^{-1}$, implying a flare region size $L \approx 10^{16}$ cm for a standard downstream sound speed. Furthermore, reconciling the synchrotron cooling timescale $\tau \approx (8 \times 10^8$ sec) $B^{-2}\gamma^{-1}$ (where the magnetic field B is in Gauss, and γ is the particle Lorentz factor) with our observations implies, for a Lorentz factor $\gamma \approx (1-3) \times 10^9$ of electrons irradiating in the GeV range, a local magnetic field $B \approx 10^{-3}$ G that is 3-10 times the nebular average [100, 159]. Both the 2007 and 2010 gamma-ray flares have similar spectral characteristics (Figure 6.6).

6.5.4 Spectral Evolution of the September 2010 Flare

The Crab Nebula X-ray continuum and gamma-rays up to ~ 100 MeV energies are modelled by synchrotron radiation of accelerated particles in an average nebular magnetic field $\vec{B} = 200\mu$G [99, 59, 27, 159]. Emission from GeV to TeV energies is interpreted as inverse Compton radiation by electrons/positrons scattering CMB and nebular soft photons [58, 59, 27, 159].

Three features of the September 2010 event are relevant: (1) the event develops within 3-4 days (whereas the others last about 2 weeks); (2) the gamma-ray rise-time appears to be remarkably short, $\tau \leq 1$ day [209]; (3) the flaring gamma-ray spectrum extends well above the limit for the maximum radiated photon energy (e.g., [15]:

$$E_{\gamma,max} \simeq \frac{9}{4}\alpha^{-1} m_e c^2 \simeq 150\text{MeV} \tag{6.1}$$

where $\alpha = e^2/\hbar c$ is the fine structure constant, c is the speed of light and m_e the mass of the electron. The constraint arises if one assumes equality between the accelerating electric field and the magnetic field at the acceleration site and synchrotron cooling in the co-spatial magnetic field and it applies to the Crab Nebula environment with the exception of this episode [209, 4]. A flare production site in the inner nebula of size $L \leq 10^{16}$ cm is favored by both the peak isotropic gamma-ray luminosity $L_p \approx 5 \times 10^{35}$ erg s^{-1} (which implies for a (3-5)% radiation efficiency that about (2-3)% of the total spin-down pulsar luminosity is dissipated at the flaring site) and by the flare rise-time of ~ 1 day. We noticed that the anvil region (knot-2 and possibly knot-1) in the Crab Nebula [197, 98] is an excellent flare site candidate also because of its alignment with the relativistic pulsar jet [209].

The September 2010 event of the Crab Nebula lasting ~ 4 days is currently the shortest detected gamma-ray flare. An analysis was presented by [224], showing that the flux and spectral evolution of this event are well described by a model characterized by very fast (shorter than ~ 1 day) particle acceleration and by synchrotron cooling in a local magnetic field 5 - 10 times larger than the average nebular value. Both the *AGILE* and *Fermi*-LAT gamma-ray spectral data are consistent with each other within a 4-day timescale. This analysis of the *AGILE* data on a 2-day timescale clearly showed that the emission is peaked at the photon energy $E_{peak} \simeq 800$ MeV, which is almost one order of magnitude larger than the synchrotron burn-off constraint of Equation 6.1. The flaring mechanism in the Crab Nebula is quite remarkable: it accelerates particles to the largest kinetic energies (PeV) associable to a specific astrophysical source and does it within the shortest time ever detected in a nebular environment.

Our results challenge the physical assumptions underlying Equation 6.1 and in particular acceleration models based on slow processes. They show that explanations in terms of Doppler boosting are problematic in light of the measured spectral curvature of the *AGILE* data (Figure 6.6). Even though a theoretical study of possible acceleration mechanisms consistent with the data discussed was beyond

the scope of this work, one can briefly mention some of the difficulties. First-order Fermi acceleration with particles gaining energy by diffusing stochastically back and forth a shock front (e.g., [36, 35, 66]) appears to be too slow and is drastically challenged by our findings. In particular, it is difficult to see how a diffusive shock acceleration mechanism can violate Equation 6.1. A locally enhanced electric field can produce a sort of runaway of kinetic energy gains with an acceleration rate larger than the synchrotron cooling rate. However, despite some attempts and analogies with other astrophysical contexts (e.g., pulsar magnetospheres), it is currently not clear how this mechanism can be implemented in the Crab Nebula. MHD models of the pulsar wind (e.g., [120, 63, 43, 121]), address the turbulence and the limit-cycle behavior of the instabilities. These features may in principle favor substantial local magnetic field enhancements. However, the calculated timescales of these instabilities (e.g., [43]) are several orders of magnitudes longer than what were detected in the Crab Nebula. Shock-drift acceleration [118] tends to occur on a timescale shorter than diffusive processes. However, it is not clear whether the required efficiency can be reached in the flaring Crab Nebula site, and whether $E_{peak} \simeq 800$ MeV can be obtained. Shocks mediated by ions in the pulsar wind that resonantly accelerate pairs by magnetosonic waves [80, 202, 25] are typically slow, and are most likely not applicable in the X-ray and optically enhanced pulsar polar jet regions of [209].

The challenge provided by the Crab Nebula gamma-ray flaring requires a thorough investigation of the mechanisms leading to efficient particle acceleration and to a natural justification of $E_{peak} \simeq 800$ MeV. The issue will be elucidated by future Chandra X-ray and HST optical observations of the inner Crab Nebula that will be carried out in search of the gamma-ray flaring site.

6.5.5 Conclusions

This observation suggests that a common acceleration process produced electron/positron energy distributions with similar physical parameters.

Considering *AGILE* exposure of the Crab Nebula, we estimate that 1-2 strong gamma-ray flares actually occur per year. The Crab Nebula is thus not a standard candle at GeV energies. Significant variations of the Crab Nebula high-energy flux have also been recently reported at X-ray [234] and, possibly, at TeV [16] energies. It remains to be established whether the gamma-ray flares that we report can be attributed to pulsar activity injecting fresh particles in the surroundings, or to major

plasma wave instabilities in the nebular environment.

Bibliography

[1] A. A. Abdo, et al. Detection of the Energetic Pulsar PSR B1509-58 and its Pulsar Wind Nebula in MSH 15-52 Using the Fermi-Large Area Telescope. *ApJ*, 714:927–936, May 2010.

[2] A. A. Abdo, et al. The Vela Pulsar: Results from the First Year of Fermi LAT Observations. *ApJ*, 713:154–165, April 2010.

[3] A. A. Abdo, et al. Search for Gamma-ray Emission from Magnetars with the Fermi Large Area Telescope. *ApJL*, 725:L73–L78, December 2010.

[4] A. A. Abdo, et al. Gamma-Ray Flares from the Crab Nebula. *Science*, 331:739–, February 2011.

[5] A. A. Abdo, et al. Fermi Large Area Telescope Observations of the Vela-X Pulsar Wind Nebula. *ApJ*, 713:146–153, April 2010.

[6] A. A. Abdo, et al. Detection of 16 Gamma-Ray Pulsars Through Blind Frequency Searches Using the Fermi LAT. *Science*, 325:840–, August 2009.

[7] A. A. Abdo, et al. The First Fermi Large Area Telescope Catalog of Gamma-ray Pulsars. *ApJS*, 187:460–494, April 2010.

[8] A. A. Abdo, et al. Fermi Large Area Telescope Observations of the Crab Pulsar And Nebula. *ApJ*, 708:1254–1267, January 2010.

[9] A. A. Abdo, et al. A population of gamma-ray emitting globular clusters seen with the Fermi Large Area Telescope. *A&A*, 524:A75+, December 2010.

[10] A. A. Abdo, et al. Fermi Large Area Telescope Observations of Gamma-ray Pulsars PSR J1057-5226, J1709-4429, and J1952+3252. *ApJ*, 720:26–40, September 2010.

[11] S. L. Adler. Photon splitting and photon dispersion in a strong magnetic field. *Annals of Physics*, 67:599–647, 1971.

[12] S. L. Adler, J. N. Bahcall, C. G. Callan, and M. N. Rosenbluth. Photon Splitting in a Strong Magnetic Field. *Physical Review Letters*, 25:1061–1065, October 1970.

[13] F. Aharonian, et al. Discovery of extended VHE gamma-ray emission from the asymmetric pulsar wind nebula in MSH 15-52 with HESS. *A&A*, 435:L17–L20, May 2005.

[14] F. Aharonian, et al. First detection of a VHE gamma-ray spectral maximum from a cosmic source: HESS discovery of the Vela X nebula. *A&A*, 448:L43–L47, March 2006.

[15] F. A. Aharonian, et al. High-energy particle acceleration in the shell of a supernova remnant. *Nature*, 432:75–77, November 2004.

[16] G. Aielli, et al. Enhanced TeV gamma ray flux from the Crab Nebula observed. *The Astronomer's Telegram*, 2921:1–+, October 2010.

[17] J. Albert, et al. VHE γ-Ray Observation of the Crab Nebula and its Pulsar with the MAGIC Telescope. *ApJ*, 674:1037–1055, February 2008.

[18] E. Aliu, et al. Observation of Pulsed γ-Rays Above 25 GeV from the Crab Pulsar with MAGIC. *Science*, 322:1221–, November 2008.

[19] M. A. Alpar, P. W. Anderson, D. Pines, and J. Shaham. Vortex creep and the internal temperature of neutron stars. II - VELA pulsar. *ApJ*, 278:791–805, March 1984.

[20] M. A. Alpar, D. Pines, P. W. Anderson, and J. Shaham. Vortex creep and the internal temperature of neutron stars. I - General theory. *ApJ*, 276:325–334, January 1984.

[21] H. Alvarez, J. Aparici, J. May, and P. Reich. The radio spectral index of the Vela supernova remnant. *A&A*, 372:636–643, June 2001.

[22] A. M. Archibald, V. M. Kaspi, M. A. Livingstone, and M. A. McLaughlin. No Detectable Radio Emission from the Magnetar-Like Pulsar in Kes 75. *ApJ*, 688:550–554, November 2008.

[23] J. Arons. Pair creation above pulsar polar caps - Geometrical structure and energetics of slot gaps. *ApJ*, 266:215–241, March 1983.

[24] J. Arons. Pulsars as gamma ray sources. *AAPS*, 120:C49+, November 1996.

[25] J. Arons. Pulsars: Progress, Problems and Prospects. *ArXiv e-prints*, August 2007.

[26] Z. Arzoumanian, et al. Discovery of an Energetic Pulsar Associated with SNR G76.9+1.0. *ApJ*, 739:39–+, September 2011.

[27] A. M. Atoyan and F. A. Aharonian. On the mechanisms of gamma radiation in the Crab Nebula. *MNRAS*, 278:525–541, January 1996.

[28] W. B. Atwood, et al. The Large Area Telescope on the Fermi Gamma-Ray Space Telescope Mission. *ApJ*, 697:1071–1102, June 2009.

[29] W. B. Atwood, M. Ziegler, R. P. Johnson, and B. M. Baughman. A Time-differencing Technique for Detecting Radio-quiet Gamma-Ray Pulsars. *ApJL*, 652:L49–L52, November 2006.

[30] X.-N. Bai and A. Spitkovsky. Modeling of Gamma-ray Pulsar Light Curves Using the Force-free Magnetic Field. *ApJ*, 715:1282–1301, June 2010.

[31] M. G. Baring. High-energy emission from pulsars: the polar cap scenario. *Advances in Space Research*, 33:552–560, 2004.

[32] M. G. Baring and A. K. Harding. Photon Splitting and Pair Creation in Highly Magnetized Pulsars. *ApJ*, 547:929–948, February 2001.

[33] R. H. Becker and D. J. Helfand. New radio observations of the composite supernova remnant G29.7-0.3. *ApJ*, 283:154–157, August 1984.

[34] W. Becker and G. G. Pavlov. The Milky Way - Pulsars and Isolated Neutron Stars. *ArXiv Astrophysics e-prints*, August 2002.

[35] A. R. Bell. The acceleration of cosmic rays in shock fronts. I. *MNRAS*, 182:147–156, January 1978.

[36] R. D. Blandford and J. P. Ostriker. Particle acceleration by astrophysical shocks. *ApJL*, 221:L29–L32, April 1978.

[37] J. M. Blondin, R. A. Chevalier, and D. M. Frierson. Pulsar Wind Nebulae in Evolved Supernova Remnants. *ApJ*, 563:806–815, December 2001.

[38] S. V. Bogovalov. On the physics of cold MHD winds from oblique rotators. *A&A*, 349:1017–1026, September 1999.

[39] P. E. Boynton, et al. Optical Timing of the Crab Pulsar, NP 0532. *ApJ*, 175:217–+, July 1972.

[40] S. Buchner and C. Flanagan. Glitches in the Vela Pulsar. In C. Bassa, Z. Wang, A. Cumming, & V. M. Kaspi, editor, *40 Years of Pulsars: Millisecond Pulsars, Magnetars and More*, volume 983 of *American Institute of Physics Conference Series*, pages 145–147, February 2008.

[41] R. Buehler, F. D'Ammando, and E. Hays. Fermi LAT confirmation of enhanced gamma-ray emission from the Crab Nebula region. *The Astronomer's Telegram*, 2861:1–+, September 2010.

[42] M. Burgay, et al. An increased estimate of the merger rate of double neutron stars from observations of a highly relativistic system. *Nature*, 426:531–533, December 2003.

[43] N. F. Camus, S. S. Komissarov, N. Bucciantini, and P. A. Hughes. Observations of 'wisps' in magnetohydrodynamic simulations of the Crab Nebula. *MNRAS*, 400:1241–1246, December 2009.

[44] P. A. Caraveo, A. De Luca, R. P. Mignani, and G. F. Bignami. The Distance to the Vela Pulsar Gauged with Hubble Space Telescope Parallax Observations. *ApJ*, 561:930–937, November 2001.

[45] K. Chen and M. Ruderman. Pulsar death lines and death valley. *ApJ*, 402:264–270, January 1993.

[46] A. F. Cheng and M. A. Ruderman. Particle acceleration and radio emission above pulsar polar caps. *ApJ*, 235:576–586, January 1980.

[47] K. S. Cheng, C. Ho, and M. Ruderman. Energetic radiation from rapidly spinning pulsars. I - Outer magnetosphere gaps. II - VELA and Crab. *ApJ*, 300:500–539, January 1986.

[48] I. Cognard and D. C. Backer. A Microglitch in the Millisecond Pulsar PSR B1821-24 in M28. *ApJL*, 612:L125–L127, September 2004.

[49] R. H. Cohen, B. Coppi, and A. Treves. Magnetic Configuration in the Neighborhood of a Collapsed Star. *ApJ*, 179:269–276, January 1973.

[50] R. H. Cohen and A. Treves. Angular Momentum and Energy Loss of a Compact Star Rotating in a Thermal Plasma. *A&A*, 20:305–+, August 1972.

[51] J. M. Cordes and D. J. Helfand. Pulsar timing. III - Timing noise of 50 pulsars. *ApJ*, 239:640–650, July 1980.

[52] J. M. Cordes and T. J. W. Lazio. NE2001.I. A New Model for the Galactic Distribution of Free Electrons and its Fluctuations. *eprint (astro-ph/0207156)*, July 2002.

[53] F. Crawford, R. N. Manchester, and V. M. Kaspi. Polarization Properties of Nine Southern Radio Pulsars. *AJ*, 122:2001–2007, October 2001.

[54] G. Cusumano, V. L. Parola, P. Romano, D. N. Burrows, and J. M. Gelbord. Swift/XRT observation of the Crab Nebula after the gamma-ray flare observed on April 11, 2011. *The Astronomer's Telegram*, 3279:1–+, April 2011.

[55] J. K. Daugherty and A. K. Harding. Polar CAP models of gamma-ray pulsars: Emision from single poles of nearly aligned rotators. *ApJ*, 429:325–330, July 1994.

[56] J. K. Daugherty and A. K. Harding. Gamma-Ray Pulsars: Emission from Extended Polar CAP Cascades. *ApJ*, 458:278–+, February 1996.

[57] O. C. de Jager. Lower Limits on Pulsar Pair Production Multiplicities from H.E.S.S. Observations of Pulsar Wind Nebulae. *ApJ*, 658:1177–1182, April 2007.

[58] O. C. de Jager and A. K. Harding. The expected high-energy to ultra-high-energy gamma-ray spectrum of the Crab Nebula. *ApJ*, 396:161–172, September 1992.

[59] O. C. de Jager, et al. Gamma-Ray Observations of the Crab Nebula: A Study of the Synchro-Compton Spectrum. *ApJ*, 457:253–+, January 1996.

[60] O. C. De Jager, A. K. Harding, P. Sreekumar, and M. S. Strickman. OSSE and EGRET Observations of the Crab and Vela Supernova Remnants. In *International Cosmic Ray Conference*, volume 2 of *International Cosmic Ray Conference*, pages 174–+, 1995.

[61] O. C. de Jager, P. O. Slane, and S. LaMassa. Probing the Radio to X-Ray Connection of the Vela X Pulsar Wind Nebula with Fermi LAT and H.E.S.S. *ApJL*, 689:L125–L128, December 2008.

[62] A. De Luca, P. A. Caraveo, S. Mereghetti, M. Negroni, and G. F. Bignami. On the Polar Caps of the Three Musketeers. *ApJ*, 623:1051–1069, April 2005.

[63] L. Del Zanna, E. Amato, and N. Bucciantini. Axially symmetric relativistic MHD simulations of Pulsar Wind Nebulae in Supernova Remnants. On the origin of torus and jet-like features. *A&A*, 421:1063–1073, July 2004.

[64] A. J. Deutsch. The electromagnetic field of an idealized star in rigid rotation in vacuo. *Annales d'Astrophysique*, 18:1–+, January 1955.

[65] R. Dodson, D. Legge, J. E. Reynolds, and P. M. McCulloch. The Vela Pulsar's Proper Motion and Parallax Derived from VLBI Observations. *ApJ*, 596:1137–1141, October 2003.

[66] L. O. Drury. An introduction to the theory of diffusive shock acceleration of energetic particles in tenuous plasmas. *Reports on Progress in Physics*, 46:973–1027, August 1983.

[67] Y.-J. Du, G. J. Qiao, J. L. Han, K. J. Lee, and R. X. Xu. The annular gap model for gamma-ray emission from young and millis econd pulsars. *ArXiv e-prints*, April 2010.

[68] K. S. Dwarakanath. Low-frequency observations of the VELA supernova remnant and their implications. *Journal of Astrophysics and Astronomy*, 12:199–211, September 1991.

[69] J. Dyks and B. Rudak. Two-Pole Caustic Model for High-Energy Light Curves of Pulsars. *ApJ*, 598:1201–1206, December 2003.

[70] R. T. Edwards, G. B. Hobbs, and R. N. Manchester. TEMPO2, a new pulsar timing package - II. The timing model and precision estimates. *MNRAS*, 372:1549–1574, November 2006.

[71] R. Enomoto, et al. A Search for Sub-TeV Gamma Rays from the Vela Pulsar Region with CANGAROO-III. *ApJ*, 638:397–408, February 2006.

[72] C. M. Espinoza, A. Lyne, M. Kramer, R. N. Manchester, and V. Kaspi. The braking index of PSR J1734-3333 and the magnetar population. *ArXiv e-prints*, September 2011.

[73] C. M. Espinoza, A. G. Lyne, B. W. Stappers, and M. Kramer. A study of 315 glitches in the rotation of 102 pulsars. *MNRAS*, 414:1679–1704, June 2011.

[74] G. Fasano and A. Franceschini. A multidimensional version of the Kolmogorov-Smirnov test. *MNRAS*, 225:155–170, March 1987.

[75] C. E. Fichtel, et al. High-energy gamma-ray results from the second small astronomy satellite. *ApJ*, 198:163–182, May 1975.

[76] J. M. Fierro. *Observ. of Spin-Powered pulsars with EGRET*. PhD thesis, Thesis, Stanford University, (1995), January 1995.

[77] D. A. Frail, M. F. Bietenholz, C. B. Markwardt, and H. Oegelman. A Radio/X-Ray Comparison of the VELA X Region. *ApJ*, 475:224–+, January 1997.

[78] B. M. Gaensler, et al. Chandra Imaging of the X-Ray Nebula Powered by Pulsar B1509-58. *ApJ*, 569:878–893, April 2002.

[79] B. M. Gaensler, K. T. S. Brazier, R. N. Manchester, S. Johnston, and A. J. Green. SNR G320.4-01.2 and PSR B1509-58: new radio observations of a complex interacting system. *MNRAS*, 305:724–736, May 1999.

[80] Y. A. Gallant and J. Arons. Structure of relativistic shocks in pulsar winds: A model of the wisps in the Crab Nebula. *ApJ*, 435:230–260, November 1994.

[81] F. P. Gavriil,et al. Magnetar-Like Emission from the Young Pulsar in Kes 75. *Science*, 319:1802–, March 2008.

[82] P. L. Gonthier, S. A. Story, B. D. Clow, and A. K. Harding. Population statistics study of radio and gamma-ray pulsars in the Galactic plane. *APSS*, 309:245–251, June 2007.

[83] E. V. Gotthelf, G. Vasisht, M. Boylan-Kolchin, and K. Torii. A 700 Year-old Pulsar in the Supernova Remnant Kesteven 75. *ApJL*, 542:L37–L40, October 2000.

[84] A. S. Hales, et al. Vela X at 31 GHz. *ApJ*, 613:977–985, October 2004.

[85] J. P. Halpern, et al. PSR J2229+6114: Discovery of an Energetic Young Pulsar in the Error Box of the EGRET Source 3EG J2227+6122. *ApJL*, 552:L125–L128, May 2001.

[86] J. P. Halpern and E. V. Gotthelf. Two Magnetar Candidates in HESS Supernova Remnants. *ApJ, in press, preprint (arXiv:astro-ph/0912.4985)*, December 2009.

[87] J. P. Halpern, E. V. Gotthelf, J. Reynolds, S. M. Ransom, and F. Camilo. Outburst of the 2 s Anomalous X-Ray Pulsar 1E 1547.0-5408. *ApJ*, 676:1178–1183, April 2008.

[88] J. P. Halpern and S. S. Holt. Discovery of soft X-ray pulsations from the gamma-ray source Geminga. *Nature*, 357:222–224, May 1992.

[89] A. K. Harding. Pulsar gamma-rays - Spectra, luminosities, and efficiencies. *ApJ*, 245:267–273, April 1981.

[90] A. K. Harding, M. G. Baring, and P. L. Gonthier. Photon-splitting Cascades in Gamma-Ray Pulsars and the Spectrum of PSR 1509-58. *ApJ*, 476:246–+, February 1997.

[91] A. K. Harding, A. G. Muslimov, and B. Zhang. Regimes of Pulsar Pair Formation and Particle Energetics. *ApJ*, 576:366–375, September 2002.

[92] A. K. Harding, V. V. Usov, and A. G. Muslimov. High-Energy Emission from Millisecond Pulsars. *ApJ*, 622:531–543, March 2005.

[93] J. W. Hartman, D. Bhattacharya, R. Wijers, and F. Verbunt. A study of the evolution of radio pulsars through improved population synthesis. *A&A*, 322:477–488, June 1997.

[94] R. C. Hartman, et al. The Third EGRET Catalog of High-Energy Gamma-Ray Sources. *ApJS*, 123:79–202, July 1999.

[95] C. O. Heinke. Swift imaging shows no evidence for active AGN near Crab. *The Astronomer's Telegram*, 2868:1–+, September 2010.

[96] D. J. Helfand, E. V. Gotthelf, and J. P. Halpern. Vela Pulsar and Its Synchrotron Nebula. *ApJ*, 556:380–391, July 2001.

[97] W. Hermsen, et al. Observation of the millisecond pulsar PSR J0218+4232 by EGRET. In M. L. McConnell & J. M. Ryan, editor, *American Institute of Physics Conference Series*, volume 510 of *American Institute of Physics Conference Series*, pages 257–261, April 2000.

[98] J. J. Hester. The Crab Nebula: An Astrophysical Chimera. *ARAA*, 46:127–155, September 2008.

[99] J. J. Hester, et al. Hubble Space Telescope and Chandra Monitoring of the Crab Synchrotron Nebula. *ApJL*, 577:L49–L52, September 2002.

[100] J. J. Hester, et al. WFPC2 Studies of the Crab Nebula. I. HST and ROSAT Imaging of the Synchrotron Nebula. *ApJ*, 448:240–+, July 1995.

[101] A. Hewish, S.J. Bell, J.D. Pilkington, P.F. Scott, and R.A. Collins. Observation of a Rapidly Pulsating Radio Source. *Nature*, 217:709, 1968.

[102] G. Hobbs, A. G. Lyne, and M. Kramer. An analysis of the timing irregularities for 366 pulsars. *MNRAS*, 402:1027–1048, February 2010.

[103] G. Hobbs, A. G. Lyne, M. Kramer, C. E. Martin, and C. Jordan. Long-term timing observations of 374 pulsars. *MNRAS*, 353:1311–1344, October 2004.

[104] G. B. Hobbs, R. T. Edwards, and R. N. Manchester. TEMPO2, a new pulsar-timing package - I. An overview. *MNRAS*, 369:655–672, June 2006.

[105] N. J. Holloway. Angular momentum and energy loss from pulsars. *MNRAS*, 181:9P–12P, October 1977.

[106] D. Horns, F. Aharonian, A. Santangelo, A. I. D. Hoffmann, and C. Masterson. Nucleonic gamma-ray production in ¡ASTROBJ¿Vela X¡/ASTROBJ¿. *A&A*, 451:L51–L54, June 2006.

[107] A. Iyudin, et al. Detection of the COS-B/EGRET source GRO J2227+61. In *International Cosmic Ray Conference*, volume 3 of *International Cosmic Ray Conference*, pages 89–+, 1997.

[108] F. James and M. Roos. Minuit - a system for function minimization and analysis of the parameter errors and correlations. *Computer Physics Communications*, 10:343–367, December 1975.

[109] S. Johnston, et al. PSR 1259-63 - A binary radio pulsar with a Be star companion. *ApJL*, 387:L37–L41, March 1992.

[110] G. Kanbach. Gamma radiation from the Crab and VELA pulsars. In C. E. Fichtel, S. D. Hunter, P. Sreekumar, & F. W. Stecker, editor, *NASA Conference Publication*, volume 3071 of *NASA Conference Publication*, pages 101–113, May 1990.

[111] G. Kanbach. Gamma-Ray Pulsars. In W. Becker, H. Lesch, & J. Trümper, editor, *Neutron Stars, Pulsars, and Supernova Remnants*, pages 91–+, 2002.

[112] G. Kanbach, et al. EGRET observations of the VELA pulsar, PSR0833-45. *A&A*, 289:855–867, September 1994.

[113] V. M. Kaspi. Grand unification of neutron stars. *Proceedings of the National Academy of Science*, 107:7147–7152, April 2010.

[114] V. M. Kaspi, J. R. Lackey, and D. Chakrabarty. A Glitch in an Anomalous X-Ray Pulsar. *ApJL*, 537:L31–L34, July 2000.

[115] V. M. Kaspi, J. H. Taylor, and M. F. Ryba. High-precision timing of millisecond pulsars. 3: Long-term monitoring of PSRs B1855+09 and B1937+21. *ApJ*, 428:713–728, June 1994.

[116] N. Kawai, et al. X-ray and radio pulse phase comparison for PSR 1509 - 58. *ApJL*, 383:L65, December 1991.

[117] M. J. L. Kesteven. A catalogue of galactic radio sources. *Australian Journal of Physics*, 21:369–+, June 1968.

[118] J. G. Kirk, A. W. Guthmann, Y. A. Gallant, and A. Achterberg. Particle Acceleration at Ultrarelativistic Shocks: An Eigenfunction Method. *ApJ*, 542:235–242, October 2000.

[119] J. G. Kirk, O. Skjæraasen, and Y. A. Gallant. Pulsed radiation from neutron star winds. *A&A*, 388:L29–L32, June 2002.

[120] S. S. Komissarov and Y. E. Lyubarsky. Synchrotron nebulae created by anisotropic magnetized pulsar winds. *MNRAS*, 349:779–792, April 2004.

[121] S. S. Komissarov and M. Lyutikov. On the origin of variable gamma-ray emission from the Crab nebula. *MNRAS*, 414:2017–2028, July 2011.

[122] M. Kramer. Pulsars & Magnetars. In *IAU Symposium*, volume 259 of *IAU Symposium*, pages 485–492, April 2009.

[123] M. Kramer, et al. The Parkes Multibeam Pulsar Survey - III. Young pulsars and the discovery and timing of 200 pulsars. *MNRAS*, 342:1299–1324, July 2003.

[124] M. Kramer, et al. Tests of General Relativity from Timing the Double Pulsar. *Science*, 314:97–102, October 2006.

[125] L. Kuiper and W. Hermsen. High-energy characteristics of the schizophrenic pulsar PSR J1846-0258 in Kes 75. Multi-year RXTE and INTEGRAL observations crossing the magnetar-like outburst. *A&A*, 501:1031–1046, July 2009.

[126] L. Kuiper, et al. COMPTEL detection of pulsed gamma -ray emission from PSR B1509-58 up to at least 10 MeV. *A&A*, 351:119–132, November 1999.

[127] L. Kuiper, et al. High-Resolution Spatial and Timing Observations of Millisecond Pulsar PSR J0218+4232 with Chandra. *ApJ*, 577:917–922, October 2002.

[128] L. Kuiper, et al. The likely detection of pulsed high-energy gamma -ray emission from millisecond pulsar PSR J0218+4232. *A&A*, 359:615–626, July 2000.

[129] H. S. Kumar and S. Safi-Harb. Variability of the High Magnetic Field X-Ray Pulsar PSR J1846-0258 Associated with the Supernova Remnant Kes 75 as Revealed by the Chandra X-Ray Observatory. *ApJL*, 678:L43–L46, May 2008.

[130] A. D. Kuzmin. Giant pulses of pulsar radio emission. *APSS*, 308:563–567, April 2007.

[131] S. M. LaMassa, P. O. Slane, and O. C. de Jager. Probing the Nature of the Vela X Cocoon. *ApJL*, 689:L121–L124, December 2008.

[132] M. I. Large, A. E. Vaughan, and B. Y. Mills. A Pulsar Supernova Association? *Nature*, 220:340–341, October 1968.

[133] D. A. Leahy, W. Tian, and Q. D. Wang. Distance Determination to the Crab-Like Pulsar Wind Nebula G54.1+0.3 and the Search for its Supernova Remnant Shell. *AJ*, 136:1477–1481, October 2008.

[134] J. R. Lin and S. N. Zhang. Radio Pulsars as Progenitors of Anomalous X-Ray Pulsars and Soft Gamma-Ray Repeaters: Magnetic Field Evolution through Pulsar Glitches. *ApJL*, 615:L133–L136, November 2004.

[135] M. A. Livingstone, V. M. Kaspi, and F. P. Gavriil. Timing Behavior of the Magnetically Active Rotation-Powered Pulsar in the Supernova Remnant Kesteven 75. *ApJ*, 710:1710–1717, February 2010.

[136] M. A. Livingstone, V. M. Kaspi, F. P. Gavriil, and R. N. Manchester. 21 Years of Timing PSR B1509-58. *ApJ*, 619:1046–1053, February 2005.

[137] M. A. Livingstone, V. M. Kaspi, E. V. Gotthelf, and L. Kuiper. A Braking Index for the Young, High Magnetic Field, Rotation-Powered Pulsar in Kesteven 75. *ApJ*, 647:1286–1292, August 2006.

[138] M. A. Livingstone, C.-Y. Ng, V. M. Kaspi, F. P. Gavriil, and E. V. Gotthelf. Post-outburst Observations of the Magnetically Active Pulsar J1846-0258. A New Braking Index, Increased Timing Noise, and Radiative Recovery. *ApJ*, 730:66–+, April 2011.

[139] M. López Moya, et al. The TeV Crab. In *Polarimetry days in Rome: Crab status, theory and prospects*, 2008.

[140] D. R. Lorimer and M. Kramer. *Handbook of Pulsar Astronomy*. Cambridge, UK: Cambridge University Press, December 2004.

[141] A. G. Lyne. From Crab Pulsar to Magnetar? In F. Camilo & B. M. Gaensler, editor, *Young Neutron Stars and Their Environments*, volume 218 of *IAU Symposium*, pages 257–+, 2004.

[142] A. G. Lyne, et al. A Double-Pulsar System: A Rare Laboratory for Relativistic Gravity and Plasma Physics. *Science*, 303:1153–1157, February 2004.

[143] A. G. Lyne and R. N. Manchester. The shape of pulsar radio beams. *MNRAS*, 234:477–508, October 1988.

[144] A. G. Lyne, S. L. Shemar, and F. G. Smith. Statistical studies of pulsar glitches. *MNRAS*, 315:534–542, July 2000.

[145] M. Lyutikov. On generation of Crab giant pulses. *MNRAS*, 381:1190–1196, November 2007.

[146] MAGIC Collaboration, J. Aleksić, et al. Observations of the Crab pulsar above 25 GeV with the MAGIC I telescope. *ArXiv e-prints*, August 2011.

[147] MAGIC Collaboration, J. Aleksić, et al. Phase-resolved energy spectra of the Crab Pulsar in the range of 50-400 GeV measured with the MAGIC Telescopes. *ArXiv e-prints*, September 2011.

[148] R. N. Manchester, G. B. Hobbs, A. Teoh, and M. Hobbs. The Australia Telescope National Facility Pulsar Catalogue. *AJ*, 129:1993–2006, April 2005.

[149] R. N. Manchester, et al. The Parkes multi-beam pulsar survey - I. Observing and data analysis systems, discovery and timing of 100 pulsars. *MNRAS*, 328:17–35, November 2001.

[150] R. N. Manchester, I. R. Tuohy, and N. Damico. Discovery of radio pulsations from the X-ray pulsar in the supernova remnant G320.4-1.2. *ApJL*, 262:L31–L33, November 1982.

[151] A. Manzali, A. De Luca, and P. A. Caraveo. Phase-resolved Spectroscopy of the Vela Pulsar with XMM-Newton. *ApJ*, 669:570–578, November 2007.

[152] C. B. Markwardt and H. Ögelman. An X-ray jet from the Vela pulsar. *Nature*, 375:40–42, May 1995.

[153] F. Mattana, et al. The Evolution of the γ- and X-Ray Luminosities of Pulsar Wind Nebulae. *ApJ*, 694:12–17, March 2009.

[154] J. R. Mattox, et al. The Likelihood Analysis of EGRET Data. *ApJ*, 461:396–+, April 1996.

[155] S. Matz, et al. The pulsed hard X-ray spectrum of PSR B1509-58. *ApJ*, 434:288–291, October 1994.

[156] V. A. McBride, et al. INTEGRAL detection of the pulsar wind nebula in PSR J1846-0258. *A&A*, 477:249–253, January 2008.

[157] P. M. McCulloch, P. A. Hamilton, D. McConnell, and E. A. King. The VELA glitch of Christmas 1988. *Nature*, 346:822–824, August 1990.

[158] A. Melatos. Spin-down of an oblique rotator with a current-starved outer magnetosphere. *MNRAS*, 288:1049–1059, July 1997.

[159] M. Meyer, D. Horns, and H.-S. Zechlin. The Crab Nebula as a standard candle in very high-energy astrophysics. *A&A*, 523:A2+, November 2010.

[160] T. Mineo, et al. The hard X-ray emission from the complex SNR MSH 15-52 observed by BeppoSAX. *A&A*, 380:695–703, December 2001.

[161] D. A. Moffett and T. H. Hankins. Multifrequency Radio Properties of the Crab Pulsar. In S. Johnston, M. A. Walker, & M. Bailes, editor, *IAU Colloq. 160: Pulsars: Problems and Progress*, volume 105 of *Astronomical Society of the Pacific Conference Series*, pages 283–+, 1996.

[162] T. D. Morton, et al. Observations of X-Rays and Thermal Dust Emission from the Supernova Remnant Kes 75. *ApJ*, 667:219–225, September 2007.

[163] A. G. Muslimov and A. K. Harding. Extended Acceleration in Slot Gaps and Pulsar High-Energy Emission. *ApJ*, 588:430–440, May 2003.

[164] A. G. Muslimov and A. K. Harding. High-Altitude Particle Acceleration and Radiation in Pulsar Slot Gaps. *ApJ*, 606:1143–1153, May 2004.

[165] C.-Y. Ng, P. O. Slane, B. M. Gaensler, and J. P. Hughes. Deep Chandra Observation of the Pulsar Wind Nebula Powered by Pulsar PSR J1846-0258 in the Supernova Remnant Kes 75. *ApJ*, 686:508–519, October 2008.

[166] F. Pacini. Rotating Neutron Stars, Pulsars and Supernova Remnants. *Nature*, 219:145–146, July 1968.

[167] F. Pacini and M. Salvati. Acceleration of Particles in Extended Non-Thermal Sources. *APL*, 15:39–+, October 1973.

[168] D. Parent, et al. Observations of Energetic High Magnetic Field Pulsars with the Fermi Large Area Telescope. *ArXiv e-prints*, September 2011.

[169] J. A. Peacock. Two-dimensional goodness-of-fit testing in astronomy. *MNRAS*, 202:615–627, February 1983.

[170] A. Pellizzoni, et al. A First XMM-Newton Look at the Relativistic Double Pulsar PSR J0737-3039. *ApJL*, 612:L49–L52, September 2004.

[171] A. Pellizzoni, et al. Pulsar Bow-Shocks. In F. A. Aharonian, H. J. Völk, & D. Horns, editor, *High Energy Gamma-Ray Astronomy*, volume 745 of *American Institute of Physics Conference Series*, pages 371–376, February 2005.

[172] A. Pellizzoni, et al. Discovery of New Gamma-Ray Pulsars with AGILE. *ApJL*, 695:L115–L119, April 2009.

[173] A. Pellizzoni, et al. High-Resolution Timing Observations of Spin-Powered Pulsars with the AGILE Gamma-Ray Telescope. *ApJ*, 691:1618–1633, February 2009.

[174] A. Pellizzoni, et al. Detection of Gamma-Ray Emission from the Vela Pulsar Wind Nebula with AGILE. *Science*, 327:663–, February 2010.

[175] R. Perna and J. A. Pons. A Unified Model of the Magnetar and Radio Pulsar Bursting Phenomenology. *ApJL*, 727:L51+, February 2011.

[176] J. Pétri. A unified polar cap/striped wind model for pulsed radio and gamma-ray emission in pulsars. *MNRAS*, 412:1870–1880, April 2011.

[177] M. Pilia, et al. AGILE Observations of the ”Soft” Gamma-ray Pulsar PSR B1509 - 58. *ApJ*, 723:707–712, November 2010.

[178] M. Pilia, A. Treves, A. Pellizzoni, A. Trois, and S. Motta. Observation of Gamma-Ray Emission from PSR J2022+3842. *The Astronomer's Telegram*, 3466:1–+, July 2011.

[179] C. Pittori, et al. First AGILE catalog of high-confidence gamma-ray sources. *A&A*, 506:1563–1574, November 2009.

[180] J. A. Pons and R. Perna. Magnetars vs. high magnetic field pulsars: a theoretical interpretation of the apparent dichotomy. *ArXiv e-prints*, September 2011.

[181] A. Possenti, R. Cerutti, M. Colpi, and S. Mereghetti. Re-examining the X-ray versus spin-down luminosity correlation of rotation powered pulsars. *A&A*, 387:993–1002, June 2002.

[182] V. Radhakrishnan and R. N. Manchester. Detection of a Change of State in the Pulsar PSR 0833-45. *Nature*, 222:228–229, April 1969.

[183] P. V. Ramanamurthy, et al. A Long-Term Study of High-Energy Gamma-Ray Emission from the Vela, Geminga, and Crab Pulsars. *ApJ*, 450:791–+, September 1995.

[184] P. V. Ramanamurthy, C. E. Fichtel, D. A. Kniffen, P. Sreekumar, and D. J. Thompson. Possible Evidence for Pulsed Emission of High-Energy Gamma Rays by PSR B0656+14. *ApJ*, 458:755–+, February 1996.

[185] J. M. Rankin. Toward an empirical theory of pulsar emission. IV - Geometry of the core emission region. *ApJ*, 352:247–257, March 1990.

[186] N. Rea, et al. A Low-Magnetic-Field Soft Gamma Repeater. *Science*, 330:944–, November 2010.

[187] M. J. Rees and J. E. Gunn. The origin of the magnetic field and relativistic particles in the Crab Nebula. *MNRAS*, 167:1–12, April 1974.

[188] M. Rissi, N. Otte, T. Schweizer, and M. Shayduk. A New Sum Trigger to Provide a Lower Energy Threshold for the MAGIC Telescope. *IEEE Transactions on Nuclear Science*, 56:3840–3843, December 2009.

[189] R. W. Romani. Gamma-Ray Pulsars: Radiation Processes in the Outer Magnetosphere. *ApJ*, 470:469–+, October 1996.

[190] R. W. Romani, et al. Sub-luminous γ-ray Pulsars. *ApJ*, 738:114–+, September 2011.

[191] M. Ruderman. Crust-breaking by neutron superfluids and the VELA pulsar glitches. *ApJ*, 203:213–222, January 1976.

[192] M. Ruderman, T. Zhu, and K. Chen. Neutron Star Magnetic Field Evolution, Crust Movement, and Glitches. *ApJ*, 492:267–+, January 1998.

[193] M. A. Ruderman and P. G. Sutherland. Theory of pulsars - Polar caps, sparks, and coherent microwave radiation. *ApJ*, 196:51–72, February 1975.

[194] R. Ruderman. Neutron star crustal plate tectonics. II - Evolution of radio pulsar magnetic fields. III - Cracking, glitches, and gamma-ray bursts. *ApJ*, 382:576–593, December 1991.

[195] T. Sako, et al. Very High Energy Gamma-Ray Observations of PSR B1509-58 with the CANGAROO 3.8 Meter Telescope. *ApJ*, 537:422–428, July 2000.

[196] P. M. Saz Parkinson, et al. Eight γ-ray Pulsars Discovered in Blind Frequency Searches of Fermi LAT Data. *ApJ*, 725:571–584, December 2010.

[197] J. D. Scargle. Activity in the Crab Nebula. *ApJ*, 156:401–+, May 1969.

[198] F. D. Seward and F. R. Harnden, Jr. A new, fast X-ray pulsar in the supernova remnant MSH 15-52. *ApJL*, 256:L45–L47, May 1982.

[199] A. E. Shabad and V. V. Usov. Gamma-ray emission from strongly magnetized pulsars. *ArXiv e-prints*, September 2011.

[200] P. Slane. High Energy Studies of Pulsar Wind Nebulae. In F. A. Aharonian, W. Hofmann, & F. Rieger, editor, *American Institute of Physics Conference Series*, volume 1085 of *American Institute of Physics Conference Series*, pages 120–128, December 2008.

[201] P. O. Slane. Multiwavelength Studies of Pulsar Wind Nebulae. In *AAS/High Energy Astrophysics Division #11*, volume 42 of *Bulletin of the American Astronomical Society*, pages 695–+, February 2010.

[202] A. Spitkovsky and J. Arons. Time Dependence in Relativistic Collisionless Shocks: Theory of the Variable "Wisps" in the Crab Nebula. *ApJ*, 603:669–681, March 2004.

[203] D. H. Staelin and E. C. Reifenstein, III. Pulsating Radio Sources near the Crab Nebula. *Science*, 162:1481–1483, December 1968.

[204] I. H. Stairs. Pulsars in Binary Systems: Probing Binary Stellar Evolution and General Relativity. *Science*, 304:547–552, April 2004.

[205] P. A. Sturrock. Pulsar Radiation Mechanisms. *Nature*, 227:465–470, August 1970.

[206] B. N. Swanenburg, et al. Second COS B catalog of high-energy gamma-ray sources. *ApJL*, 243:L69–L73, January 1981.

[207] K. Tamura, N. Kawai, A. Yoshida, and W. Brinkmann. Evidence for a Pulsar Jet Producing a Hot Nebula in the Supernova Remnant MSH 15-52. *PASJ*, 48:L33–L36, June 1996.

[208] M. Tavani, et al. The AGILE Mission. *A&A*, 502:995–1013, August 2009.

[209] M. Tavani, et al. Discovery of Powerful Gamma-Ray Flares from the Crab Nebula. *Science*, 331:736–, February 2011.

[210] M. Tavani, et al. AGILE detection of enhanced gamma-ray emission from the Crab Nebula region. *The Astronomer's Telegram*, 2855:1–+, September 2010.

[211] J. H. Taylor, R. N. Manchester, and A. G. Lyne. Catalog of 558 pulsars. *ApJS*, 88:529–568, October 1993.

[212] J. H. Taylor and J. M. Weisberg. Further experimental tests of relativistic gravity using the binary pulsar PSR 1913 + 16. *ApJ*, 345:434–450, October 1989.

[213] The Fermi-LAT Collaboration. Fermi Large Area Telescope First Source Catalog. *2010arXiv1002.2280A*, February 2010.

[214] C. Thompson and R. C. Duncan. The soft gamma repeaters as very strongly magnetized neutron stars - I. Radiative mechanism for outbursts. *MNRAS*, 275:255–300, July 1995.

[215] C. Thompson and R. C. Duncan. The Soft Gamma Repeaters as Very Strongly Magnetized Neutron Stars. II. Quiescent Neutrino, X-Ray, and Alfven Wave Emission. *ApJ*, 473:322–342, December 1996.

[216] D. J. Thompson. Gamma ray pulsars. In K. S. Cheng and G. E. Romero, editors, *Cosmic Gamma-Ray Sources*, volume 304 of *Astrophysics and Space Science Library*, page 149, October 2004.

[217] D. J. Thompson, et al. Gamma Radiation from PSR B1055-52. *ApJ*, 516:297–306, May 1999.

[218] W. F. Tompkins, et al. EGRET Gamma-Ray Observations of the Crab P1/P2 Ratio. *ApJ*, 487:385–+, September 1997.

[219] A. Treves, M. Pilia, and M. L. Moya. On Energy-, Angular Momentum-Loss and Pulsar Spark Gaps. In *American Institute of Physics Conference Series*, volume 1357 of *American Institute of Physics Conference Series*, pages 312–313, August 2011.

[220] E. Trussoni, S. Massaglia, S. Caucino, W. Brinkmann, and B. Aschenbach. ROSAT PSPC observations of the supernova remnant MSH 15-52. *A&A*, 306:581–+, February 1996.

[221] M. P. Ulmer, et al. Gamma-Ray and Radio Observations of PSR B1509-58. *ApJ*, 417:738–+, November 1993.

[222] V. V. Usov and D. B. Melrose. Pulsars with Strong Magnetic Fields - Polar Gaps Bound Pair Creation and Nonthermal Luminosities. *Australian Journal of Physics*, 48:571–+, 1995.

[223] VERITAS Collaboration, E. Aliu, et al. Detection of Pulsed Gamma Rays Above 100 GeV from the Crab Pulsar. *ArXiv e-prints*, August 2011.

[224] V. Vittorini, et al. Spectral Evolution of the 2010 September Gamma-ray Flare from the Crab Nebula. *ApJL*, 732:L22+, May 2011.

[225] P. T. Wallace, et al. Detection of optical pulses from the VELA pulsar. *Nature*, 266:692–694, April 1977.

[226] N. Wang. Pulsar glitches detected at Urumqi. *Highlights of Astronomy*, 15:228–228, November 2010.

[227] K. P. Watters, R. W. Romani, P. Weltevrede, and S. Johnston. An Atlas for Interpreting γ-Ray Pulsar Light Curves. *ApJ*, 695:1289–1301, April 2009.

[228] K. W. Weiler and N. Panagia. VELA X and the evolution of Plerions. *A&A*, 90:269–282, October 1980.

[229] P. Weltevrede, et al. Gamma-ray and Radio Properties of Six Pulsars Detected by the Fermi Large Area Telescope. *ApJ*, 708:1426–1441, January 2010.

[230] P. Weltevrede and S. Johnston. Profile and polarization characteristics of energetic pulsars. *MNRAS*, 391:1210–1226, December 2008.

[231] P. Weltevrede, et al. Pulsar Timing with the Parkes Radio Telescope for the Fermi Mission. *Publications of the Astronomical Society of Australia*, 27:64–75, March 2010.

[232] R. D. Wills, et al. High-energy gamma-ray sources observed by COS-B. In R. Cowsik & R. D. Wills, editor, *Non-Solar Gamma-Rays*, pages 43–47, 1980.

[233] R. B. Wilson, et al. BATSE/CGRO Observations of Isolated Pulsars. In K. A. van Riper, R. I. Epstein, & C. Ho, editor, *Isolated Pulsars*, page 257, 1993.

[234] C. A. Wilson-Hodge, et al. When a Standard Candle Flickers. *ApJL*, 727:L40+, February 2011.

[235] L. Zhang and K. S. Cheng. The optical, X-ray and gamma-ray light curves and spectra of crab-like pulsars: PSR B0540-69 and PSR B1509-58. *A&A*, 363:575–584, November 2000.

Acknowledgments

I would firstly like to thank my Supervisors Prof. Aldo Treves and Dr. Alberto Pellizzoni for their precious scientific insights and prolific discussion that helped me develop a deeper critical knowledge on pulsars' physics.

I am particularly grateful to Andrea Possenti and Marta Burgay for their continuous help in my pulsar education and studies, and to Paolo Esposito and Alessio Trois for the huge technical and theoretical support during my PhD.

This Thesis acknowledges financial contribution from the agreement ASI-INAF I/009/10/0

Last but not least I wish to thank all the people who have passed by in these three years at the astrophysicists' office, for making this experience a most pleasant one and for rendering the work days much more fun.